

Master Thesis

Evaluation of 50-cm photomultiplier tube stability  
and proton decay search sensitivity for the  
Hyper-Kamiokande experiment  
( ハイパーカミオカンデ実験に向けた50 cm 口径  
光電子増倍管の安定性評価および陽子崩壊探索  
の感度評価 )

January 24, 2025

Department of Physics, Graduate School of Science  
The University of Tokyo  
東京大学大学院理学系研究科物理学専攻

Sanshiro Goto  
後藤三四郎

# Abstract

Hyper-Kamiokande (HK), which is the successor to Super-Kamiokande (SK), is a gigantic water Cherenkov detector that will use 20,000 newly developed 50 cm-diameter photomultiplier tubes (HKPMT). One of the main physics targets of HK is nucleon decay. In preparation for the search for nucleon decay in HK, this thesis first evaluates the stability of the PMTs, which are key to the performance of HK. Then, the sensitivity of HK to the decay mode of  $p \rightarrow e^+\pi^0$  is also evaluated through simulations as the first attempt using software developed for HK.

As for the stability evaluation of HKPMT, two types of measurement were conducted; measurement of dark rate for large number of PMTs (mass-measurement) and measurement of dark rate and gain for more than one year (long-term measurement).

In mass-measurement, up to 200 of the PMTs delivered each month are measured for 1 to 6 months to assess the stability of dark rate of PMTs and production quality with large statistics. More than 2,000 PMTs have been measured since July 2023 in mass-measurement and the cumulative result satisfies HK's requirement. However, several factors that could potentially cause issues in a long term operation are identified and further investigation is needed. In addition, more consideration is required when considering a 10- or 20-year operation of HK.

In long-term measurement, dark rate and gain of 16 PMTs have been monitored since July 2023 and October 2023, respectively. Dark rates have remained stable over a year. For gain, an increasing trend of  $1.3 \pm 0.4$  %/year has been observed and this is a similar trend with SKPMT.

As for the evaluation of the sensitivity to  $p \rightarrow e^+\pi^0$  in HK, from the signal and background (atmospheric neutrino) Monte Carlo simulations (MC), the signal efficiency and the background rate in HK are estimated to be  $36.76 \pm 0.24$  % and  $1.62 \pm 0.40$  events/(Mt·year), respectively, while the signal efficiency and the background rate were about 42 % and 1.83 events/(Mt·year), respectively, in the previous analysis in SK. Assuming the performances estimated in this study, the search sensitivity in HK with only the statistical uncertainty exceeds the current life time limit after 3 years operation and reaches  $10^{35}$  years after about 25 years operation. These estimated sensitivities are worse than the official sensitivity of HK estimated with software for SK, but they can be improved if tuning of software for HK is completed and additional analysis techniques such as neutron tagging are applied.

# Contents

<b>1</b>	<b>Physics Background</b>	<b>4</b>
1.1	Standard model and its limitation . . . . .	4
1.2	Grand Unified Theories . . . . .	5
1.2.1	$SU(5)$ model . . . . .	5
1.2.2	SUSY $SU(5)$ model . . . . .	6
1.2.3	$SO(10)$ model . . . . .	7
1.3	Search for nucleon decay . . . . .	7
1.4	Overview of this thesis . . . . .	8
<b>2</b>	<b>Hyper-Kamiokande Experiment</b>	<b>9</b>
2.1	Particle detection . . . . .	9
2.1.1	Cherenkov radiation . . . . .	9
2.1.2	Observation of Cherenkov light . . . . .	10
2.2	Water tank . . . . .	11
2.3	50 cm PMT for Hyper-Kamiokande . . . . .	13
<b>3</b>	<b>Stability evaluation of HKPMT</b>	<b>18</b>
3.1	Necessity of stability evaluation . . . . .	18
3.1.1	Problem about dark rate stability of HKPMT . . . . .	18
3.1.2	Screening test before delivery . . . . .	18
3.1.3	Necessity of stability evaluation . . . . .	18
3.2	Stability evaluation . . . . .	19
3.2.1	Dark rate . . . . .	19
3.2.2	Gain . . . . .	19
3.3	Mass-measurement of PMT . . . . .	20
3.3.1	Experimental setup . . . . .	20
3.3.2	Data analysis . . . . .	23
3.3.3	Result of mass measurement . . . . .	24
3.3.4	Summary of mass-measurement . . . . .	29
3.4	long-term measurement of PMT . . . . .	29
3.4.1	Experimental setup . . . . .	30
3.4.2	Dark rate measurement . . . . .	32
3.4.3	Gain measurement . . . . .	35
3.4.4	Summary of long-term measurement . . . . .	40
3.5	Summary and discussion of stability evaluation of PMT . . . . .	41

<b>4</b>	<b>Evaluation of proton decay search sensitivity for Hyper-Kamiokande</b>	<b>42</b>
4.1	Monte Carlo Simulation . . . . .	42
4.1.1	Event generation . . . . .	42
4.1.2	Propagation of particles in water . . . . .	46
4.1.3	Detector response . . . . .	46
4.2	Event Reconstruction with fitQun . . . . .	47
4.2.1	Likelihood . . . . .	48
4.2.2	Predicted charge . . . . .	48
4.2.3	Vertex pre-fitter . . . . .	49
4.2.4	Single-ring fitter . . . . .	50
4.2.5	Multi-ring fitter . . . . .	51
4.2.6	Dependence of fitQun performance on distance from wall . . . . .	52
4.3	Proton decay analysis . . . . .	55
4.3.1	Event selection . . . . .	55
4.3.2	Sensitivity . . . . .	65
4.4	Summary . . . . .	67
<b>5</b>	<b>Summary</b>	<b>69</b>

# Chapter 1

## Physics Background

Through the various experiments in the 20th and 21st centuries, particle physics has developed dramatically. The discovery of the Higgs boson by the ATLAS [1] and the CMS [2] experiments in 2012 has verified the correctness of the beautiful theory known as the standard model (SM), which can explain most of the results from previous particle physics experiments. However, a more fundamental theory beyond the SM is believed to exist. In fact, for example, the Super-Kamiokande (SK), which has been operated since 1996, observed neutrino oscillation in 1998 and this phenomenon cannot be explained by the SM.

Nucleon decay is one of effective phenomena for testing theories beyond the SM. Many experiments including SK have searched for nucleon decay, but none of them has observed it so far.

### 1.1 Standard model and its limitation

In the SM, there are 17 elementary particles as shown in Fig. 1.1. Gauge bosons mediate fundamental interactions; electromagnetic, weak, and strong interactions (gravitational interaction is not considered in the SM). Quarks are the fermions which interact via all interactions and compose of hadrons such as proton. Leptons are also fermions but they do not interact via the strong interaction. In particular, neutrinos interact via only the weak interaction. Higgs boson gives mass to particles. One of the most important points in the SM is that all fundamental interactions except for the gravitational interaction are generated from gauge symmetry. The strong interaction is described by the  $SU(3)_C$  symmetry. The electromagnetic and weak interactions are collectively described by the  $SU(2)_L \times U(1)_Y$  symmetry. In short, the SM is the quantum field theory with  $SU(3)_C \times SU(2)_L \times U(1)_Y$ .

While the SM is consistent with the results of most past particle physics experiments, it cannot explain some things such as the gravitational interaction, dark matter, neutrino masses, etc. Moreover, many parameters in the SM can only be determined experimentally. For example, it cannot be derived from the SM that the number of generations of quarks and leptons is three.

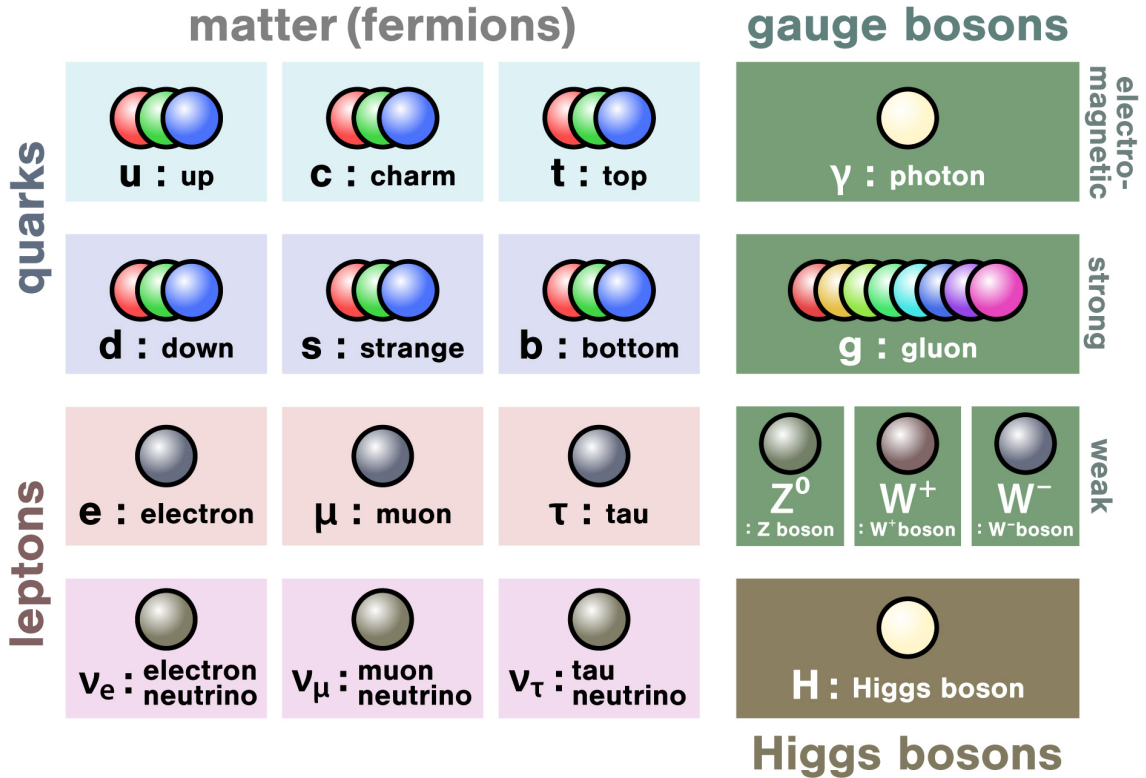


Figure 1.1. Elementary particles in the SM. Taken from [3]

## 1.2 Grand Unified Theories

Theories which describe the strong, electromagnetic, and weak interactions with single gauge symmetry are called Grand Unified Theories (GUTs) and many problems in the SM are expected to be solved by GUTs. Since the first GUT was proposed by H. Georgi and S. Glashow in 1974 [4], many GUT models have been proposed. GUT models generically predict proton decay. In this section, we focus on  $SU(5)$ , SUSY  $SU(5)$ , and  $SO(10)$  models.

### 1.2.1 $SU(5)$ model

$SU(5)$  is the minimum gauge group which contains  $SU(3)_C \times SU(2)_L \times U(1)_Y$ . In  $SU(5)$  model, fermions are represented by  $\mathbf{10} + \bar{\mathbf{5}}$  and gauge bosons are represented by  $\mathbf{24}$  as

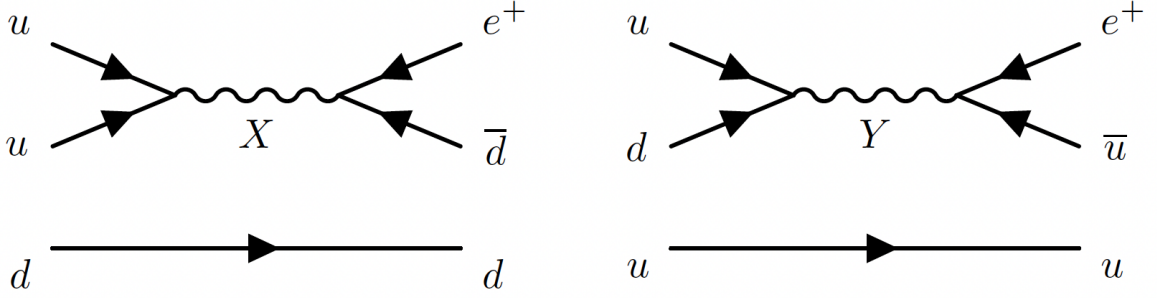


Figure 1.2. Feynman diagrams for  $p \rightarrow e^+\pi^0$  via  $X$  and  $Y$  bosons

follows;

$$\bar{\mathbf{5}} : \begin{pmatrix} d_1^c \\ d_2^c \\ d_3^c \\ e \\ -\nu_e \end{pmatrix} \text{ and } \mathbf{10} : \begin{pmatrix} 0 & u_3^c & -u_2^c & u_1 & d_1 \\ -u_3^c & 0 & u_1^c & u_2 & d_2 \\ u_2^c & -u_1^c & 0 & u_3 & d_3 \\ -u_1 & -u_2 & -u_3 & 0 & e^c \\ -d_1 & d_2 & -d_3 & -e^c & 0 \end{pmatrix}, \quad (1.1)$$

$$\mathbf{24} : \begin{pmatrix} G_1^1 - \frac{2B}{\sqrt{30}} & G_2^1 & G_3^1 & \bar{X}_1 & \bar{Y}_1 \\ G_1^2 & G_2^2 - \frac{2B}{\sqrt{30}} & G_3^2 & \bar{X}_2 & \bar{Y}_2 \\ G_1^3 & G_2^3 & G_3^3 - \frac{2B}{\sqrt{30}} & \bar{X}_3 & \bar{Y}_3 \\ X^1 & X^2 & X^3 & \frac{W^3}{\sqrt{2}} + \frac{3B}{\sqrt{30}} & W^+ \\ Y^1 & Y^2 & Y^3 & W^- & -\frac{W^3}{\sqrt{2}} + \frac{3B}{\sqrt{30}} \end{pmatrix}, \quad (1.2)$$

where the  $G_j^i$ s correspond to the gluons of  $SU(3)_C$ ,  $W^\pm$ ,  $W^3$ s,  $B$  correspond to the gauge bosons of  $SU(3)_L \times U(1)_Y$ , and  $X$  and  $Y$  are 12 new gauge bosons which exchange quarks and leptons.

In the minimal  $SU(5)$  model,  $p \rightarrow e^+\pi^0$  is the dominant decay mode whose predicted proton lifetime is about  $10^{31\pm 1}$  years [5]. Figure 1.2 shows the Feynman diagrams for  $p \rightarrow e^+\pi^0$ . However, this model was already excluded by the previous experiments as shown in Sec.1.3.

## 1.2.2 SUSY $SU(5)$ model

$SU(5)$  model is saved by introducing a symmetry between fermions and bosons, so-called ‘‘super-symmetry(SUSY)’’. SUSY makes the number of both fermions and bosons double.

In the minimal SUSY  $SU(5)$  model, the most dominant decay mode is  $p \rightarrow \bar{\nu}K^+$  whose predicted upper limit of the partial lifetime is  $< 2.9 \times 10^{30}$  years [6]. This minimal SUSY  $SU(5)$  model was also already excluded by as shown in Sec.1.3.

### 1.2.3 $SO(10)$ model

The next larger GUT is  $SO(10)$  model. This model includes right-handed neutrinos and explain the generation of the finite neutrino mass, which is not assumed in the SM. In this model, all fermions are represented by **16**.  $SO(10)$  has many patterns of symmetry breaking as below;

$$SO(10) \rightarrow \begin{cases} SU(5) \times U(1), \\ SU(4) \times SU(2)_L \times SU(2)_R, \\ SU(3) \times SU(2)_L \times SU(2)_R \times U(1), \\ SU(4) \times SU(2)_L \times U(1) \end{cases} \rightarrow SU(3)_C \times SU(2)_L \times U(1)_Y \quad (1.3)$$

The most dominant decay mode of  $SO(10)$  model is  $p \rightarrow e^+\pi^0$  as well as the minimal  $SU(5)$  model and its predicted lifetime is  $10^{34}$ - $10^{39}$  years [7][8].

## 1.3 Search for nucleon decay

Various experiments, such as IMB [9], Kamiokande [10], and SK [11], have searched for nucleon decay, but no significant signal exceeding background has been observed so far. In particular, SK has determined the lower limits of the lifetime for many decay modes. For example, the lower limits on the lifetimes for  $p \rightarrow e^+\pi^0$  and  $p \rightarrow \bar{\nu}K^+$  have both been obtained by SK, with values of  $2.4 \times 10^{34}$  years [12] and  $5.9 \times 10^{33}$  years [13], respectively. These results ruled out the minimal  $SU(5)$  and minimal SUSY  $SU(5)$  models. However, there are many GUT models which predict longer lifetime of nucleons and it is difficult to validate such models in SK. Figure 1.3 shows a comparison of historical experimental limits on the nucleon lifetime for several key modes and ranges of theoretical prediction as of 2018. Expected limits obtained by some future experiments are also included in the same figure.

An idea to search to longer lifetimes than the current lower limits is to use larger detectors. Roughly speaking, if the number of nucleons in the detector is 10 times greater, the lifetime that can be searched for in the same observation time will also be 10 times longer. The successor to SK explained in Chapter 2, Hyper-Kamiokande, will have an about eight times larger fiducial volume than that of SK and nucleon decay search is one of the main physics targets of Hyper-Kamiokande. Considering the comparison of fiducial volume between Hyper-Kamiokande and SK, Hyper-Kamiokande can explore a lifetime of up to about  $10^{35}$  years for  $p \rightarrow e^+\pi^0$ . This value covers the entire range of predicted lifetimes of models such as SUSY  $SO(10)$  as shown in Fig. 1.3.

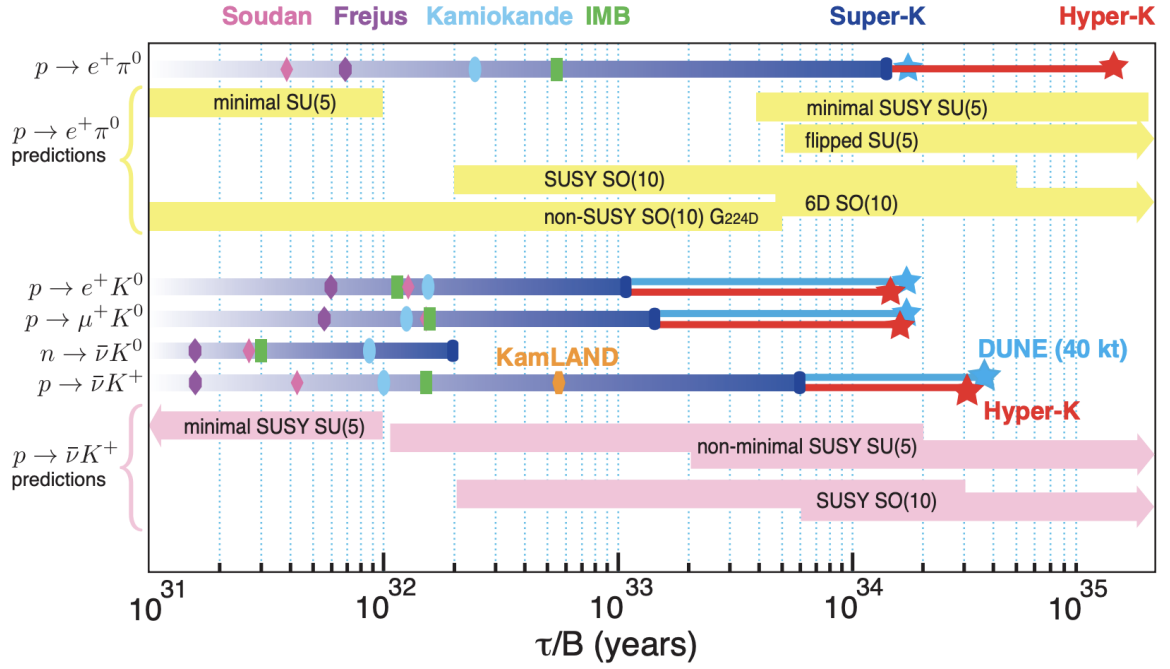


Figure 1.3. A comparison of historical experimental limits on the nucleon lifetime for several key modes and ranges of theoretical prediction as of 2018. Expected limits by some future measurements are also included. Taken from [14].

## 1.4 Overview of this thesis

In Chapter 2, the overview of Hyper-Kamiokande is explained. Then in Chapter 3, the stability of the photomultiplier tubes, which are key to the performance of Hyper-Kamiokande, is evaluated in preparation for the search for proton decay in Hyper-Kamiokande. Finally in Chapter 4, the sensitivity of Hyper-Kamiokande to proton decay is also evaluated through simulations. This sensitivity study is the first attempt using software developed for Hyper-Kamiokande.

# Chapter 2

## Hyper-Kamiokande Experiment

Hyper-Kamiokande (HK) is the successor to SK. HK is a gigantic water Cherenkov detector that uses 260 kt of ultrapure water and about 20,000 50 cm diameter photomultiplier tubes (PMTs) to detect Cherenkov light. The construction of HK began in 2020 in Kamioka-cho, Hida City, Gifu Prefecture and the operation will be started in 2027. This chapter provides an overview of HK.

### 2.1 Particle detection

#### 2.1.1 Cherenkov radiation

HK observes physics events such as neutrino interactions and nucleon decays by detecting the Cherenkov light emitted by charged particles produced by the events.

Cherenkov radiation is electromagnetic radiation emitted when a charged particle moves through a medium at a speed greater than the phase velocity of light in that medium. Figure 2.1 shows a schematic view of Cherenkov radiation. The Cherenkov light is emitted in a conical shape. The opening angle of the cone  $\theta$  is determined by the velocity of the charged particle as below;

$$\cos \theta = \frac{1}{\beta n}, \quad (2.1)$$

where the  $\beta$  is the ratio of the velocity  $v$  to speed of light in vacuum  $c$  ( $\beta = v/c$ ) and  $n$  is the refractive index of the medium. The momentum threshold for Cherenkov radiation is derived from the condition of  $\beta > 1/n$ . Table 2.1 summarizes the Cherenkov threshold for various charged particles in water.

Table 2.1. Momentum thresholds of the Cherenkov radiation in water for various charged particles in water ( $n = 1.34$ )

	$e$	$\mu$	$\pi^+$	$p$
Momentum (MeV/ $c$ )	0.57	118	156	1052

The number of Cherenkov photons emitted by a particle of charge  $Ze$  at wavelengths

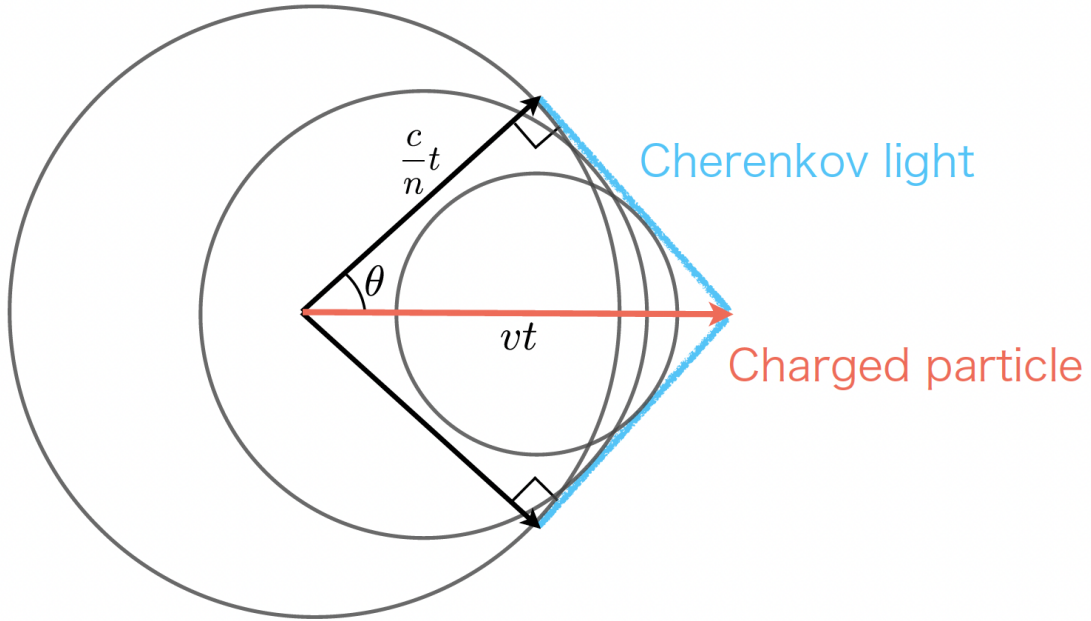


Figure 2.1. A schematic view of Cherenkov radiation. Taken from [15].

$\lambda$  to  $\lambda + d\lambda$  per unit length  $dN(\lambda)$  is expressed as below;

$$dN(\lambda) = \frac{2\pi Z^2}{137} \left\{ 1 - \left( \frac{1}{\beta n(\lambda)} \right)^2 \right\} \frac{d\lambda}{\lambda^2}. \quad (2.2)$$

The shorter the wavelength, the more photons are emitted. The 50 cm PMT installed in the inner tank is sensitive to wavelengths of 300 to 600 nm, and in this region, a charged particle with  $\beta \sim 1$  emits about 350 photons/cm.

### 2.1.2 Observation of Cherenkov light

Cherenkov light is detected by PMTs placed on the surface of the detector as shown in Fig. 2.2. Since Cherenkov light is emitted in a conical shape, the PMTs detecting Cherenkov light are distributed in a ring shape.

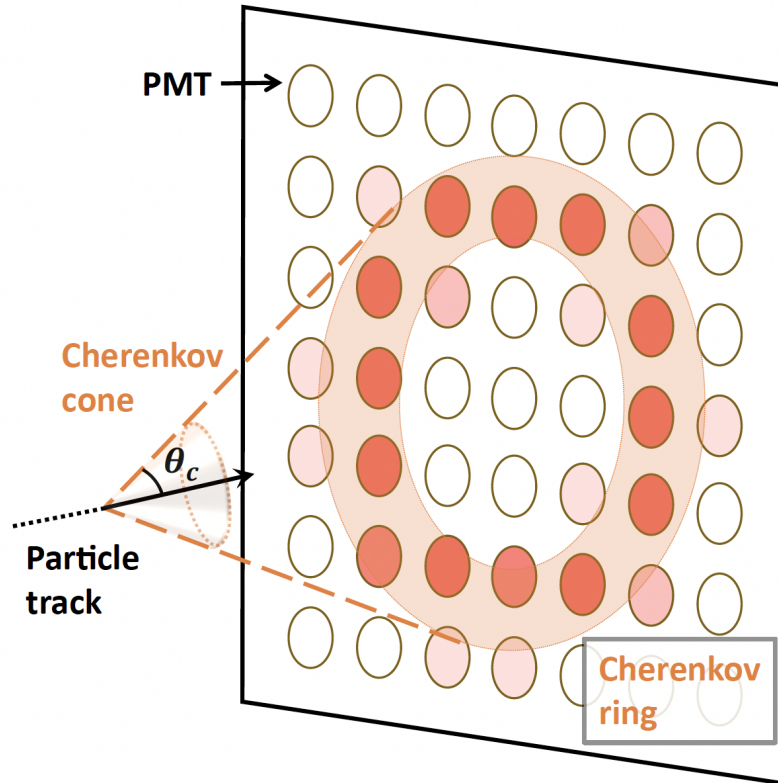


Figure 2.2. Cherenkov radiation and PMTs which detect those light. Taken from [16].

As explained in Sec.2.1.1, the number of photons emitted and the opening angle of the cone is determined by the velocity of the particle. Therefore, the momentum and the direction of the particle can be reconstructed using the information such as the detected charge, the time of light detection, and the distribution of PMTs that detected the light. In addition, electrons and gamma rays make a fuzzier ring than muons or charged pions because electrons and gamma rays generate electromagnetic shower when propagating in the water. Such differences in the shape of the ring can be used for particle identification. The detail of the event reconstruction is explained in Sec.4.2.

## 2.2 Water tank

The water tank of HK is a stainless steel cylindrical tank with a diameter of 68 m, a height of 71 m, and it will contain about 260 kt water. This tank is constructed 600 meters underground in the Kamioka mine to reduce cosmic ray muons. Figure 2.3 shows a schematic view of HK. The tank has two layers as in SK; the inner detector (ID) and the outer detector (OD). The ID is the main detector, which detects Cherenkov light generated in neutrino events or nucleon decay. About 20,000 50 cm diameter PMTs will be installed on the inner side of the ID in a checkerboard pattern (see Fig. 2.4), with a photocathode coverage in the ID wall of 20 %. The OD surrounds the ID with a water thickness of 1 m at the sides and 2 m at the top and bottom. The OD is used to remove

cosmic rays as background for observations and to shield the ID from radiation from the bedrock surrounding HK. About 3,600 8 cm PMTs will be installed on the inner wall of the OD facing outward.

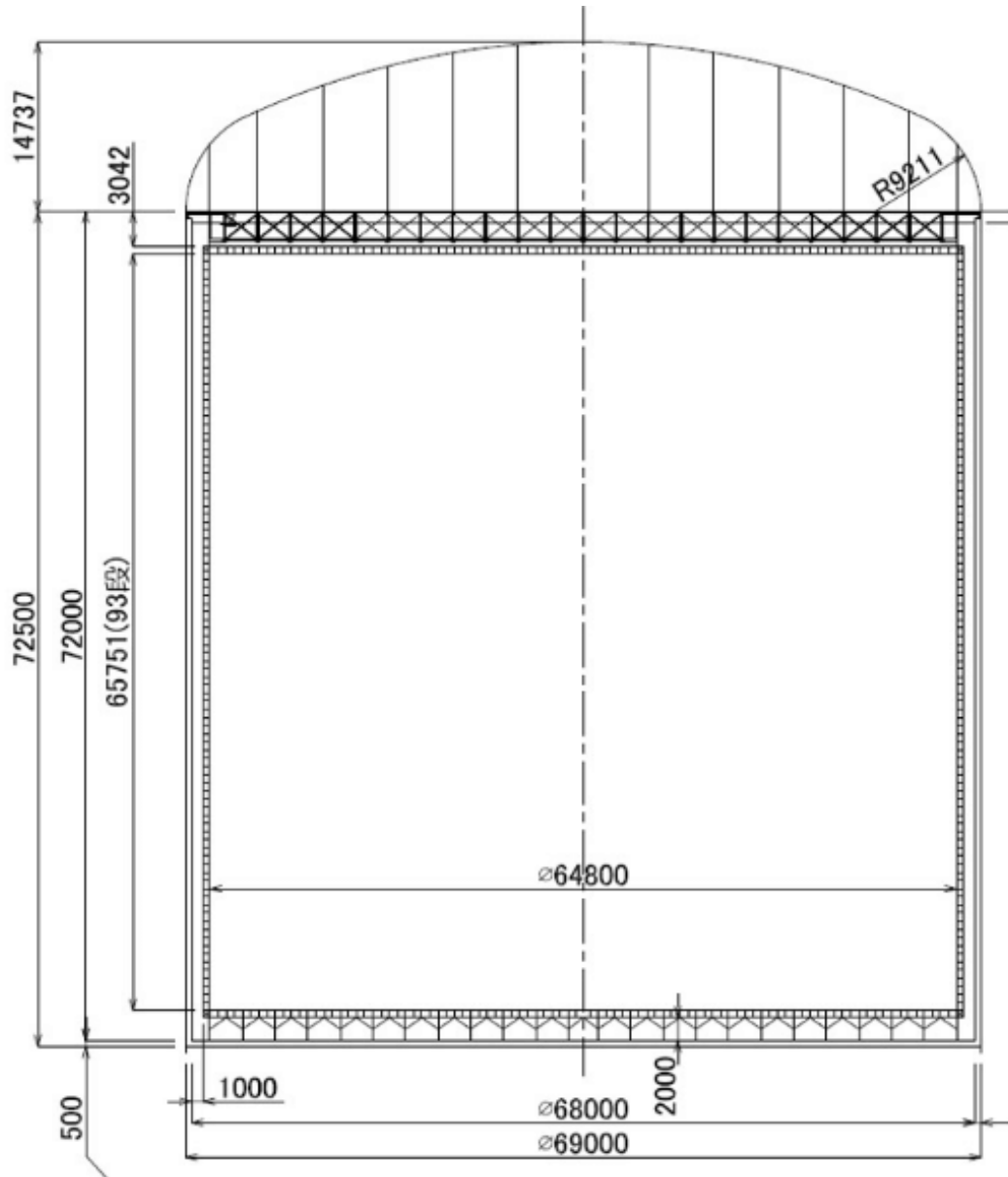


Figure 2.3. A schematic view of HK [17]

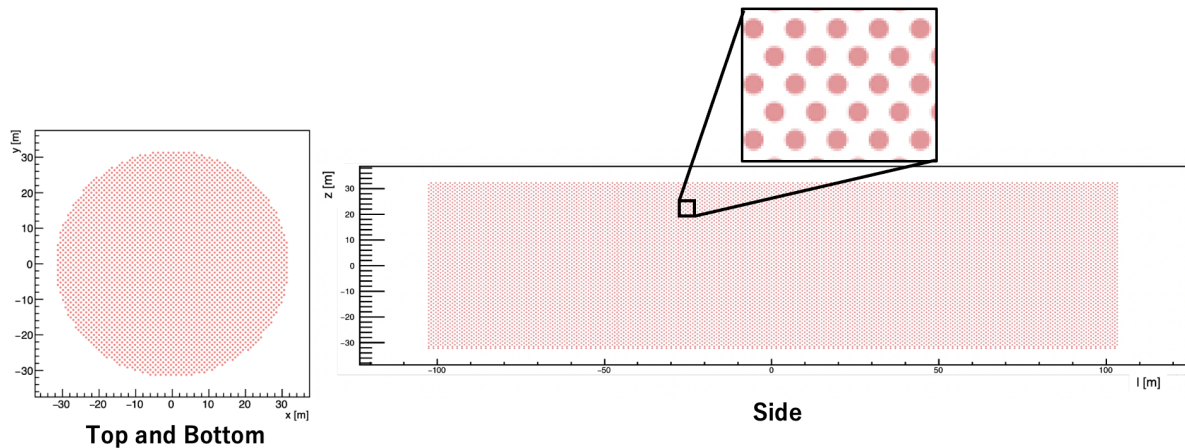


Figure 2.4. The arrangement of PMTs on the ID wall. The circle (left) represents the top (bottom) of a cylindrical tank. The rectangle (right) represents the side of the cylindrical tank. Pink dots in the figure represent PMTs. PMTs are placed in a checkerboard pattern. Taken from [16].

### 2.3 50 cm PMT for Hyper-Kamiokande

PMT is a photodetector that detects photons by converting them into electrons through the photoelectric effect. To detect the faint Cherenkov radiation, the PMTs need to have high photon detection efficiency. In addition, since the event reconstruction uses the time and number of photons detected by each PMT, time resolution and charge resolution are important. Other than performance related to photon detection, high pressure resistance and waterproof performance are also required to withstand operation at depths of several tens of meters.

In SK, 50 cm PMT (SKPMT, R3600 [18]) made by Hamamatsu Photonics (HPK) has been used. In HK, 50 cm PMT improved from SKPMT (HKPMT, R12860) will be used (Fig. 2.5).



Figure 2.5. HKPMT

One of the main changes from SKPMT is that the structure of the dynode has changed from a “Venetian blind” type to a “Box & Line” type (Fig. 2.6). Unlike the venetian blind type, the Box&Line type has a much higher time resolution because the electrons are amplified through almost a single pathway. Furthermore, the collection efficiency of photoelectrons has also improved due to the larger size of the first stage dynode.

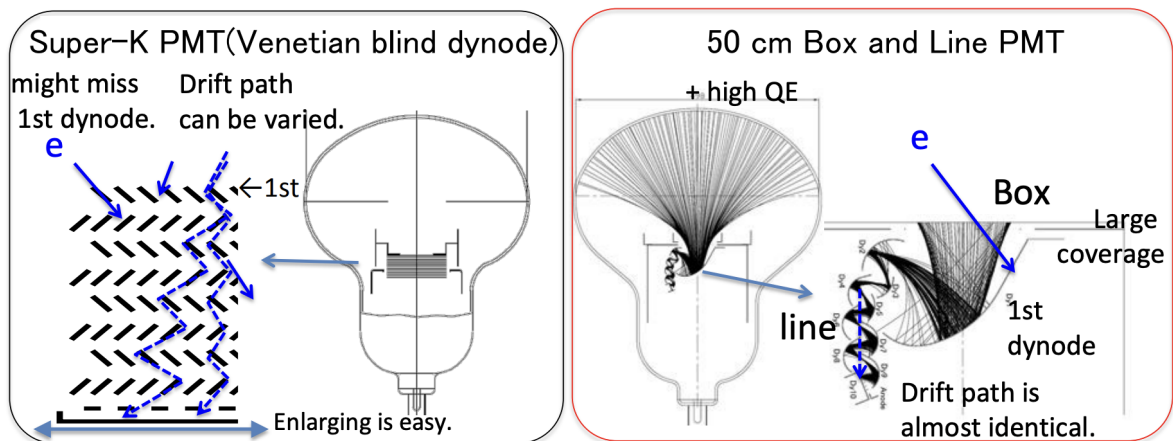


Figure 2.6. Venetian blind type dynode in SKPMT (left) and Box & Line type dynode in HKPMT (Right) [19]

Other than the structure of dynode, the photocathode has a higher QE. As a result of these improvement, the single photoelectron time and charge resolutions of HKPMT represent a factor of two improvement over SKPMT (see Fig. 2.7, Fig. 2.8). In addition,

the relative single photon detection efficiency is twice that of SKPMT (see Fig. 2.9). Table 2.2 is a summary table of basic performances of HKPMT and SKPMT.

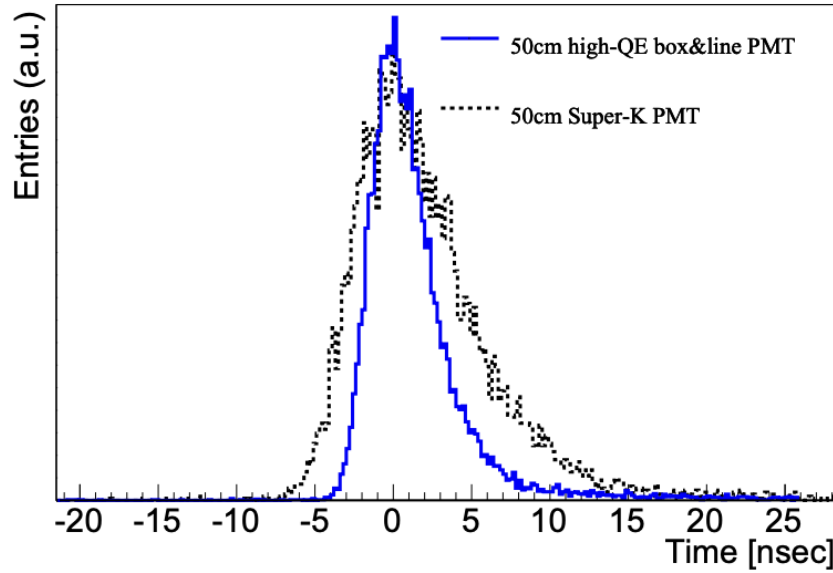


Figure 2.7. Transit time distribution at single photoelectron [14]. Blue solid line is HKPMT and black dotted line is SKPMT.

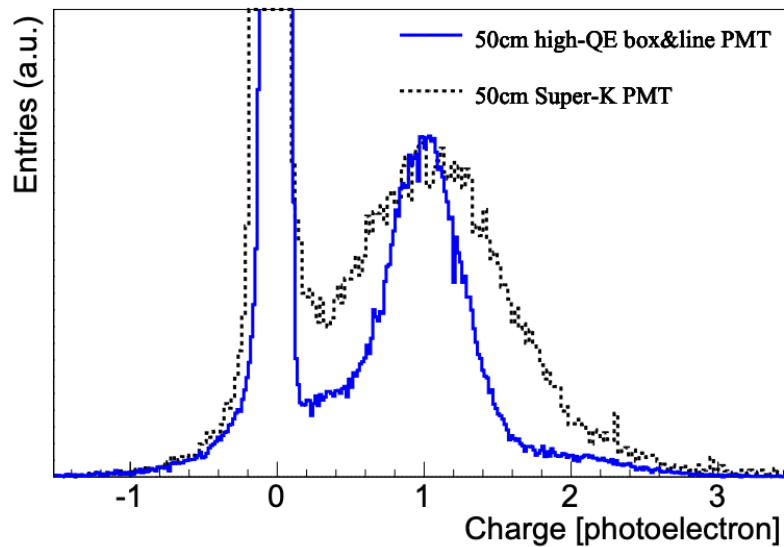


Figure 2.8. Single photoelectron distribution with pedestal [14]. Blue solid line is HKPMT and black dotted line is SKPMT.

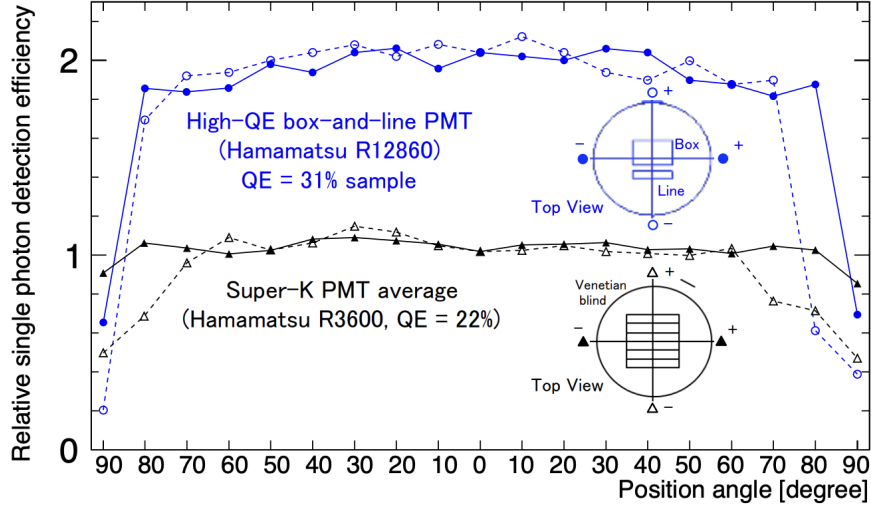


Figure 2.9. Relative single photon detection efficiency as a function of the position in the photocathode, where a position angle is zero at the PMT center and  $\pm 90^\circ$  at the edges [14]. The dashed line is the result of a scan along the line of symmetry of the Box&Line dynode structure, and the solid line is the result of a scan along the direction orthogonal to the line of symmetry.

Table 2.2. Summary of the basic performances of HKPMT and SKPMT

	HKPMT	SKPMT	Remarks
Quantum efficiency [%]	30	22	At $\lambda=390$ ns [20]
Collection efficiency [%]	95	73	From [20]
Timing resolution [ns]	2.59	6.73	FWHM of transit time spread [20]
Charge resolution [%]	30.8	60.1	$\sigma/mean$ of 1 p.e. peak [20]

Since the height of HK is about twice of that of SK, pressure resistance and waterproof performance of HKPMT are also improved from SKPMT. Figure 2.10 shows a side view of HKPMT. The shape of HKPMT is similar with that of SKPMT, but the curvature of the neck and photocathode is more relaxed.

The mass production of HKPMT began in 2020 and approximately 12,000 PMTs have been delivered to Kamioka by November 2024. The mass production will continue until 2026.

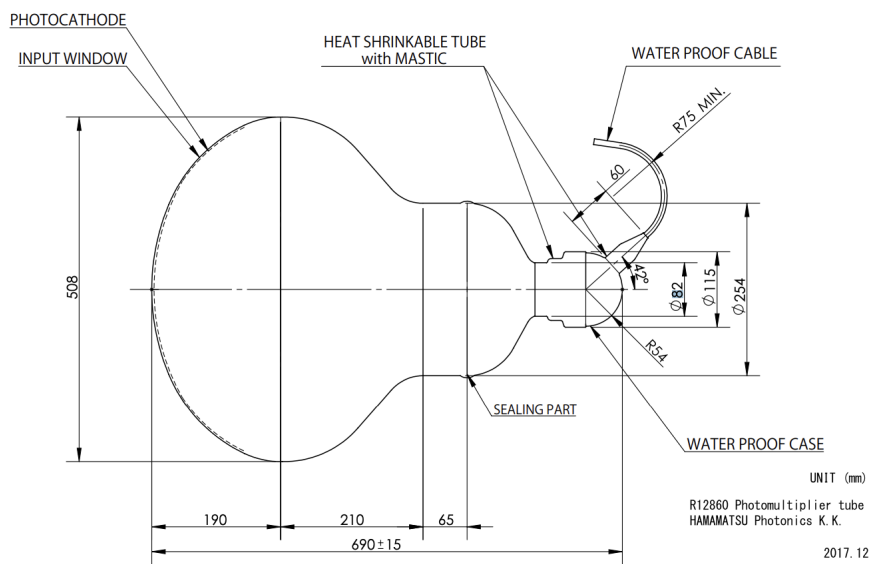


Figure 2.10. Side view of HKPMT [14]

# Chapter 3

## Stability evaluation of HKPMT

### 3.1 Necessity of stability evaluation

#### 3.1.1 Problem about dark rate stability of HKPMT

The mass production of PMTs began in 2020. Since 2021, a sample of the delivered PMTs had been tested for quality assurance, including basic performance measurements such as dark rate, time resolution, and charge resolution, over a period of about a week. It was found that about 10-20 % of the PMTs exhibited unstable dark rates and some of them became unstable several days after the start of the measurements. As a result, the delivery of PMTs was stopped in May 2022. Investigations were carried out to find the cause of the instability of the dark rate, and improvements were made. As a result of these efforts, the deliveries of PMTs resumed in May 2023.

In this thesis, PMTs produced before and after the improvements were made are called “original PMTs” and “improved PMTs”, respectively.

#### 3.1.2 Screening test before delivery

In addition to the improvements explained in Sec.3.1.1, a screening test to evaluate dark rate and its stability lasting one week has been imposed on produced PMTs before delivery by the manufacturer (HPK) in order to reduce unstable PMTs since the delivery was restarted. This test is imposed not only on improved PMTs but also on original PMTs because there are PMTs among the original PMTs that are not problematic and we want to use them. Only PMTs that pass this test have been delivered.

#### 3.1.3 Necessity of stability evaluation

As mentioned in Sec.3.1.1, there are PMTs that become unstable during operation. Although all delivered PMTs passed the one week screening test by HPK, it is possible that dark rate instability appears with longer term operation. Therefore, measurements to evaluate dark rate stability of PMTs are needed in addition to the screening test. Moreover, an increasing trend of gain has been observed in SKPMT, so whether a similar trend is present in HKPMT is also needed to be evaluated at this stage.

## 3.2 Stability evaluation

To evaluate the stability of PMT, the following two types of PMT measurements have been conducted after the resumption of PMT deliveries;

- Mass-measurement : measurement of dark rate of 200 PMTs per month
- long-term measurement : measurement of dark rate and gain of 16 PMTs over a year

This thesis describes these two types of measurements. The following two sections (Sec.3.2.1 and Sec.3.2.2) are explanations of measured quantities in both measurements.

### 3.2.1 Dark rate

Even when a PMT is set in the dark, signals occur because of thermal electron from its photocathode, scintillation light caused by the radio isotopes in the glass of PMT, environmental radiation, etc. Such signal is called “dark count”, and “dark rate” is defined as the number of the dark counts per one second. In this thesis, the dark rate is evaluated as the average value over one minute. For HKPMT, typical dark rate is about 4 kHz with a threshold voltage of  $-1$  mV, but actual measured value at the location where measurement setups described in this thesis exist is about 7 or 8 kHz due to high concentrations of environmental radiation in those places.

In HK, if the dark rate exceeds 10 kHz, it can interfere event triggering and transferring data. Therefore, PMTs which have a high rate over 10 kHz are unacceptable. In addition, if there are problems such as insulation failures in the PMT, dark rate fluctuations or sharp increases, etc. can be observed. Moreover, if a PMT flashes due to discharge inside the PMT (“flasher PMT”), dark rates of surrounding PMTs can also be unstable. The value of dark rate is used for correction of number of hit PMTs to estimate the true number of PMTs which detect Cherenkov light, so the stability of dark rate is also important for the detector performance.

### 3.2.2 Gain

The electrons emitted from the photocathode of the PMT are amplified at the dynodes and then output as a signal. The gain of HKPMT is set to about  $1 \times 10^7$ .

In SK, a trend of about 2 percent increase per year in gain has been observed [15] (Fig. 3.1). It is speculated that the cause of this change is that the amount of cesium in the dynode changes during operation. In detail, as the cesium in the dynode decreases with operation, the gain increases until a certain level, and after it decreases beyond the level, the gain starts to decrease in the opposite direction. There are individual differences in gain variation and there are PMTs which have a decreasing tendency of gain.

HKPMT also uses cesium, so the same phenomenon that occurs with SKPMT can also happen. However, whether a similar trend exists in mass produced HKPMT has not yet been tested. Therefore, we have measured long-term trends in the gain of HKPMT.

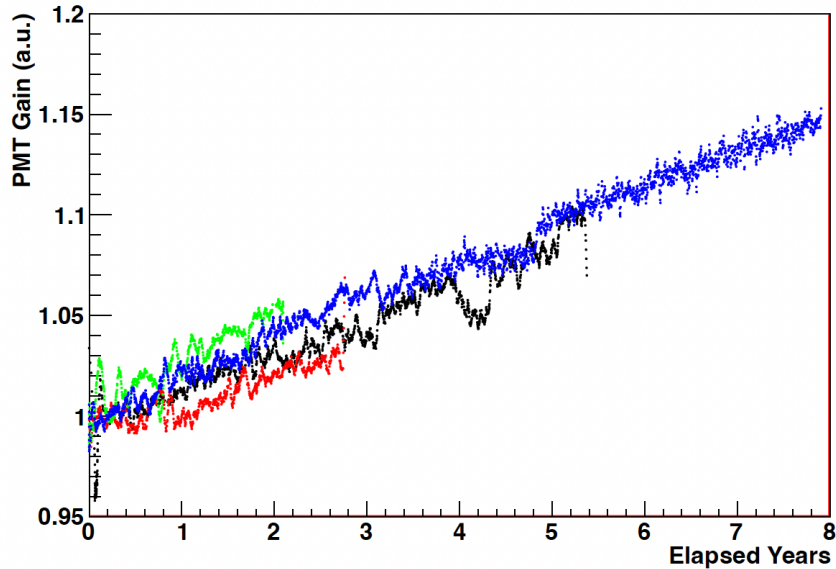


Figure 3.1. Time variation of the averaged PMT gain measured by using the PMTs in the bottom of the SK tank [15]. The colors show the detector periods; black, red, green and blue are for SK-I, -II, -III and -IV, respectively.

### 3.3 Mass-measurement of PMT

About 500 PMTs are delivered to Kamioka every month. In mass-measurement, 100 to 200 of those delivered PMTs are sampled and measured for 1 to 6 months immediately. This allows for the early detection of any changes in quality during mass production. In this measurement, dark rate and its stability are monitored for large numbers of PMTs. More than 20 % of all PMTs will be tested by the end of PMT delivery. Therefore, dark rate stability of PMTs and change in quality can be evaluated through large statistics.

#### 3.3.1 Experimental setup

There are two dark rooms in Kamioka and each of them can accommodate 100 PMTs (Fig. 3.2). One room (room B) is used for measurement for one month (1-month measurement), and the other room (room A) is basically used for longer-term measurement such as 3 months or 6 months (3- or 6-month measurement). PMTs are delivered to Kamioka every month, and at that timing, one period of 1-month measurements is finished and the PMTs are replaced with delivered ones. After the replacement, next measurement is started. For 3- or 6-month measurements, the measured PMTs are replaced at the timing of delivery as well as 1-month measurements, but the frequency is once every 3 or 6 deliveries. One PMT in each room is used as a reference and is not exchanged. The reference PMT is not counted as evaluated PMT. In addition, there are instances where some PMTs cannot be measured due to malfunctions in the measurement equipment such as a sudden power-off of the high voltage.

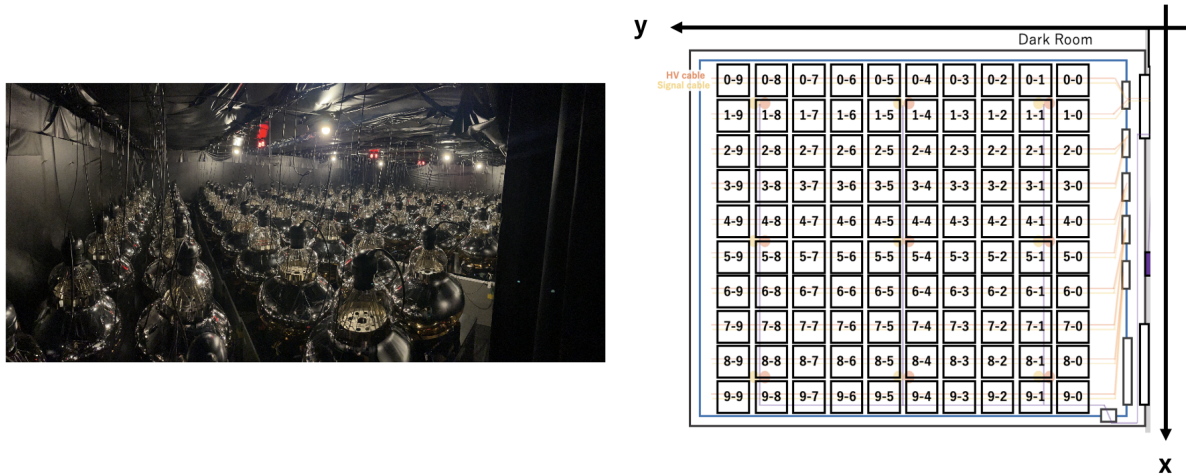


Figure 3.2. A view of the darkroom where PMTs are installed (left) and PMTs arrangement (right). There is another darkroom next to this room.

Figure 3.3 shows the time variation of temperature inside the dark room. The temperature inside the dark rooms is almost stable during the measurement because the rooms are well insulated and air conditioners work. Seasonal temperature changes are also within a range of about five degrees Celsius.

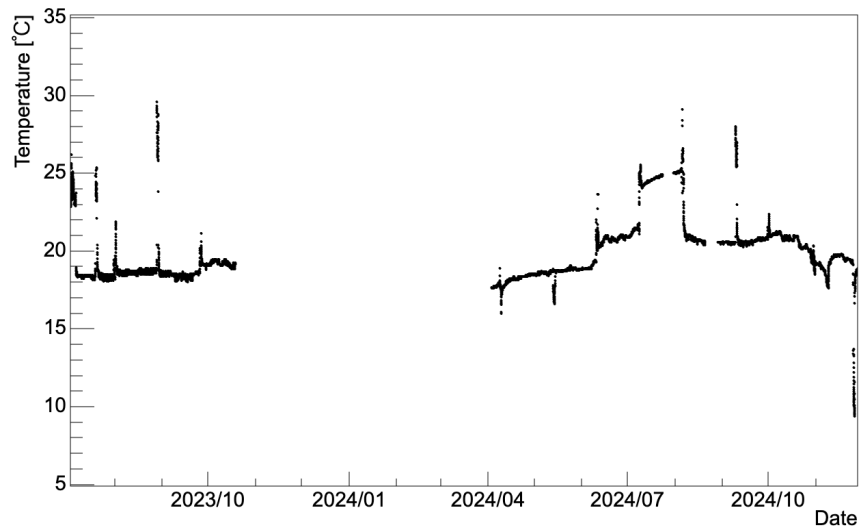


Figure 3.3. Time variation of temperature inside the dark room. The points where temperature changes like a spike correspond to when the darkroom was opened for PMT replacement. There are no data between November 2023 and March 2024 due to the problem of the thermometer.

As an electronics module for DAQ, QTC-Based Electronics with Ethernet (QBEE) [21], which is the electronics module used in SK since 2008, is used. One QBEE has 24 channels, and each channel consists of a custom charge-to-time converter (QTC) and a multi-hit time-to-digital converter (TDC). The charge and time resolutions are 0.2 pC and 0.1 ns, respectively. The charge dynamic range is 0.2 to 2500 pC. In this measurement, the trigger threshold voltage is set to  $-1$  mV, which is equivalent to 1/6 of typical pulse height of a single photoelectron signal,  $-6$  mV. Similarly for high voltage source (HV module), those used in SK, EDS made by iSeg, are also used. The voltage applied to each PMT is set to the value to achieve a gain of  $1 \times 10^7$ , which is determined by HPK. One HV module has 24 channels and can supply voltage of 2.5 kV at maximum. Ten QBEEs and ten HV modules are used, and about 20 PMTs are connected to each QBEE and HV module. Figure 3.4 shows which PMTs in each room are connected to which QBEE and HV modules.

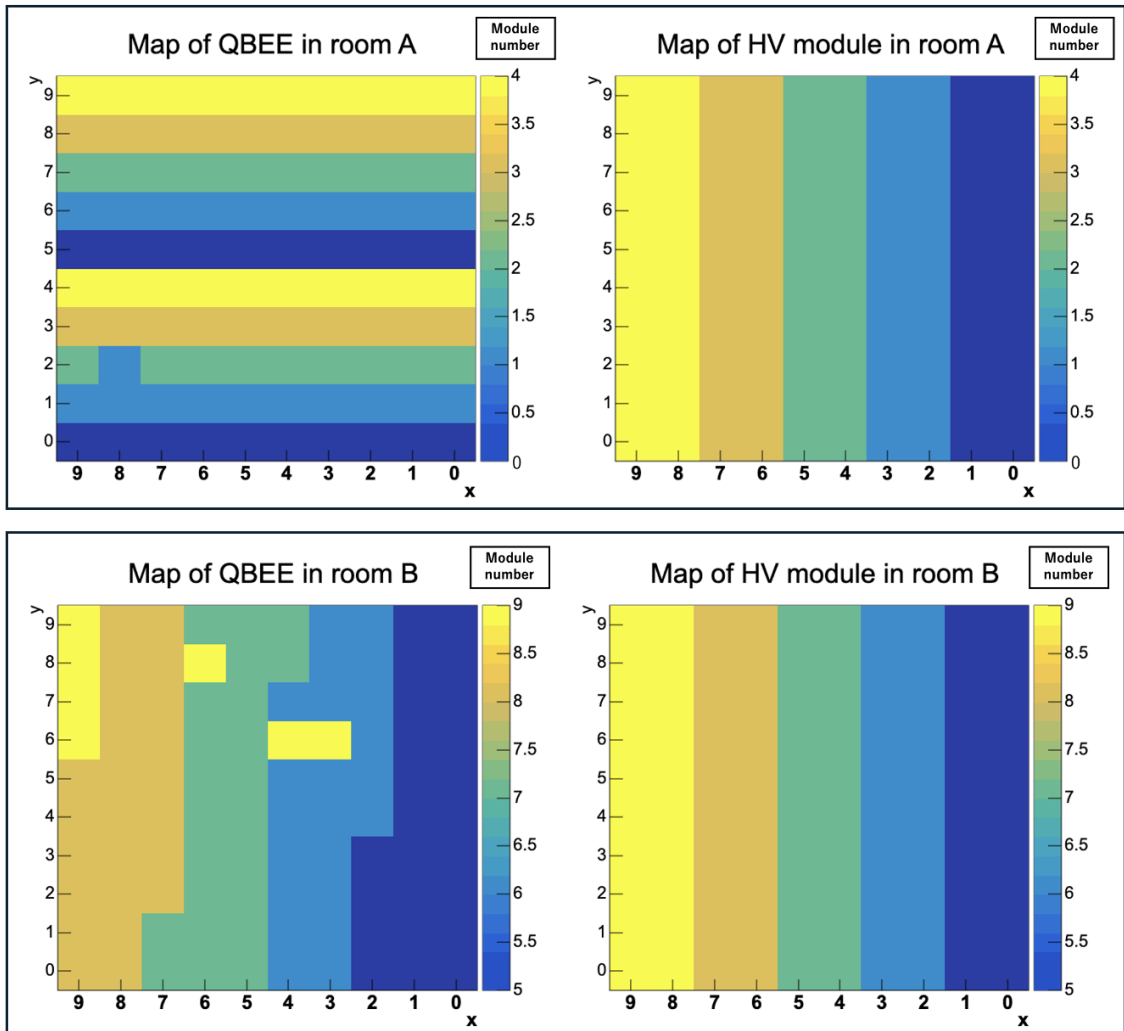


Figure 3.4. Map indicating which PMTs in each room are connected to which QBEE and HV modules. Top (Bottom) left is for QBEEs in room A (B) and top (bottom) right is for HV modules in room A (B).

The temperature of the place where the electronics modules locate is not controlled. Figure 3.5 shows trends of temperatures of 10 QBEEs between February 2024 and October 2024 (data before February 2024 were not stored and therefore could not be checked). From this figure, the minimum temperatures were about 15 °C in winter and the maximum temperatures were about 35 °C, so the temperature differences were more than 20 °C in some modules. However, the QTC of QBEE was tested to operate within an ambient temperature range of 26 °C to 44 °C [22], and QBEE includes a temperature correction system [21]. Therefore, it is considered that these temperature variations do not have a significant impact on the measurement of dark rate.

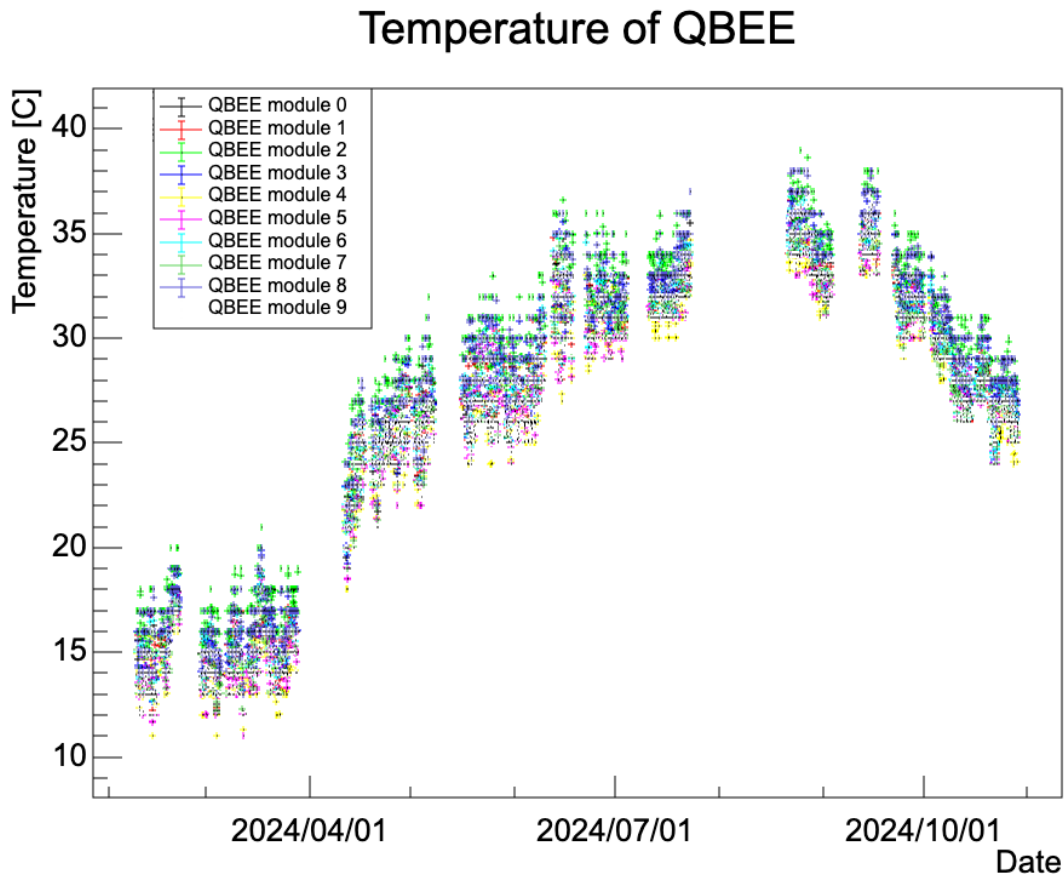


Figure 3.5. Trends of temperatures of 10 QBEEs between February 2024 and October 2024.

### 3.3.2 Data analysis

Dark rate of each PMT is calculated every one minute from the total number of signals counted with QBEE. In this set up, there is no system for shielding the geomagnetic field, and it affects the dark rate of each PMT. Taking this into account, the magnetic field at each PMT location is measured and corrected for dark rate using that value [23]. In stable PMTs, the dark rate is as shown in the left of Fig. 3.6. On the other hand, when the PMT has a problem, the dark rate will fluctuate wildly as shown in the right of Fig. 3.6.

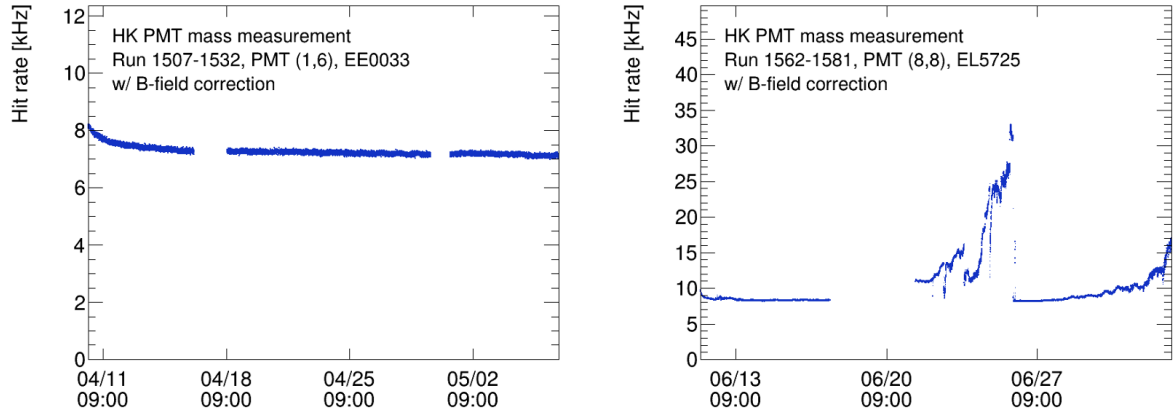


Figure 3.6. Examples of time variation of dark rate. The left is stable PMT. The right is unstable PMT and fails the criterion 2 and 3.

In addition, a high dark rate exceeding 10 kHz is also a problem as mentioned in Sec.3.2.1. Therefore, the dark rate and its stability are evaluated with the criteria as below;

1. Dark rate increases by more than 1 kHz within 1 minute and it does not go back to normal within 5 minutes.
2. Dark rate fluctuates by more than 0.5 kHz compared to the average of past 1 hour and it does not go back to normal within 5 minutes.
3. Dark rate increases by more than 0.5 kHz and the rate of neighboring PMT also increases by more than 0.5 kHz at the same time and the rate of  $>115$  p.e. charge hit also increases in the neighboring PMT.
4. Dark rate at 6 days after turning on HV exceeds 14.4 kHz.

A PMT meeting any one of the above criteria is considered to be a problematic PMT. The criterion 1, 2 and 3 are to detect the rate instability. The target of the criterion 1 is step rate increases and that of the criterion 2 is more moderate rate fluctuations including both rate increase and decrease. A PMT meeting the criterion 3 is counted as a flasher PMT. The criterion 4 is to judge if the dark rate of a PMT is too high or not. The value 14.4 kHz in the criterion 4 is determined taking account the effect of environmental radiation mentioned in Sec.3.2.1.

HK requires that the fraction of problematic PMTs is below 5% and that of flasher PMTs is below 1 %.

### 3.3.3 Result of mass measurement

Since July 2023, more than 2,000 PMTs have been measured. Table 3.1 and Table 3.2 are the breakdowns of the summary of each measurement period of 1-month measurements

and 3- or 6-month measurements, respectively. “C1-4” in the tables correspond to the criterion 1 to 4 and “Any” means the number of PMTs which meet any of the criteria. “Original” and “Improved” correspond to the number of original and improved PMTs measured in each period, respectively.

Table 3.1. Breakdown of the summary of each measurement period of 1-month measurements

Start date	End date	Room	# of measured PMT			# of problematic PMT					Fraction of problematic PMT [%]
			Original	Improved	Total	C1	C2	C3	C4	Any	
2023/7/7	2023/7/14	A	0	100	100	0	0	0	0	0	0
2023/7/7	2023/7/14	B	0	100	100	3	3	0	0	3	$3.0 \pm 1.7$
2023/7/20	2023/7/28	A	0	99	99	0	0	0	0	0	0
2023/7/20	2023/7/28	B	0	99	99	2	3	0	2	3	$3.0 \pm 1.7$
2023/8/4	2023/8/12	B	0	99	99	2	4	0	0	4	$4.1 \pm 2.0$
2023/8/29	2023/9/6	B	0	99	99	6	6	0	0	6	$6.1 \pm 2.4$
2023/9/26	2023/10/28	B	0	97	97	3	13	0	1	13	$13.4 \pm 3.5$
2023/11/2	2023/12/4	B	0	98	98	1	2	0	0	2	$2.0 \pm 1.4$
2023/12/6	2023/12/31	B	0	98	98	0	3	0	0	3	$3.1 \pm 1.7$
2024/1/10	2024/2/2	B	0	98	98	2	3	0	0	3	$3.1 \pm 1.7$
2024/2/8	2024/3/4	B	0	99	99	0	0	0	0	0	0
2024/3/6	2024/3/27	B	0	99	99	1	1	0	0	1	$1.0 \pm 1.0$
2024/4/10	2024/5/7	B	4	95	99	1	2	0	0	2	$2.0 \pm 1.4$
2024/5/15	2024/6/9	B	0	99	99	0	0	0	0	0	0
2024/6/11	2024/7/3	B	0	99	99	2	3	0	0	3	$3.0 \pm 1.7$
2024/7/10	2024/7/22	B	0	99	99	3	5	0	0	5	$5.1 \pm 2.2$
2024/8/21	2024/9/2	B	0	98	98	1	5	0	0	5	$5.1 \pm 2.2$
2024/9/11	2024/9/30	B	0	99	99	3	5	0	0	5	$5.1 \pm 2.2$
2024/10/2	2024/10/28	B	0	99	99	1	2	0	0	2	$2.0 \pm 1.4$
Total			4	1873	1877	31	60	0	3	60	$3.2 \pm 0.4$

Table 3.2. Breakdown of the summary of each measurement period of 3- or 6-month measurements

Start date	End date	Room	# of measured PMT			# of problematic PMT					Fraction of problematic PMT [%]
			Original	Improved	Total	C1	C2	C3	C4	Any	
2023/8/4	2023/10/28	A	0	99	99	0	0	0	0	0	0
2023/11/2	2024/2/2	A	0	99	99	0	1	0	0	1	$1.0 \pm 1.0$
2024/2/8	2024/7/22	A	97	0	97	3	5	0	0	5	$5.2 \pm 2.2$
2024/8/21	2024/10/28	A	0	96	96	2	3	0	0	3	$3.1 \pm 1.8$
Total			97	294	391	5	9	0	0	9	$2.3 \pm 0.8$

For these tables, we focus on two points; difference between the two dark rooms and difference between original and improved PMTs.

The first point is the difference between the two dark rooms. The fraction of problematic PMTs in room A, mainly used for 3- or 6-month measurements, in total is  $1.5 \pm 0.5\%$ , while that in room B, used for 1-month measurements, is  $3.6 \pm 0.5\%$ . This is unnatural because it is reasonable to assume that a longer measurement period would lead to more problematic PMTs appearing. Therefore, it is suspected that a part of problematic PMTs in room B are due to something originating from the measurement system. Figure 3.7 shows the position where problematic PMTs were detected. It is seen that the locations where problematic PMTs were detected are not uniformly distributed.

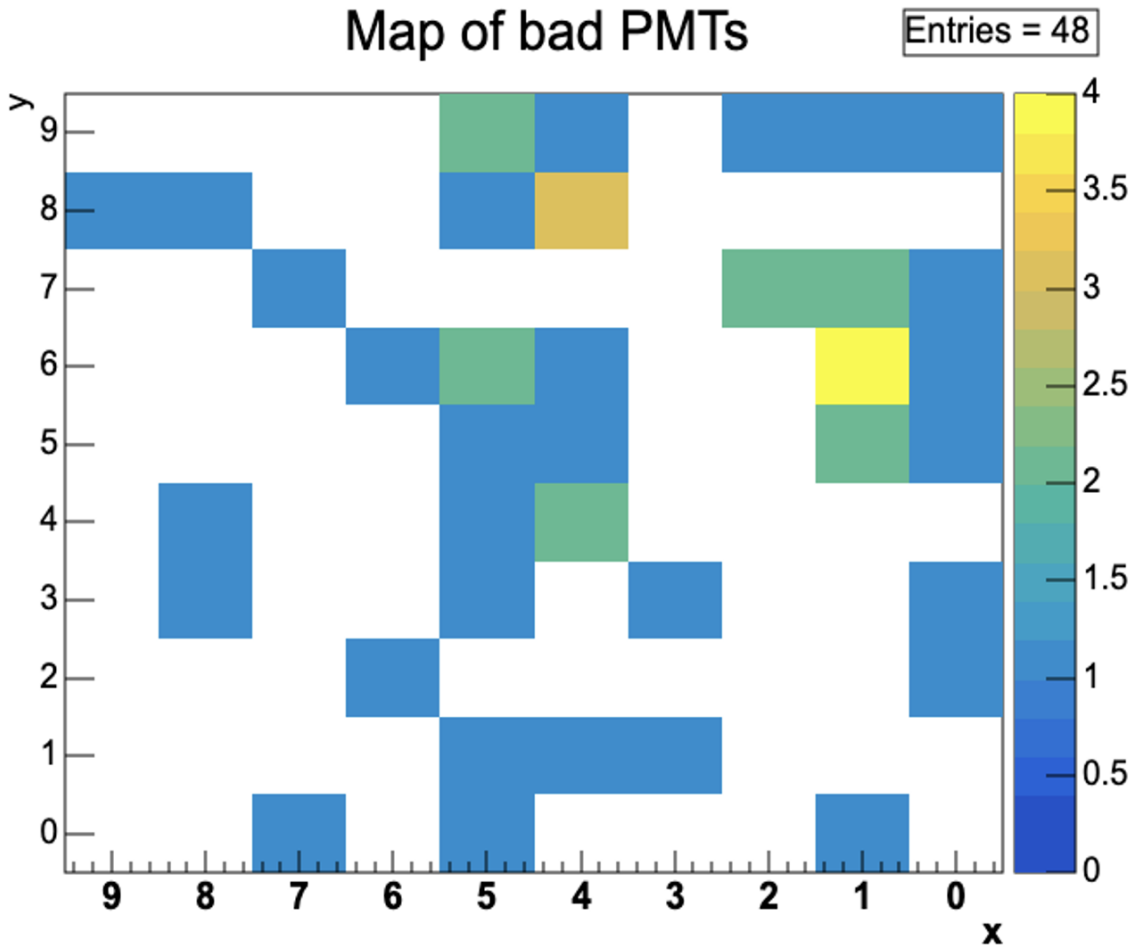


Figure 3.7. The position where problematic PMTs were detected in room B between July 2023 and July 2024.

Figure 3.8 shows the distribution of QBEE and HV modules where problematic PMTs connected in room B between July 2023 and July 2024. It is seen that module 5 and 7 of both QBEE and HV have a lot of problematic PMTs. As Fig. 3.4 shows, the distribution of QBEE and HV overlap significantly in room B, so if specific modules of either of QBEE or HV have many problematic PMTs, specific modules of the other could have also many problematic PMTs.

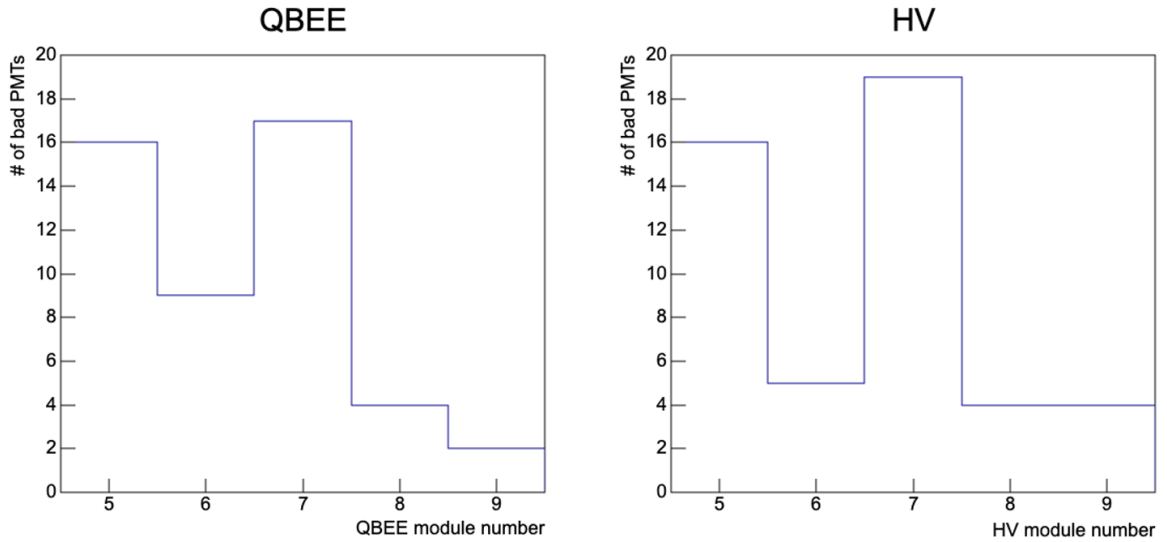


Figure 3.8. The distribution of QBEE and HV modules where problematic PMTs connected in room B between July 2023 and July 2024. Left is for QBEE and right is for HV module.

It is difficult to conclude whether the problem is in the position where the PMT is placed (or in the cables and connectors at that position) or in specific QBEE or HV modules, but one or some of these could be the cause of the more problematic PMTs in room B than in room A. Therefore, first, the module 5 and 7 of HV were exchanged to new ones on August 2024. Figure 3.9 shows the position where problematic PMTs were detected and Figure 3.10 shows the distribution of QBEE and HV modules where problematic PMTs connected in room B after replacement of HV modules. Compared to Figure 3.7 and Figure 3.8, there seems to be changes in positions where problematic PMTs appear and in the QBEE and HV modules connected to them. However, the number of problematic PMTs in room B after replacement of HV modules is only 12 and statistics are very small, so further measurements are needed.

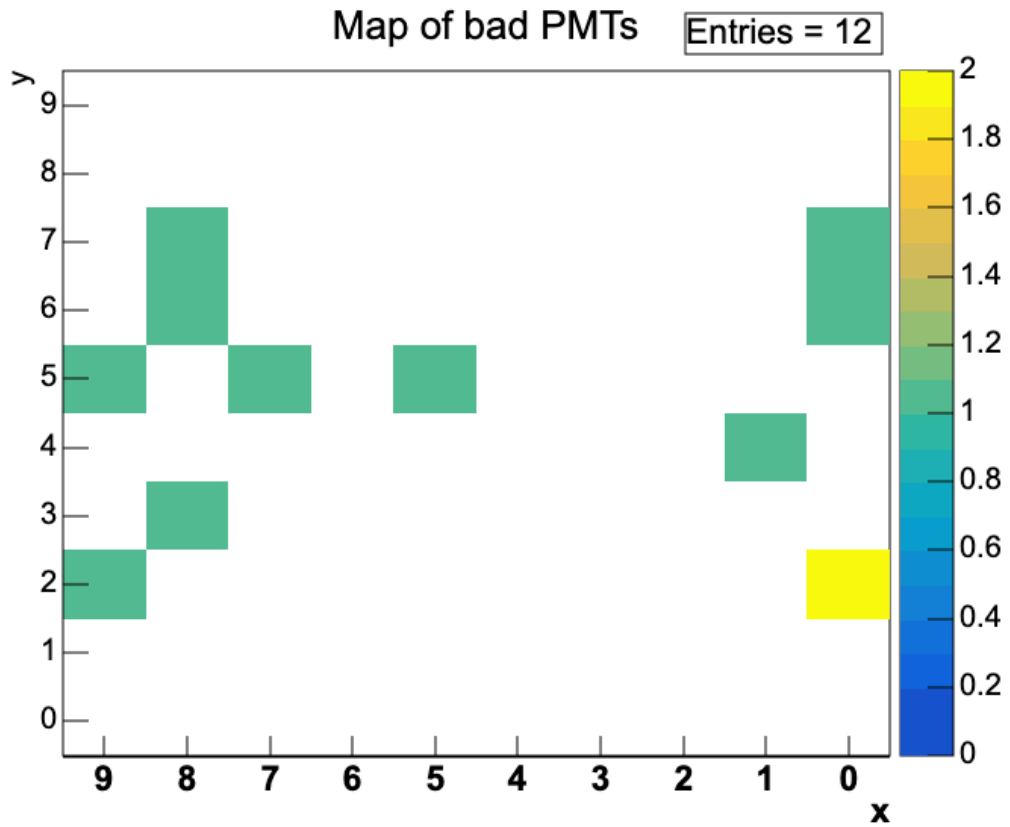


Figure 3.9. The position where problematic PMTs were detected in room B after replacement of module 5 and 7 of HV in August 2024.

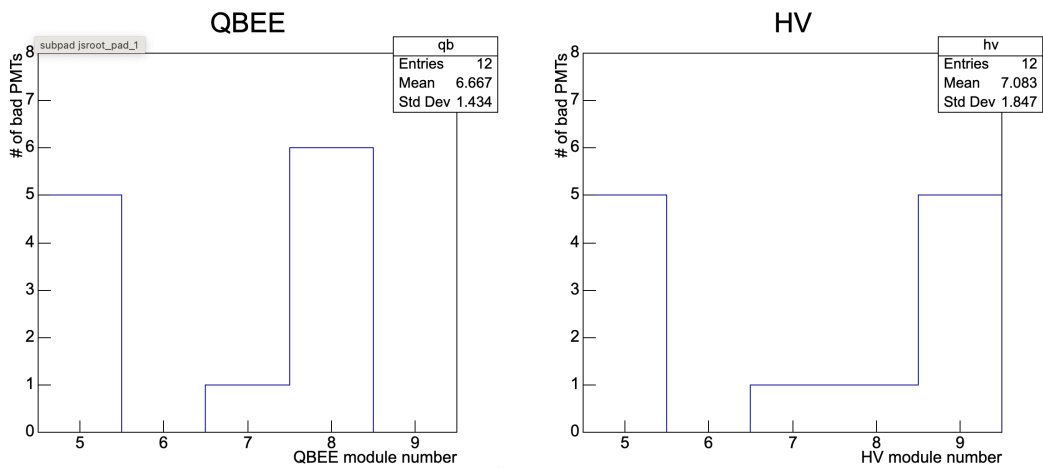


Figure 3.10. The distribution of QBEE and HV modules where problematic PMTs connected in room B after replacement of module 5 and 7 of HV on August 2024. Left is for QBEE and right is for HV module.

The other point is the difference between types of PMTs. As described in Sec.3.1.1, there are two types of PMT; “original” and “improved” PMT. As Table 3.2 shows, a 6-month measurement for 97 original PMTs was conducted from February 2024 to July 2024, while the other 3-month measurements were with only improved PMTs. In this period with only original PMTs, the fraction of problematic PMTs is higher than that in the other period with improved PMTs in room A. Therefore, original PMT may be more unstable than improve ones though both type of PMTs pass the screening test by HPK before delivery. However, original PMTs were measured only in a 6-month measurement while improved ones were measured only in 3-months measurement, so there is also a possibility that more problematic PMTs appear when improved PMTs are measured for longer than 3 months. In fact, the first three month of the 6-month measurement with original PMTs had two problematic PMTs and the other three problematic PMTs appeared in the latter three months. Therefore, the fraction of problematic PMTs was around 2 % during the first three months with original PMTs, which is similar to the 3-month measurement of the improved PMT. To investigate whether same trend appears in improved PMTs, 6-month measurements for improved PMTs also will be performed in future.

Although further investigation is needed about the problematic PMTs, even including them, the overall fraction of problematic PMTs and flasher PMTs are below 5 % and 1 %, respectively. This satisfies the requirement of HK mentioned in Sec.3.3.2.

### 3.3.4 Summary of mass-measurement

In order to assess PMT stability and manufactured quality with large statistics, up to 200 of the PMTs delivered each month are immediately measured. In this measurement, dark rate and its stability are evaluated for 1 to 6 months.

While the cumulative result satisfies HK’s requirement, several factors that could potentially cause issues, such as the setup and the type of PMT, have been found. Therefore, further investigation is needed.

## 3.4 long-term measurement of PMT

In mass-measurement, dark rate stability of PMTs is evaluated for 6 months at maximum. However, PMTs installed in the tank will continue to be operated for more than ten years and it is difficult to exchange them if they are out of order while operating. Therefore, we need to see the stability for longer term than mass-measurement. In addition, as mentioned in Sec.3.2.2, increase tendency of gain has been observed in SKPMT while long-term tendency of gain has not been checked so far in mass-produced HKPMT. Thus, it is also very interesting to see if HKPMT has similar trend in gain with SKPMT.

### 3.4.1 Experimental setup

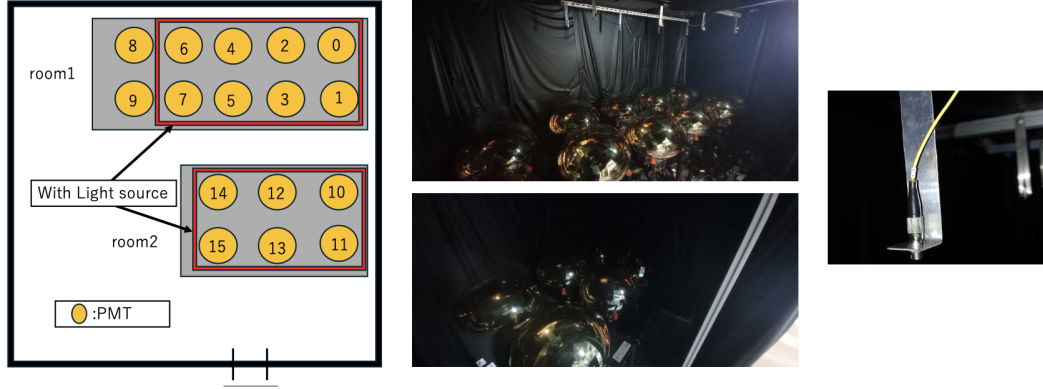


Figure 3.11. The overview of the setup of long-term measurement. The left is the PMTs and darkroom layout. The middle top is the larger dark room where 10 PMTs are set and the middle bottom is the smaller dark room where 6 PMTs are set. The right is one of the optical fibers fixed on each PMT for photon injection.

Figure 3.11 shows the overview of the setup for this measurement of 16 PMTs. Two dark rooms are located in a laboratory in the Kamioka underground. To cancel the geomagnetic field, coils are wrapped around both rooms. One of the two rooms accommodates 10 PMTs (CH0-9) and the other accommodates 6 PMTs (CH10-15). Figure 3.12 shows the time variation of temperature in the dark room. The temperature is approximately 24 °C and remains almost constant throughout the year, with fluctuations of up to about 1 °C.

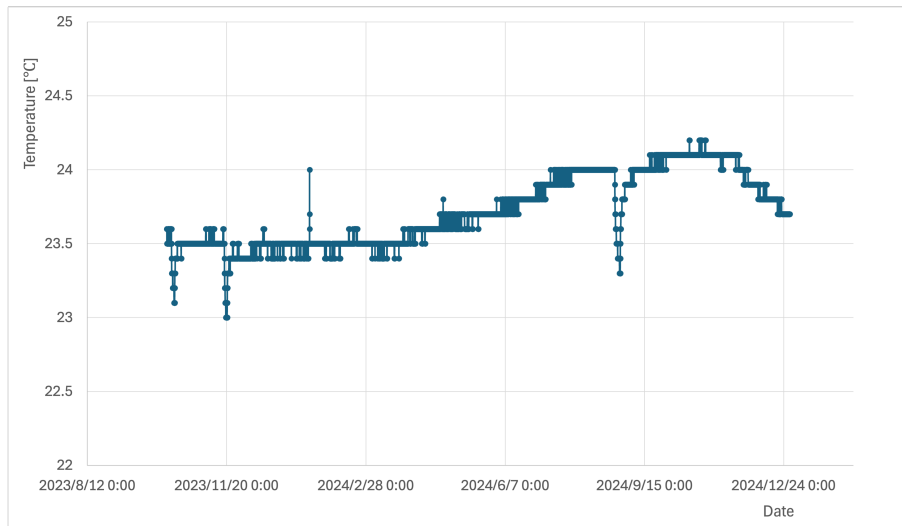


Figure 3.12. Time variation of temperature in the dark room. The points where temperature changes like a spike correspond to when the darkroom was opened for minor setup changes.

To obtain charge distributions for single photoelectron, optical fibers are fixed above 14 of the 16 PMTs and very weak light (about 0 to 1 photons/pulse) emitted from a laser oscillator outside the darkroom enters the PMT through the fibers. The wavelength of the laser is 405 nm and the light is injected to the PMTs at a frequency of 500 Hz. The probability of the PMT detecting a photon is about 10 to 20 % per pulse. Though this photon injection is continuously occurring throughout the measurement, the impact on the dark rate is small, with a maximum effect of about 0.1 kHz. Therefore, no correction is applied to the measured dark rate.

As a HV module, EDS made by iSeg are used as well as mass-measurement. The voltage applied to each PMT is set to the value to achieve a gain of  $1 \times 10^7$ , which is determined by HPK.

Figure 3.13 shows the DAQ system. Signals from PMTs are amplified with the amplifier by the factor of 10 and the amplified signal is divided into two. One of two is converted to a logic signal with the width of  $1 \mu\text{s}$  with the VME and NIM discriminators if the pulse height of a signal (signal has negative polarity) is higher than threshold. The VME discriminator is used to remotely and freely adjust the threshold and the NIM discriminator is used to widen the narrow (about 80 ns) output pulse by the VME discriminator to  $1 \mu\text{s}$ , which is of the order of the time window for a single event in HK. The threshold is set to  $-10 \text{ mV}$ , which is equivalent to  $1/6$  of typical pulse height of a single photoelectron signal,  $-60 \text{ mV}$  (this is value after amplified by the factor of 10). Then, number of pulses is counted with scalers for dark rate measurement. The other of the divided signal goes into the ADC and integrated charge of the signal is measured for gain measurement. The gate width of integration is 200 ns. From the start of measurement of gain to July 2024, ADC boards made by LeCroy (1182) were used, but they broke in July 2024. Therefore, CAEN's desktop digitizer (DT5730) has been used as a new ADC since August 2024. In December 2023, AC couplers were added to remove the offset voltage of the output of the amplifier. Table 3.3 is the list of equipments used for this measurement.

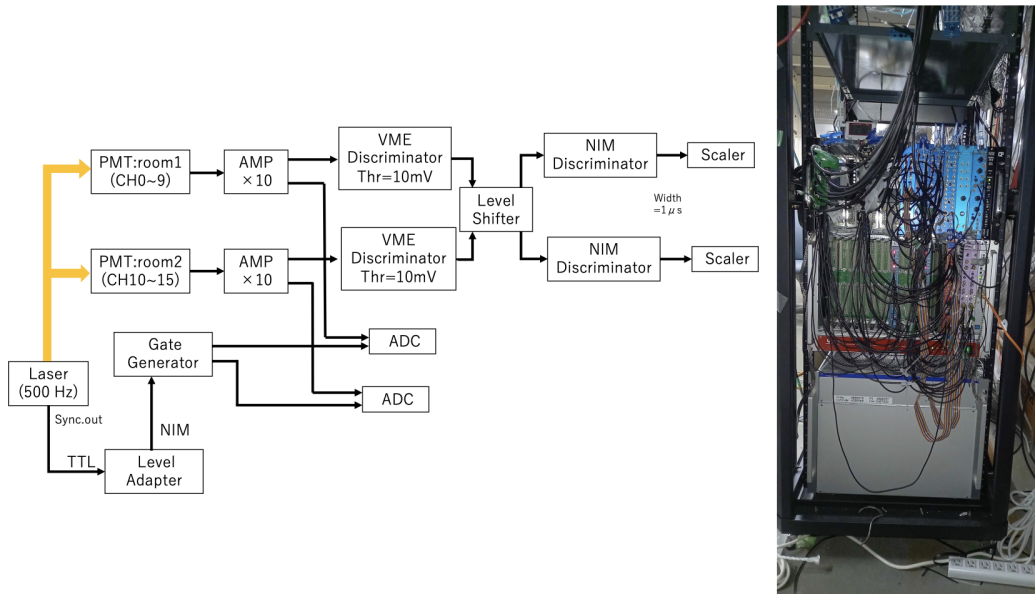


Figure 3.13. DAQ system. The left is the flowchart of how signals are processed. The right is the electric rack.

Table 3.3. List of equipment used for measurements

Use	Manufacture	Serial
Amplifier (for large room)	REPIC	RPN-092
Amplifier (for small room)	REPIC	RPN-093
Discriminator (VME)	CAEN	V814
Discriminator (NIM)	Kaizu Works	KN247A
Level shifter (ECL to NIM)	Kaizu Works	KN1840
ADC (until July 2024)	LeCroy	1182
ADC (since Aug 2024)	CAEN	DT5730
Scaler	REPIC	RPV-100
Gate generator	Kaizu Works	KN1500
Level adapter (TTL to NIM)	Kaizu Works	KN200
Laser oscilator	Hamamatsu Photonics	PLP-10 405 nm

### 3.4.2 Dark rate measurement

#### Data analysis

Dark rate of each PMT is calculated every one minute from the total number of signals counted with the scaler. The stability of dark rate is evaluated with the same criteria as mass measurement (see Sec.3.3.2) except for the criterion for flasher PMTs because the setup for this measurement does not take information of charge of each dark count.

## Result

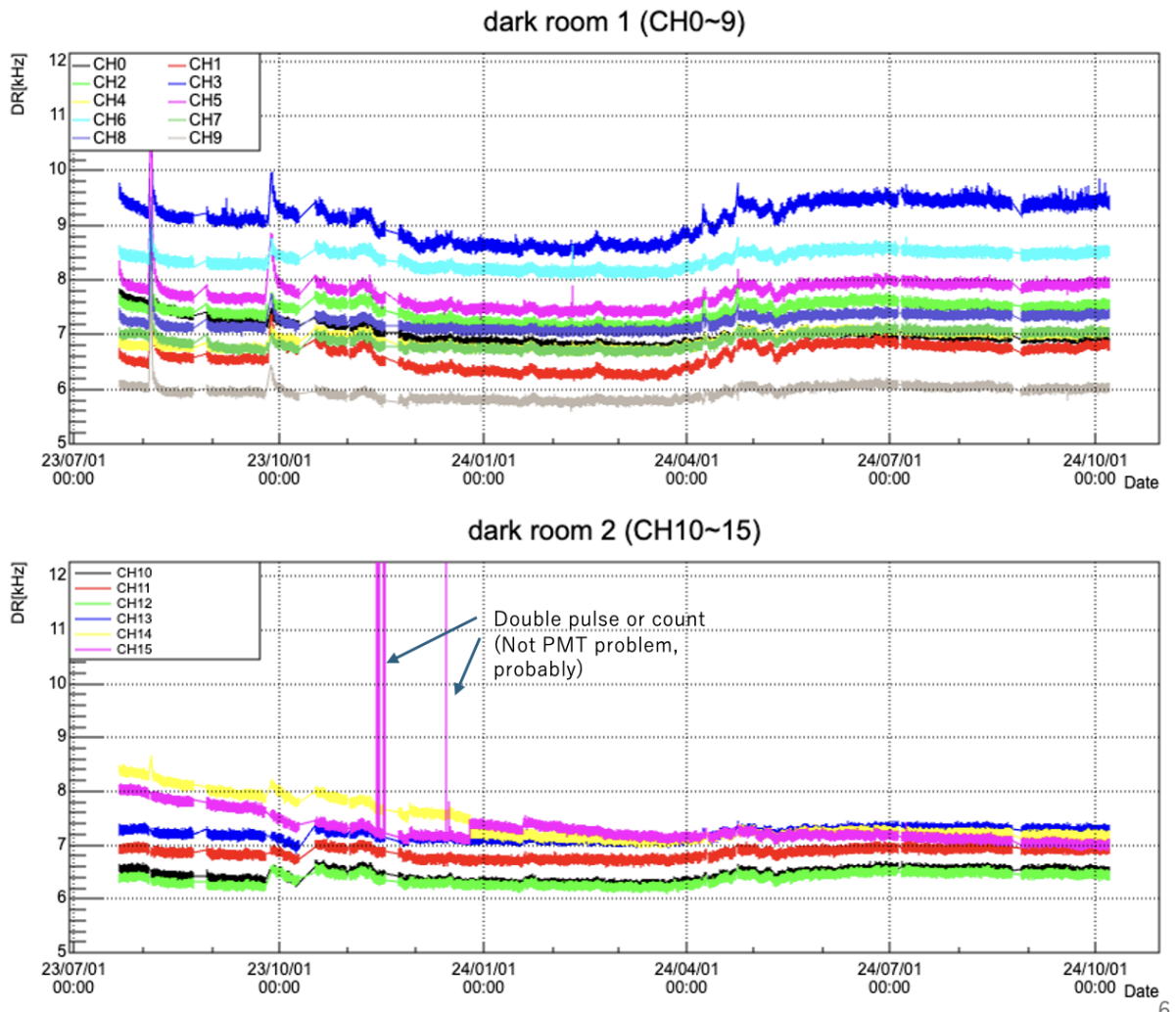


Figure 3.14. Time variation of dark rate. The top is dark rates of 10 PMTs in the larger dark room and the bottom is that of 6 PMTs in the smaller dark room.

Figure 3.14 shows the time variation of dark rate of each PMT from July 2023 to November 2024. There are some periods when large dark rate increase seen at the same time in all PMTs. These correspond to the periods immediately after dark rooms were opened for minor setup changes. As a result of applying the criteria to the time variation of dark rates, no PMTs are judged as problematic PMTs except CH15.

In CH15, rate jumps occurred sometimes in November and December 2023. During these rate jumps, dark rate became about 14 kHz and almost was constant. In normal time, dark rate of CH15 was about 7 kHz, so dark rate during rate jumps was almost exactly doubled compared with dark rate in normal time. To investigate the cause of this problem, CH14 and CH15 of the VME discriminator were swapped since December 25th. However, no similar events have appeared after CH14 and CH15 were swapped.

Except for those double rate, no problem has been observed. Given these circumstances, these rate instabilities in CH15 are not considered as a problem of PMT but a problem of electronics modules such as double pulse occurred in the discriminator or double counts in the scaler. Therefore, it is concluded that all PMTs work stably over a year in this setup.

While no PMTs are judged as problematic PMTs with the criteria, there seems gradual rate increase or decrease. These variations may be related with the environmental radiation by radon. Figure 3.15 shows the time variation of the radon concentration in the laboratory. The radon concentration in Kamioka underground is high and it has seasonal variations. Figure 3.16 shows the scatter plot of the average dark rate of 16 PMTs against the radon concentration. The correlation coefficient between the average dark rate and the radon concentration is 0.66. Therefore, the gradual variations in dark rates are considered to be due to fluctuations in radon concentrations.

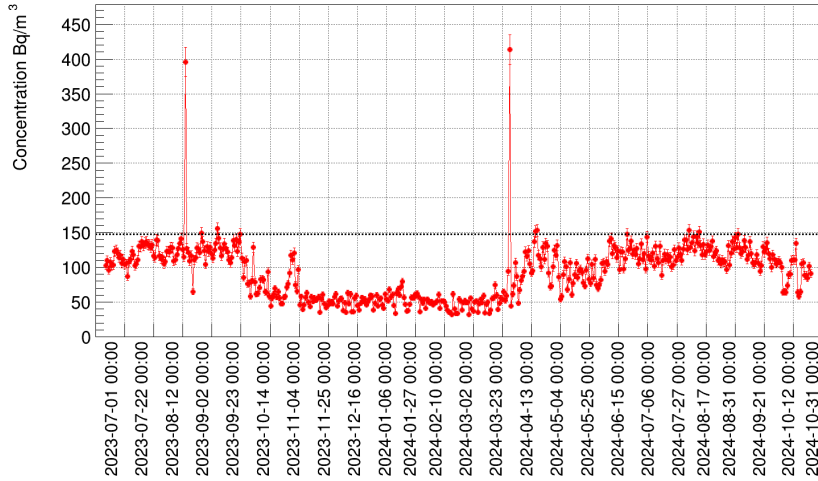


Figure 3.15. Time variation of radon concentration at the entrance of the laboratory.

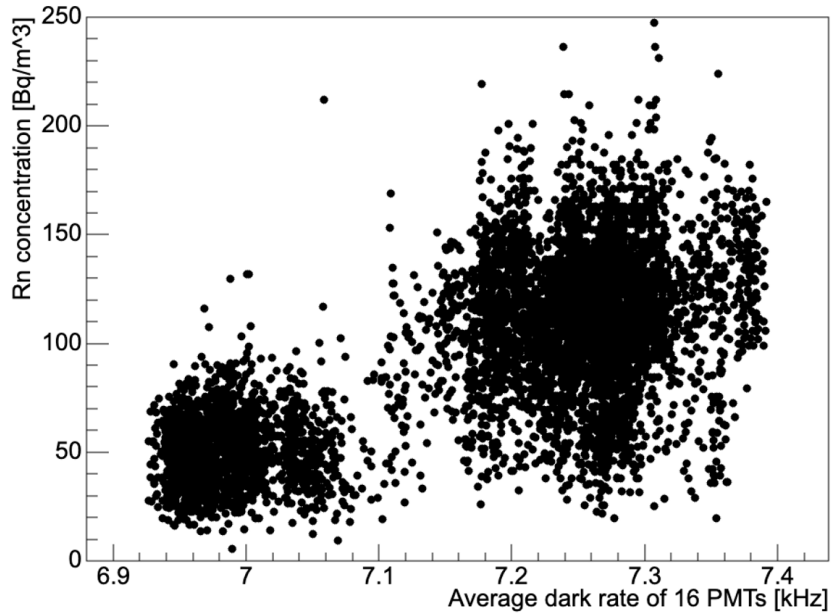


Figure 3.16. Scatter plot of the average dark rate of 16 PMTs against the radon concentration.

### 3.4.3 Gain measurement

#### Data analysis

Gain is obtained every day using the charge distribution. The flow to obtain the gain is as below;

1. Obtain charge distribution by the ADC for each PMT.
2. Smear the charge distribution and fit it with a function.
3. Judge whether the fit is successful or not.
4. If the fit is successful, calculate gain.

The charge information of photons injected from the optical fiber is obtained for each PMT every day by the ADC. The photon injection is conducted throughout the day, but only data for approximately 1.5 hours (3 million events) are collected to reduce data volume and computational resources.

The signal and the baseline of the ADC fluctuate due to the influence of noise from the electronics modules and the rack as shown in Fig. 3.17. These fluctuations distort the charge distribution, create multiple peaks, and make it difficult to capture the true single-photoelectron peak as shown in Fig. 3.18.

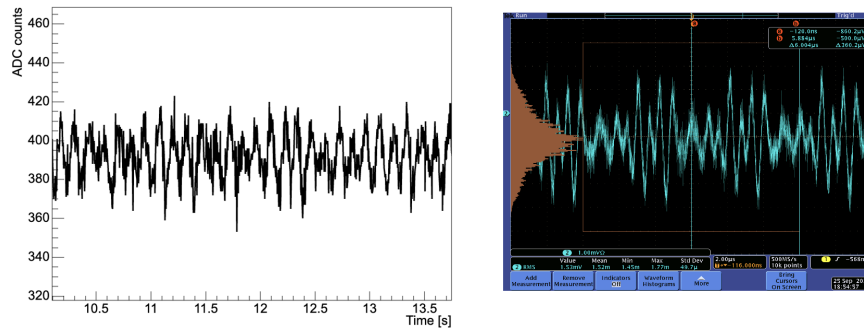


Figure 3.17. The baseline of the ADCs (left) and the signal (right) as a function of time. Periodic structures emerge due to noise.

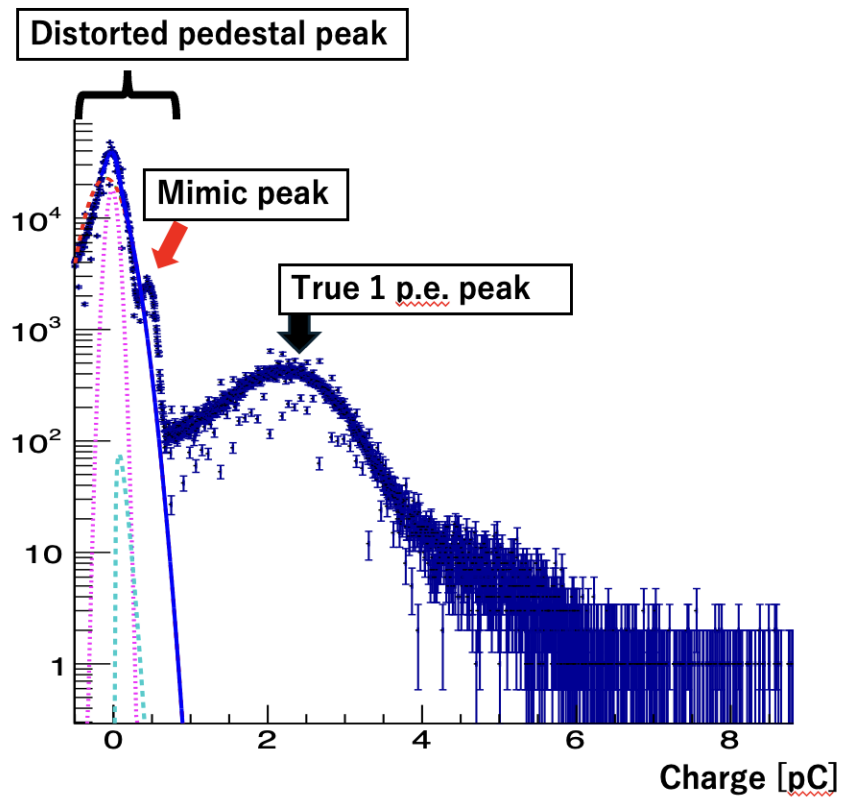


Figure 3.18. An example of a charge distribution distorted by noise. The pink, green, and light blue dotted lines show the first, second, and third term of Eq. (3.1), respectively. The red dotted curve shows the summation of the second and third term of Eq. (3.1).

Therefore, the obtained charge distribution is smeared by convoluting a Gaussian  $\sigma$  of which is 0.25 pC to reduce the effect of noise (see Fig. 3.19).

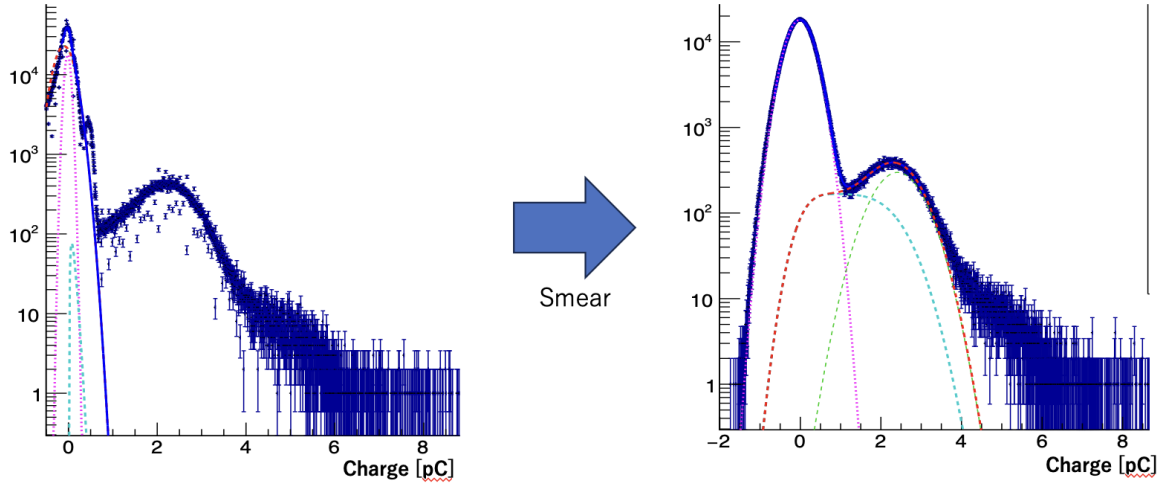


Figure 3.19. Smearing of charge distribution by Gaussian convolution.  $\sigma$  of the Gaussian is 0.25 pC. It can be seen that before smearing, the fitting described below failed due to distortion of the charge distribution caused by noise, and that smearing enables proper fitting. The pink, green, and light blue dotted lines in both distributions show the first, second, and third term of Eq. (3.1), respectively. The red dotted curve shows the summation of the second and third term of Eq. (3.1).

Charge distribution after smeared is fitted with a function as below;

$$\begin{aligned}
 \text{Fitting function} = & p_0 \exp \left\{ - \left( \frac{x - p_1}{\sqrt{2}p_2} \right)^2 \right\} \\
 & + p_3 \exp \left\{ - \left( \frac{x - p_4}{\sqrt{2}p_5} \right)^2 \right\} \\
 & + \frac{p_6 p_3}{2} \left\{ \text{erf} \left( \frac{x - p_1}{\sqrt{2}p_2} \right) - \text{erf} \left( \frac{x - p_4}{\sqrt{2}p_5} \right) \right\}.
 \end{aligned} \tag{3.1}$$

The first term is a Gaussian corresponding to the pedestal and the second term is a Gaussian corresponding to one photoelectron (1 p.e.) peak. The third term is a function that takes into account incomplete amplification due to inelastic scattering at the dynode, etc. Figure 3.20 shows how to obtain gain from charge distribution.

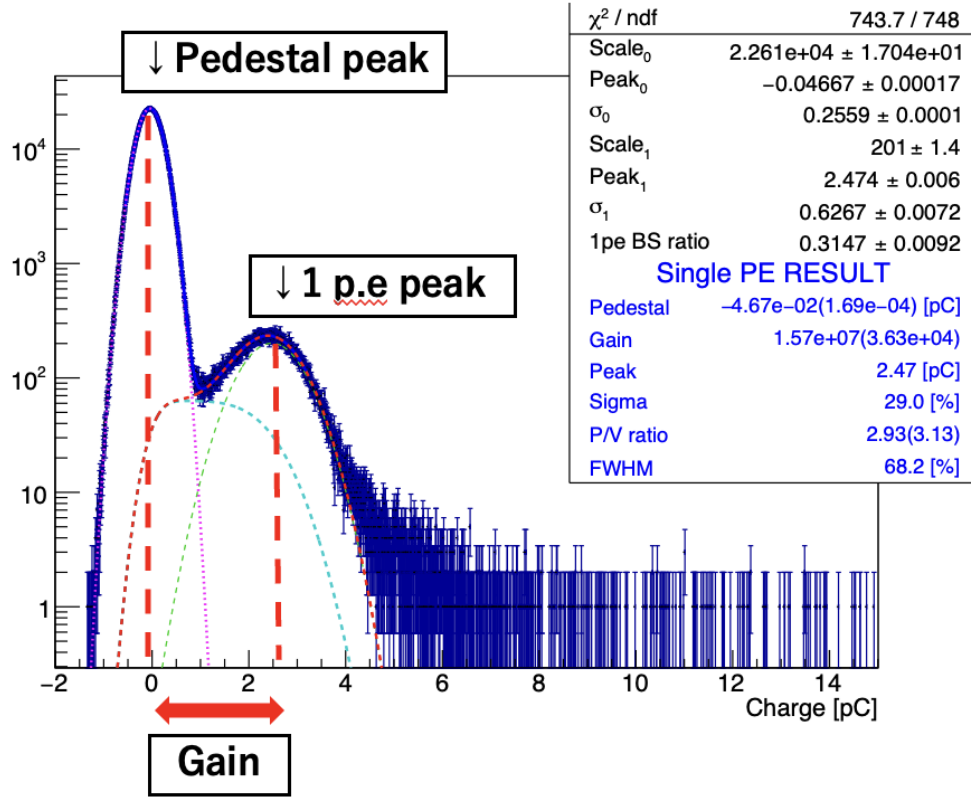


Figure 3.20. How to obtain gain from charge distribution. The pink, green, and light blue dotted lines show the first, second, and third term of Eq. (3.1), respectively. The red dotted curve shows the summation of the second and third term of Eq. (3.1).

Then, gain is calculated from

$$\text{Gain} = \frac{p_4 - p_1}{1.602 \times 10^{-19}}. \quad (3.2)$$

To exclude cases where fitting was unsuccessful due to the influence of noise or other factors, a fitting result is excluded if the value of  $\chi^2$  falls outside the 0.5% to 99.5% confidence interval of the chi-squared distribution with  $n$  degrees of freedom. The probability that the fitting is unsuccessful depends on the noise in each channel, but it is about 0 to 10 %.

The above process is carried out daily, and the gains has been measured over a year.

As mentioned in Sec.3.4.1, ADCs for gain measurement were replaced on August 2024 and new one and previous ones are not same. To calibrate the difference between the different ADCs, the average of the data taken from August 7th to 10th is used for correction. That data is compared with the predicted gain on that dates by extrapolating the data with previous ADCs. Figure 3.21 shows how to obtain the correction factors and Table 3.4 is the calculated correction factors.

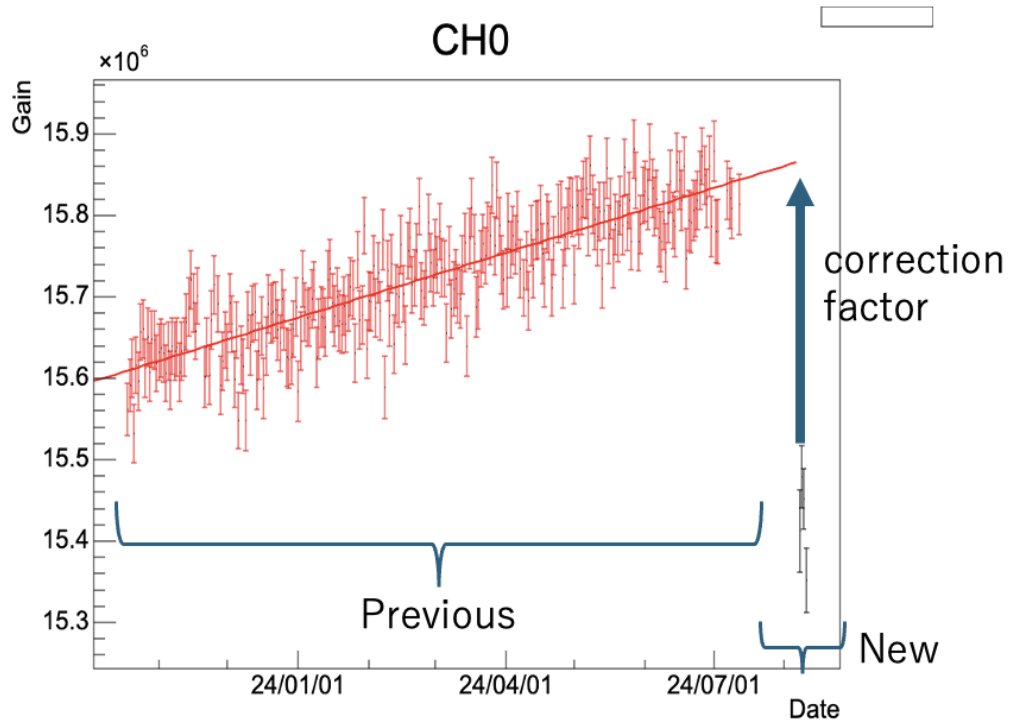


Figure 3.21. How to obtain correction factors between new ADC and previous ADC.

Table 3.4. List of correction factors

CH	Correction factor
0	$\times 1.029$
1	$\times 1.032$
2	$\times 1.044$
3	$\times 1.035$
4	$\times 1.044$
5	$\times 1.034$
6	$\times 1.040$
7	$\times 1.058$
10	$\times 1.022$
11	$\times 1.013$
12	$\times 1.015$
13	$\times 1.020$
14	$\times 1.010$
15	$\times 1.019$

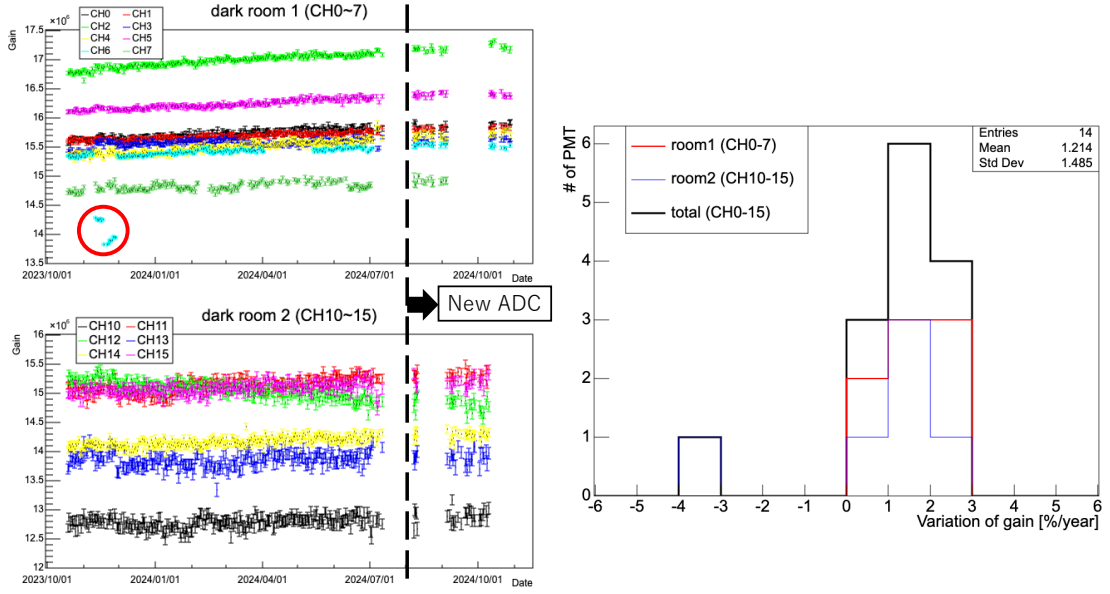


Figure 3.22. Time variation of gain. The left top shows the gain of 8 PMTs in the larger dark room and the left bottom shows the gain of 6 PMTs in the smaller dark room. The right is the distribution of change rate of gain per year when the gain of each PMT at the beginning of the measurement is set to 1. In CH6, data from November 11<sup>th</sup> to November 28<sup>th</sup> (red circle) were rejected when calculating the variation of the gain due to a clear abnormal gain caused by a cable connection problem.

The left figures (top, bottom) of Fig. 3.22 shows time variation of gain of each PMT from October 2023 to November 2024. In CH6, data from November 11th to November 28th (red circle in the left top figure) were clearly abnormal. This was due to bad cable attachment and was recovered after reconnecting cables. This abnormal period of CH6 was rejected when calculating gain variations. The right figure is the distribution of change rate of gain per year when the gain of each PMT at the beginning of the measurement is set to one. As this distribution shows, most PMTs measured in this measurement have increase tendency of gain and the average of the change rate of gain is

$$\text{Average of gain change} = 1.3 \pm 0.4 \text{ \%/year.} \quad (3.3)$$

A trend of increasing gain is observed in mass produced HKPMTs as well as SKPMT.

The gain of one PMT (CH12) has decreasing tendency. As explained in Sec.3.2.2, the variation of gain is thought to be due to the change of the amount of cesium in the dynode during operation and there are individual differences. In fact, some SKPMTs have decreasing tendency of gain.

### 3.4.4 Summary of long-term measurement

In long-term measurement, dark rate and gain of 16 PMTs have been monitored since July 2023 and October 2023, respectively.

Dark rates have remained stable over a year. Although the number of PMTs measured is small and the statistics are limited, based on this result, it is unlikely that the number of PMTs that become unstable during operation will drastically increase within one year.

For gain, increasing tendency of  $1.3 \pm 0.4$  %/year has been observed and this is a similar trend with SKPMT. Therefore, regular gain measurements will be required during operation of HK to apply corrections during analysis.

### 3.5 Summary and discussion of stability evaluation of PMT

After mass production of HKPMT began in 2020, problems about the stability of the dark rate were identified and actions have been taken such as improving the PMTs and performing pre-shipping screening tests by HPK. In addition, a long-term increase in gain has been observed in SKPMTs, and it was necessary to check whether the same phenomenon occurs in HKPMTs. Based on these backgrounds, two types of measurements have been conducted since July 2023; mass-measurement of dark rate and long-term measurement of dark rate and gain.

As for the evaluation of the gain change in long-term measurement, increasing tendency has been observed. This is a similar trend with SKPMT.

As for the evaluation of dark rate and its stability in both mass-measurement and long-term measurement, the cumulative result of mass-measurement and the result of long-term measurement satisfy HK's requirement. However, more consideration is required when considering a 10- or 20-year operation of HK. Even if the fraction of problematic PMTs is within 5 % over measurements conducted for 1 to 6 months, this does not guarantee that the fraction will not change significantly over 20 years of operation. In long-term measurement, no problematic PMTs were found, but that was still only a year. Since it is impossible to conduct a 20-year measurement, fundamentally solving this issue is difficult, but it may be possible to reduce the risk by additional evaluation criteria or measurement methods. For example, the current HK's requirement only considers the number of problematic PMTs, but a PMT that was unstable for a very short time differs in operational impacts for HK from one that remained unstable from the moment the problem occurred until the end of the measurement. Additionally, measuring at a voltage higher than the specification may serve as an accelerated test.

# Chapter 4

## Evaluation of proton decay search sensitivity for Hyper-Kamiokande

Nucleon decay is one of the main physics targets of HK. In particular, the mode that a proton decays into a positron and a neutral pion ( $p \rightarrow e^+\pi^0$ ) is one of the main decay modes predicted in many GUTs and have been searched by various experiments. The mode of  $p \rightarrow e^+\pi^0$  is good for experimental search because the signal of this mode is simple and distinctive.

In this chapter, the sensitivity to  $p \rightarrow e^+\pi^0$  in HK is evaluated. The sensitivity to  $p \rightarrow e^+\pi^0$  in HK was also estimated in [14], but it was based on the software used in SK. This thesis represents the first attempt using software developed for HK. There are some incomplete aspects in the tuning and development, and those points are mentioned in each section.

### 4.1 Monte Carlo Simulation

The Monte Carlo simulation (MC) of the proton decay and background events in HK is carried out in the following order; the decay and interactions inside the nucleus, propagation of particles inside the detector, and the detector response when Cherenkov photons are observed by the PMTs.

#### 4.1.1 Event generation

##### Proton decay simulation

In this analysis, it is assumed that proton decay equally happens in each proton of  $\text{H}_2\text{O}$  which contains two proton in hydrogen nuclei and eight protons in oxygen nuclei.

Protons in hydrogen are called “free protons” and assumed to be at rest. Since free protons are at rest and do not interact with other particles, the electron and neutral pion are emitted back to back when a free proton decays and each of them has a monochromatic momentum of  $459.43 \text{ MeV}/c$ . A  $\pi^0$  decays into two gamma rays immediately after generated.

On the other hand, protons in oxygen are called “bound protons”. On bound protons, there are effects of the Fermi momentum, nuclear binding energy, and collisions with other surrounding nucleons. The ratio of protons in  $s$ -state to those in  $p$ -state is set to 1:3 based on the nuclear shell model [24]. The Fermi momentum of a nucleon in  $^{16}\text{O}$  is distributed based on electron- $^{12}\text{C}$  scattering data [25]. The binding energy is distributed as a Gaussian with a mean of 39.0 MeV (10.2 MeV) and a sigma of 15.5 MeV (3.82 MeV) for  $s$ -state ( $p$ -state) protons. The effective proton mass is calculated by subtracting the binding energy from the proton mass. When the wave function of a proton is overlapping with that of the other surrounding nucleon during the decay, this decay becomes a two-body system decay, named “correlated decay”. The probability of correlated decay in bound proton decays is predicted to be about 10 % based on [26]. Figure 4.1 shows the distributions of the simulated momentum and effective mass of protons [15].

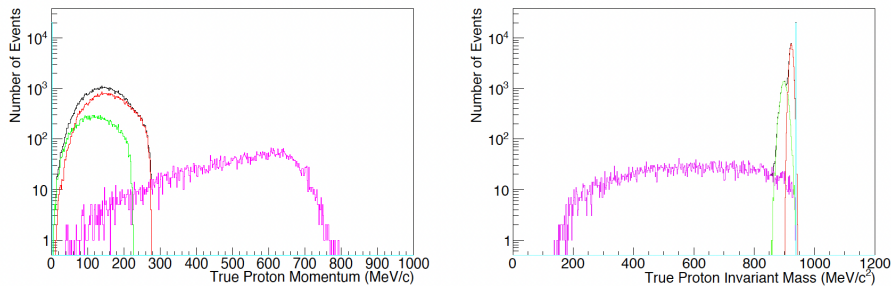


Figure 4.1. Distributions of simulated initial momentum (left) and effective invariant mass (right) of protons. The cyan, black, green, red and purple histograms correspond to free, bound,  $s$ -state,  $p$ -state and correlated decay protons, respectively. Taken from [15].

The interactions with the nucleons in an oxygen are also considered for the particles emitted from a decayed proton. While a positron generated in  $^{16}\text{O}$  escapes from nucleus without any interaction, a  $\pi^0$  interacts hadronically with nucleons. These interactions are called the pion final state interactions ( $\pi$ -FSI) and simulated in NEUT [27]. NEUT is a neutrino-nucleus interaction simulation program library. NEUT is used for not only simulation of neutrino-nucleus interactions but also nucleon decay simulations because it can extensively simulate the interactions between nucleons and hadrons generated within the nucleus. In NEUT, a custom semi-classical intranuclear cascade model [28] is used to simulate  $\pi$ -FSI. The interaction positions are determined using a Woods–Saxon nucleon density function [29]. Table 4.1 shows the breakdown of the fraction of the types of  $\pi$ -FSI in the sample of proton decay used in this analysis.

Table 4.1. Breakdown of the fraction of the types of  $\pi$ -FSI

No interaction	Charge exchange	Scattering	Absorption
$34.6 \pm 0.2 \%$	$14.9 \pm 0.2 \%$	$22.2 \pm 0.2 \%$	$28.3 \pm 0.2 \%$

## Background simulation

For the background events of  $p \rightarrow e^+\pi^0$ , only atmospheric neutrinos are assumed because there are no other considerable backgrounds. In this analysis, the atmospheric neutrino flux at SK calculated based on the Honda model [30][31], called ‘‘Honda flux’’ is used because the flux at HK has not been calculated yet. Figure 4.2 shows the Honda flux. The flux by other models from the FLUKA [32] and the Bartol [33] are plotted together.

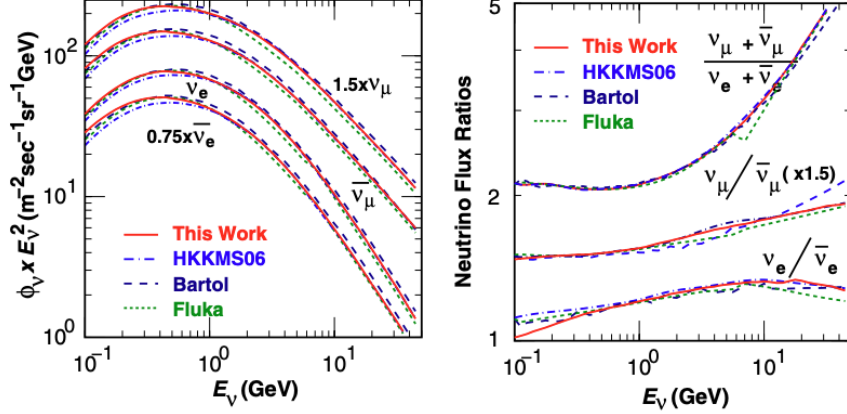


Figure 4.2. Direction-averaged atmospheric neutrino flux at SK by the Honda flux (red) and other models (blue, black, and green). The absolute flux is on the left and the the flux ratio is on the right. Taken from [30].

The interactions of neutrinos with water are simulated by NEUT [27]. In the atmospheric neutrino MC, the interactions of neutrinos with electrons are neglected because the cross section for neutrino-electron interaction is three orders of magnitude smaller than that for neutrino-hadron interactions. The neutrino interactions include two types; Charged Current (CC) interactions mediated by the  $W$  boson and NC interactions mediated by the  $Z$  boson. In both CC and NC interactions, there are three main types of reactions; Quasi-Elastic (QE) scattering, resonant productions, and Deep Inelastic Scattering (DIS). Figure 4.3 shows the distributions of the CC  $\nu_\mu$  and  $\bar{\nu}_\mu$  cross sections per nucleon as a function of neutrino energy simulated in NEUT and the experimental data [34].

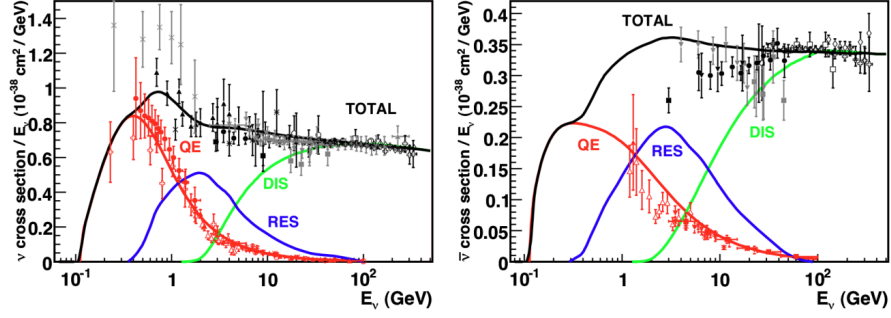


Figure 4.3. Distributions of CC  $\nu_\mu$  (left) and  $\bar{\nu}_\mu$  (right) cross sections per nucleon as a function of neutrino energy simulated in NEUT (solid lines) and the experimental data (dots). Taken from [34],

CCQE and NCQE are the dominant interactions in the region of the neutrino energy below 1 GeV. CCQE is described as below;

$$\text{CCQE} : \nu + N \rightarrow l + N', \quad (4.1)$$

and NCQE is as below;

$$\text{NCQE} : \nu + N \rightarrow \nu + N, \quad (4.2)$$

where  $N$  and  $N'$  are the initial and final nucleons, and  $l$  is the lepton. The scattering with multiple nucleons as below also exists;

$$\nu + NN' \rightarrow l + N'N'', \quad (4.3)$$

where  $NN'$  and  $N'N''$  are the combinations of initial and final nucleons, respectively.

In the resonant production, a single meson or photon is produced by the barion resonance through neutrino interactions as follows;

$$\nu + N \rightarrow l + N' + (\pi, K, \gamma, \eta). \quad (4.4)$$

The coherent pion production, where a neutrino interacts with the entire atomic nucleus and produces pions, also occurs;

$$\nu + {}^{16}\text{O} \rightarrow l + {}^{16}\text{O} + \pi. \quad (4.5)$$

$\nu_e$ CC events with 1  $\pi^0$  become the dominant backgrounds for  $p \rightarrow e^+\pi^0$  because the particles generated in  $\nu_e\text{CC}1\pi^0$ , an electron and a  $\pi^0$ , are same as those in  $p \rightarrow e^+\pi^0$ .

DIS is the dominant process in a high energy region above around 10 GeV. Such a high energy neutrino interacts with quarks and gluons and generate hadrons as below;

$$\nu + N \rightarrow l + N' + \text{hadrons}. \quad (4.6)$$

### 4.1.2 Propagation of particles in water

How the detector works when particles are emitted by proton decay and neutrino reactions in HK is simulated by a simulator named WCSim [35]. WCSim is a Geant4-based Monte Carlo simulation tool for developing and simulating large water Cherenkov detectors. The Geant4 is a simulation package widely used in high-energy physics that can accurately simulate the interaction of particles as they pass through matter [36].

The propagation of particles in water is simulated with the FTFP\_BERT package [36] of the Geant4. The propagation of Cherenkov photons in water is simulated considering the attenuation and scattering in the water.

### 4.1.3 Detector response

When Cherenkov photons reach the PMTs, a part of them are registered as hits, taking into account the detection efficiency of the PMTs. The hits are digitized based on the electronics scheme used in SK until 2001 [37], because the electronics module for HK and the QBEE (see 3.3.1) are not implemented in WCSim now. The disadvantage of this old scheme is its inability to tag neutrons. In SK, while the difference in the electronics had little impact on the detection efficiency of the signal events of  $p \rightarrow e^+\pi^0$ , the number of backgrounds with the old electronics scheme is about twice as large compared to that with QBEE, which is capable of neutron tagging [12]. Since neutron tagging is not used in this analysis, there is still room for improvement in the number of backgrounds.

The event trigger is issued when the number of digitized hits exceeds 37 in a sliding time window of 200 ns. Charge and time information of hits in a time window of  $-450 \text{ ns} < T_{trigger} < 950 \text{ ns}$  are saved, where  $T_{trigger}$  is the time when the trigger is issued. In this thesis, the dark rate is assumed to be 4.2 kHz, the same level as SKPMT, and random hits are added to each PMT within the time window so that the average becomes 4.2 kHz.

Figure 4.4 is the event display of a  $p \rightarrow e^+\pi^0$  event. The white-bordered circle and rectangle represent the unfolded view of the cylindrical tank of HK. The colorful dots in the figure represent the PMTs, and the color of each dot indicates the amount of charge detected by each PMT. Three Cherenkov rings formed by the positron and two gamma rays from the  $\pi^0$  are visible.

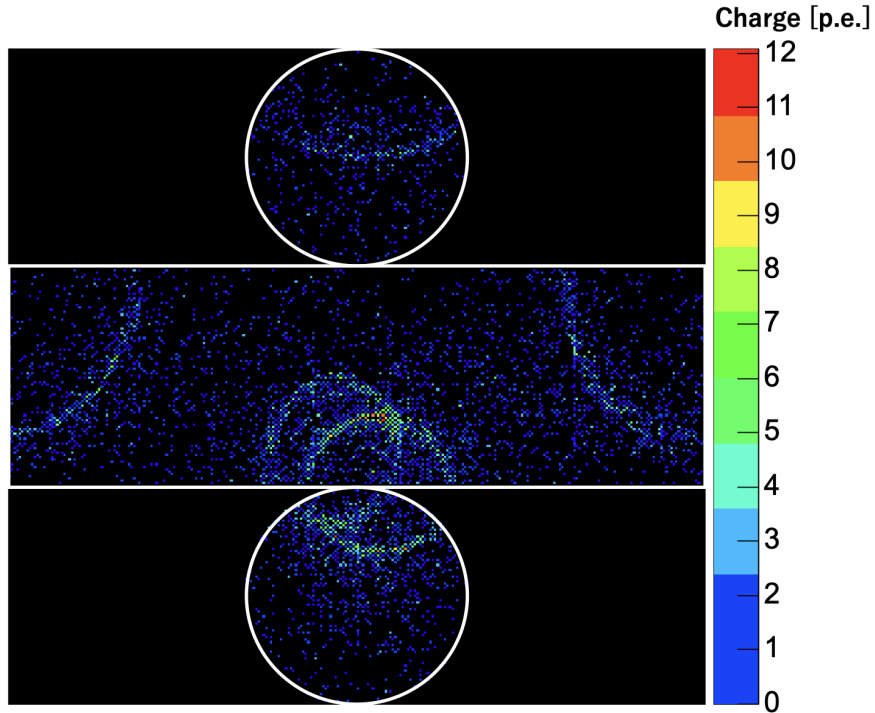


Figure 4.4. Event display of a  $p \rightarrow e^+\pi^0$  event.

## 4.2 Event Reconstruction with fitQun

When an event occurs in HK, the recorded information of detected charge and timing of each PMT is used to reconstruct the vertex, particle momentum, and particle type for that event. In this analysis, a reconstruction tool called “fitQun” is used. fitQun is a package for event reconstruction in water Cherenkov detectors and was initially developed for SK and T2K experiments based on the reconstruction method used in the MiniBooNE experiment [38]. The old reconstruction tool named “APfit” [39] was used in the previous analysis of  $p \rightarrow e^+\pi^0$  in SK, while fitQun was used for the mode of  $p \rightarrow \mu^+K^0$  in SK [40].

fitQun is a maximum likelihood fitter and the reconstruction is performed as following steps;

1. Vertex pre-fitter
2. Single-ring fitter
3. Multi-ring fitter

In this section, overviews of the likelihood function and each step of reconstruction are explained. The more detail information about fitQun is discussed in [41].

### 4.2.1 Likelihood

The strategy of fitQun is to search for the values of various variables to maximize the following likelihood function,

$$L(\mathbf{\Gamma}) = \prod_j^{\text{unhit}} P_j(\text{unhit}|\mu_j) \prod_i^{\text{hit}} \{1 - P_i(\text{unhit}|\mu_i)\} f_q(q_i|\mu_i) f_t(t_i|\mathbf{\Gamma}),$$

where  $\mu$  is predicted charge (explained in Sec.4.2.2) as a function of  $\mathbf{\Gamma}$ , and  $\mathbf{\Gamma}$  is a set of parameters including vertex position  $\mathbf{x} = (x, y, z)$ , time  $t$ , zenith angle  $\theta$ , azimuth angle  $\phi$ , and momentum  $p$ . In this equation, the index  $j$  runs over all PMTs which did not register a hit (“unhit” PMTs) and the index  $i$  runs over all PMTs which registered a hit (“hit” PMTs).  $P_j(\text{unhit}|\mu_j)$  is the probability that the PMT does not register a hit and  $1 - P_i(\text{unhit}|\mu_i)$  is the probability that the PMT registers a hit.  $f_q(q_i|\mu_i)$  and  $f_t(t_i|\mathbf{x})$  are the probability density functions of the observed charge and time, respectively.  $f_q(q_i|\mu_i)$  and  $f_t(t_i|\mathbf{x})$  are based on detector simulations of electron, muon, and pion events in HK with WCSim.

### 4.2.2 Predicted charge

When a single particle hypothesis with parameters  $\mathbf{\Gamma}$  is given, the predicted charge each PMT observes is estimated for the direct light ( $\mu^{\text{dir}}$ ), indirect light due to scattering with water ( $\mu^{\text{sct}}$ ), and charge due to dark count ( $\mu^{\text{dark}}$ ), separately. In the case of a multi-particle ( $n$  particles) hypothesis, the predicted charge is independently calculated for  $n$ -th particle hypothesis and summed for all particle hypotheses as follows.

$$\mu_i = \sum_n (\mu_{i,n}^{\text{dir}} + \mu_{i,n}^{\text{sct}}) + \mu^{\text{dark}} \quad (4.7)$$

In this analysis, the dark count rate is assumed to be 4.2 kHz, the same level as SKPMT.  $\mu^{\text{dark}}$  takes into account this value.  $\mu^{\text{dir}}$  and  $\mu^{\text{sct}}$  are given as below;

$$\mu^{\text{dir}} = \Phi(p) \int ds g(p, s, \cos \theta) \Omega(R) T(R) \epsilon(\eta) \quad (4.8)$$

and

$$\mu^{\text{sct}} = \Phi(p) \int ds \frac{1}{4\pi} \rho(p, s) \Omega(R) T(R) \epsilon(\eta) A(s), \quad (4.9)$$

where  $s$  is the distance the particle has traveled from the point where it began to emit Cherenkov light, and  $p$  is the momentum of the particle at the position where it started to emit Cherenkov light.  $R$ ,  $\theta$ , and  $\eta$  are variables to indicate the relative position between the PMT and the particle as shown in Fig. 4.5.

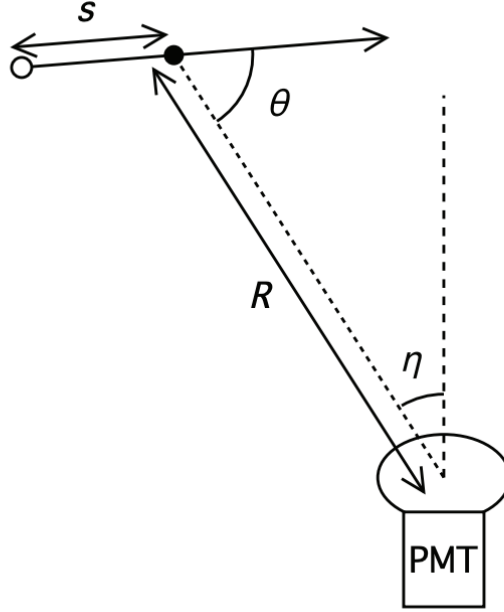


Figure 4.5. Schematic diagram illustrating the relationship between the variables for the predicted charge, with the particle's vertex position marked as a white dot. Taken from [41].

In Eq.4.8 and Eq.4.9,  $\Phi$  is the photon yield,  $g$  is the Cherenkov emission profile,  $\Omega$  is the PMT solid angle factor,  $T$  is the light transmission factor,  $\epsilon$  is the PMT angular acceptance,  $\rho$  is the photo emission fraction and  $A$  is the ratio of charge generated by direct light to that generate by indirect light.

fitQun used in this thesis is under development and does not take into account the scattering of Cherenkov photons in water.

### 4.2.3 Vertex pre-fitter

The vertex position of an event is determined by minimizing  $-\ln L(\mathbf{\Gamma})$ . To ensure that the  $-\ln L(\mathbf{\Gamma})$  converges, proper initial parameters are needed. The vertex pre-fitter roughly estimates the vertex position  $\mathbf{x}$  and time  $t$  using information of hit timing of each PMT in a time window of (-100 ns, +400 ns) around the event trigger.  $\mathbf{x}$  and  $t$  are estimated by maximizing the goodness function defined as below;

$$G(\mathbf{x}, t) = \sum_i^{\text{hit}} \exp(-(T_{res}^i/\sigma)^2/2), \quad (4.10)$$

where

$$T_{res}^i = t_i - t - |\mathbf{R}_{PMT}^i - \mathbf{x}|/(c/n). \quad (4.11)$$

$t_i$  and  $\mathbf{R}_{PMT}^i$  are hit time and position of the  $i$ -th PMT. When  $t$  and  $\mathbf{x}$  get close to the true time and position of the event,  $T_{res}^i$  get close to 0 and  $G(\mathbf{x}, t)$  becomes larger. The

pre-fitter first maximizes the goodness by performing a rough iterative grid search in time, shrinking the grid size and  $\sigma$ . After the grid search is done,  $-G(\mathbf{x}, t)$  is minimized with  $\sigma = 4$  ns and obtained values are given as the seeds of minimization of  $-\ln L(\mathbf{x})$ .

If there are multiple hit clusters by the secondary reactions such as Michel electrons from muon decay near one event trigger, they are counted as subevents as the following procedure. First, the goodness  $G(\mathbf{x}, t)$  discussed in Eq.4.10 is scanned from  $-200$  ns to  $15000$  ns around the event trigger, while varying the time  $t$  by fixing the  $\mathbf{x}$  the vertex pre-fitter provided. Figure 4.6 is an example of the distribution of goodness as a function of  $t$ . In this figure, the goodness has several peaks at different times.

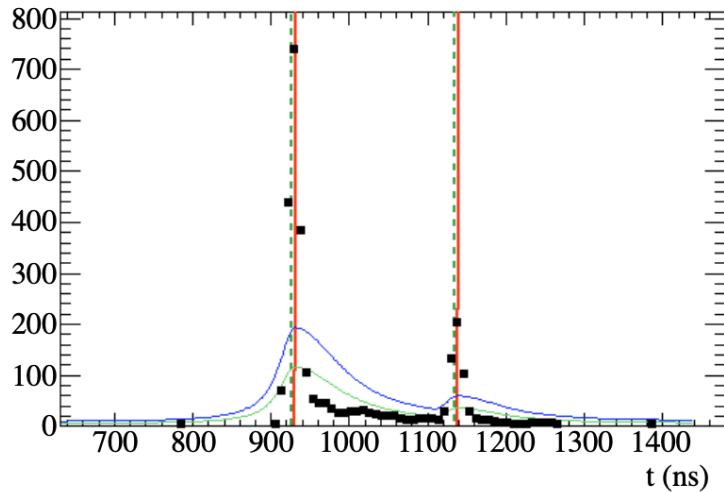


Figure 4.6. Distribution of goodness as a function of  $t$  for an event with a parent muon and a Michel electron. The vertical dashed lines indicate true particle time. The black dots are the scanned goodness points. The blue and green lines indicate the threshold which are used to search peaks. The red vertical lines indicate the time of the subevents found by the algorithm. Taken from [41].

After the peaks are searched, a time window of  $-180$  ns  $< T < 800$  ns is set around each peak, where  $T$  is the peak position. If the time windows for different peaks are overlapped, they are merged. In each time window,  $T_{res}^i$  is re-evaluated.

Finally, the vertex pre-fit and the peak search are conducted again. The final time windows are fixed for each remaining peak, and the maximum likelihood reconstruction is done in each of them.

#### 4.2.4 Single-ring fitter

After the vertex position and time of each subevent are roughly determined by the vertex pre-fitter, the single-ring fit is performed to determine the direction, momentum, vertex position and time of the particle for each subevent with single-ring hypothesis. The single-ring fitter considers the particle that gave rise to the ring to be an electron, a muon, or a charged pion.

First, single-ring electron fit is performed by minimizing the  $-\ln L$ . Second, single-ring muon fit is performed by using the value obtained in the single-ring electron fit as the seed. As for charged pion hypothesis, a charged pion can interact with nucleus of water hadronically and make two rings. A ring made before such interaction is defined as “upstream ring” and one after the interaction is defined as “downstream ring”. Therefore, single-ring charge pion fitter is performed considering both the upstream and downstream ring.

For the first subevent, the result of the single-ring fit above is used as the seed of the multi-ring fitter explained in Sec.4.2.5 and the particle type is identified by the multi-ring fitter. For the subsequent subevents, the particle identification (PID) is done based on the result of the single-ring fit because the multi-ring fitter is performed only for the first subevent. However, the parameters for the PID for those subsequent subevents have not tuned yet for HK. In this thesis, only the first subevent is used for analysis, so this incompleteness is not a problem.

### 4.2.5 Multi-ring fitter

fitQun also deals with multi-particle events by the multi-ring fitter for the first subevent. The multi-ring fitter searches up to 6-rings. Subsequent subevents are not considered as multi-particle events because they usually do not contain multi-particles.

The ring counting procedure is shown in Fig. 4.7.

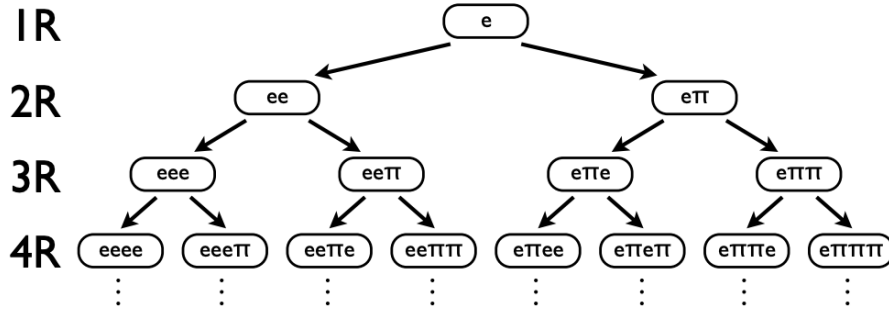


Figure 4.7. Tree diagram illustrating the ring counting algorithm. In this figure, the process starts from single electron ring hypothesis. Taken from [41].

The multi-ring fitter uses the results of the single-ring fitter as a starting point as mentioned in Sec.4.2.4. In addition, all rings are once fitted as either electrons or pions. The muon hypothesis is only considered at the end of the sequence of steps. The basic flow is,

1. Add one ring to the current number of rings ( $n$ -ring hypothesis) and perform fitting as  $(n + 1)$ -ring hypothesis. As the additional ring, both electron and  $\pi^+$  are tested.
2. Compare the likelihood  $L_{nR}$  of  $n$ -ring hypothesis and the likelihood  $L_{(n+1)R}$  of  $n + 1$ -ring hypothesis, and determine whether the added ring is a true ring or a fake using the following criteria.

- $\ln(L_{2R}/L_{1R}) > 180$  (when  $n = 1$  and the added second ring is electron.)
- $\ln(L_{2R}/L_{1R}) > 117$  (when  $n = 1$  and the added second ring is  $\pi^+$ .)
- $\ln(L_{(n+1)R}/L_{nR}) > 105$  (when  $n > 1$ .)

These cut values (180, 117, and 105) are tuned for HK using MC.

3. If the  $L_{(n+1)R}$  meets the criteria above, the added ring is judged to be true. If so, the ring is accepted and the process is repeated from 1 to 3. If the ring is judged to be fake, the ring is rejected and the process stops at the  $n$ -ring hypothesis.

Figure 4.7 shows only the case where the first ring is  $e$ -like, but same procedure is performed for the case where the first ring is  $\pi^+$ -like. After all the branches of the multi-ring hypothesis tree are terminated, the hypothesis with the smallest  $-\ln L$  is chosen as the seed hypothesis and the others are rejected. For the seed hypothesis, if there are two rings with an angle of less than 20 degree between them, they are combined into a single ring with the total energy of the two rings. After this ring merging, first, the most energetic ring is refitted with both electron and  $\pi^+$  hypotheses while the other rings are fixed. If the following criterion is met for the ring, it is identified as  $e$ -like and the original hypothesis is replaced.

$$\ln(L_e/L_{\pi^+}) > -10 \quad (4.12)$$

If not, the ring is identified as  $\pi^+$ -like. These re-fitting and re-identified process as above are performed for all the remaining rings in the descending order of the visible energy.

As mentioned earlier, in the multi-ring fitter, only  $e/\pi^+$  separation is considered until the number of ring and the type of each ring ( $e$ -like or  $\pi^+$ -like) are determined in the procedure above. However, in case the ring is judged as  $\pi^+$ -like and it is the most energetic ring, the ring is always considered as a muon, while it is always considered as  $\pi^+$  if it is a lower energy ring.

#### 4.2.6 Dependence of fiTQun performance on distance from wall

When the true vertex position is near the wall of the detector, the number of PMTs that receive Cherenkov light may be small compared with that when the vertex is far from the wall. Since fiTQun uses the information of PMTs for reconstruction, such a small number of hits makes it difficult to reconstruct the event accurately. Therefore, the performance of fiTQun depends on the distance between the vertex position and the wall. Here, the dependence of the momentum resolution and the performance of the particle identification (PID) on the distance from the vertex position to the nearest wall are discussed using samples of electrons and muons with a kinetic energy of 500 MeV.

The momentum resolution is defined as the ratio of the sigma of the Gaussian fitted to the distribution of the reconstructed momentum to the true momentum (see Fig. 4.8). Figure 4.9 shows the momentum resolution plotted as a function of the distance from the true vertex points to the nearest wall for electrons and muons. From Fig. 4.9, the momentum resolution becomes worse as the vertex position gets closer to the wall. In particular, in the region of the distance below 100 ~ 200 cm, the resolution is clearly worse than in the other region.

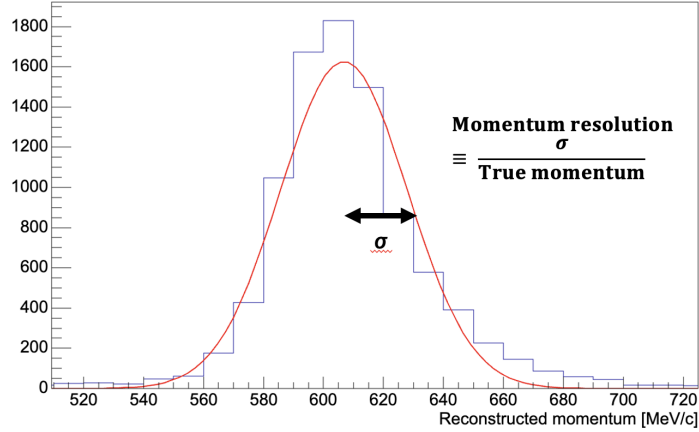


Figure 4.8. Definition of the momentum resolution. The blue histograms shows a distribution of reconstructed momentum. The red line shows a Gaussian fitted to the histogram. The momentum resolution is defined as the ratio of the sigma of the Gaussian to the true momentum.

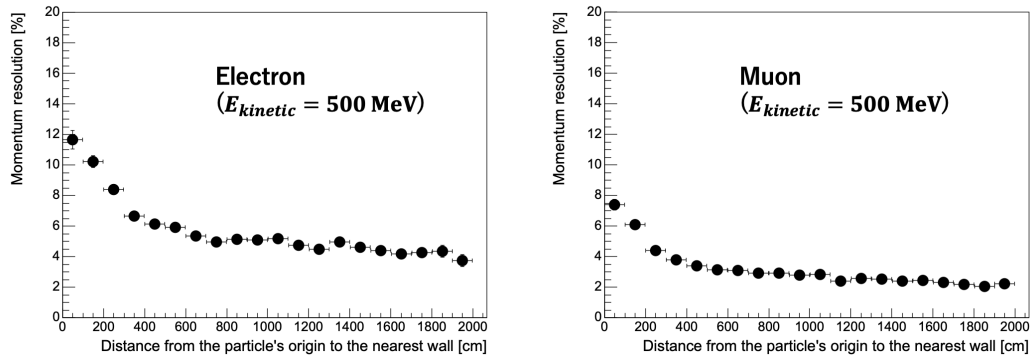


Figure 4.9. Momentum resolution plotted as a function of the distance from the true vertex points to the nearest wall for electrons (left) and muons (right).

As mentioned in Sec.4.2.5, PID is performed using  $\ln(L_e/L_{\pi^+})$ . Figure 4.10 shows the distributions of  $\ln(L_e/L_{\pi^+})$  for electrons and muons in the region where the distance from the nearest wall is greater than 200 cm. In Figure 4.10, electrons and muons are well separated.

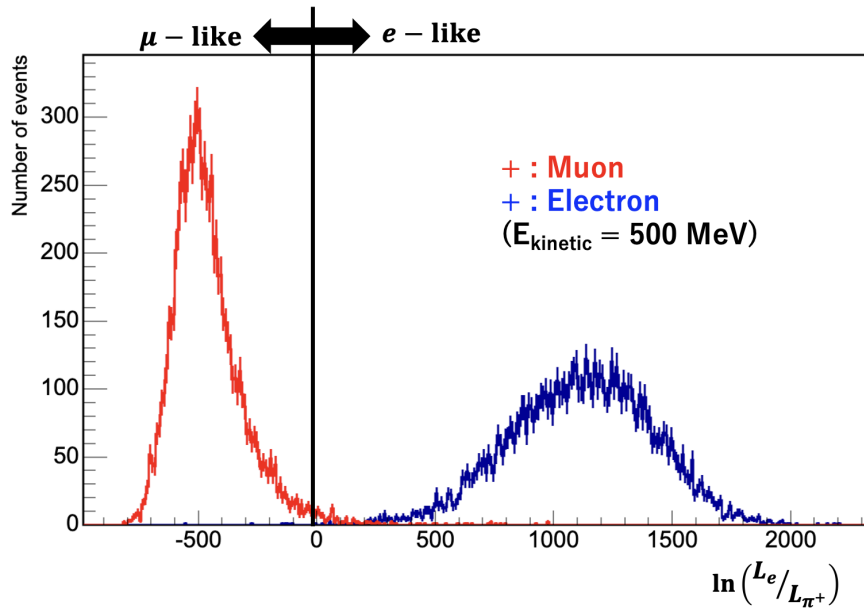


Figure 4.10. The distributions of  $\ln(L_e/L_{\pi^+})$  for electrons and muons in the region where the distance from the nearest wall is greater than 200 cm.

Figure 4.11 shows the accuracy of the PID as a function of the distance from the true vertex position to the nearest wall for electrons and muons. From Fig. 4.11, the PID accuracy also becomes worse as the vertex position gets closer to the wall. In particular, the PID accuracy for muons is clearly worse in the region of the distance below 100 ~ 200 cm.

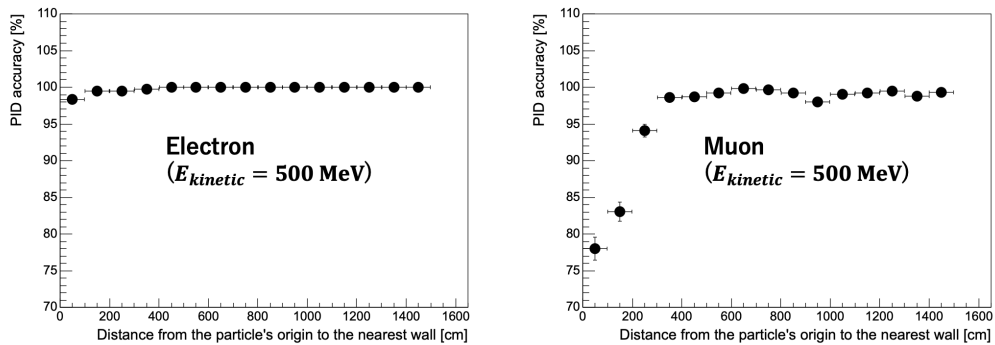


Figure 4.11. PID accuracy plotted as a function of the distance from the true vertex position to the nearest wall for electrons (left) and muons (right).

In addition to the above, when cosmic muons come from the outside of the detector, their vertex position will be reconstructed near the wall surface. From these reasons, the region near the wall should not be used for the analysis. The official fiducial volume of HK is defined as the region where the distance from the nearest wall is greater than 150

cm. With this definition, the fiducial volume of HK is 188 kt. In SK, fitQun was actually tuned so that the performance remains consistent up to a distance of 150 cm from the nearest wall [15]. However, considering the imperfections in tuning of fitQun and the fact that the veto against cosmic ray muons is still undeveloped and it is unclear how well it will perform, the fiducial volume of HK in this thesis is conservatively defined as the region where the distance from the nearest wall is greater than 200 cm. With this definition, the fiducial volume of HK is 183.3 kt and 5 kt smaller than the official value. Whether the fiducial volume can actually be extended up to a region of 150 cm from the nearest wall is a future task.

## 4.3 Proton decay analysis

### 4.3.1 Event selection

In this analysis, the signal of  $p \rightarrow e^+\pi^0$  is selected by the criteria as below :

1. The reconstructed vertex is inside the fiducial volume
2. The number of reconstructed rings is two or three
3. All rings should be identified as  $e$ -like
4. No Michel electron
5.  $85 \text{ MeV}/c^2 < \text{invariant mass of two gamma rays} < 185 \text{ MeV}/c^2$  for 3-ring events
6.  $800 \text{ MeV}/c^2 < \text{total invariant mass} < 1050 \text{ MeV}/c^2$
7. Total momentum  $< 250 \text{ MeV}/c$

To compare this analysis and the analysis in SK, these criteria are the same as those used in the latest analysis in SK [12]. However, an additional criterion that the number of tagged neutron is zero is imposed after the criterion 7 in SK because almost no neutrons appear in  $p \rightarrow e^+\pi^0$ . This criterion for tagged neutrons reduced the backgrounds by half while reducing the signal efficiency very little in SK [12]. However, this criterion is not used here because neutron tagging algorithm is not applied in this analysis due to the old electronics scheme implemented in WCSim as mentioned in Sec.4.1.3. The criterion 1 to 7 mentioned above are discussed below using 50000 signal events and 0.917 Mt·year worth (corresponding to 5 years operation in HK) atmospheric MC.

For the criterion 1, the distance from the wall to the reconstructed vertex is called “dwall”. As discussed in Sec.4.2.6, the fiducial volume of HK is defined as the region where the distance from the nearest wall is greater than 2 m in this thesis. Therefore, only events with  $d_{\text{wall}} > 200 \text{ cm}$  are selected.

For the criterion 2, in the mode of  $p \rightarrow e^+\pi^0$ , a positron and a neutral pion are emitted back-to-back from a proton at the rest frame of the proton. The neutral pion decays immediately into two gamma rays because life time of a neutral pion is about  $10^{-16} \text{ s}$ . Those two gamma rays create two  $e$ -like rings by the electromagnetic shower process. However, those two gamma rays cannot be reconstructed correctly when one of them has

very low momentum due to the Lorentz-boost. Moreover, when there is overlap between three rings, some of the rings may not be able to be reconstructed correctly. Taking into account such effects, the 2- or 3-ring events are selected by the criterion 2. As for atmospheric neutrino events, most single electron or muon events from the CCQE interaction are rejected with this criterion. Figure 4.12 shows the distribution of the number of rings in the signal and atmospheric neutrino MC after applying the criterion 1. About 30 % of signal events are counted as 1-ring due to the absorption of  $\pi^0$  in the nucleus.

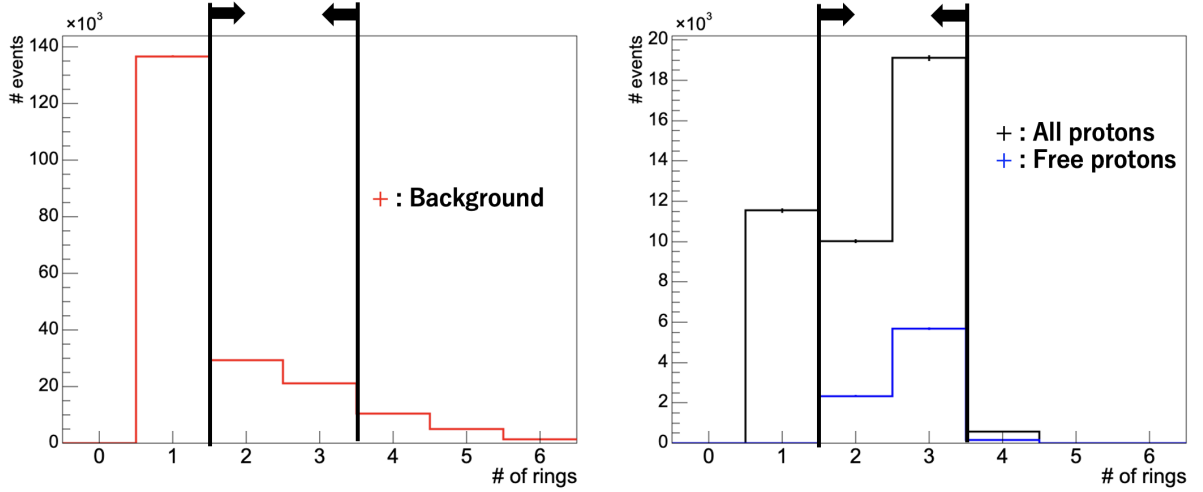


Figure 4.12. The distribution of the number of rings in the signal (right) and atmospheric neutrino (left) MC after applying the criterion 1. In the right plot, the black histogram is for all protons and the blue one is for free protons. The black vertical lines and arrow symbols show the selected region for the criterion 2.

For the criterion 3, in  $p \rightarrow e^+\pi^0$ , visible particles are one electron and two  $\gamma$ s except when a charged pion is produced by charge exchange in the nucleus. Since both an electron and a gamma generate  $e$ -like ring, the criterion 3 requires that all rings are  $e$ -like. As for backgrounds, many of events such as primary neutrinos are  $\nu_\mu$  ( $\bar{\nu}_\mu$ ) are removed. About 60-70 % of backgrounds can be rejected with this criterion because the ratio of electron neutrinos to muon neutrinos in atmospheric neutrinos is 1:2 when ignoring the neutrino oscillations. Atmospheric neutrino events where charged pions or secondary muons are generated are also rejected. Figure 4.13 shows the distribution of all  $e$ -like or not in the signal and atmospheric neutrino MC after applying the criterion 1 and 2.

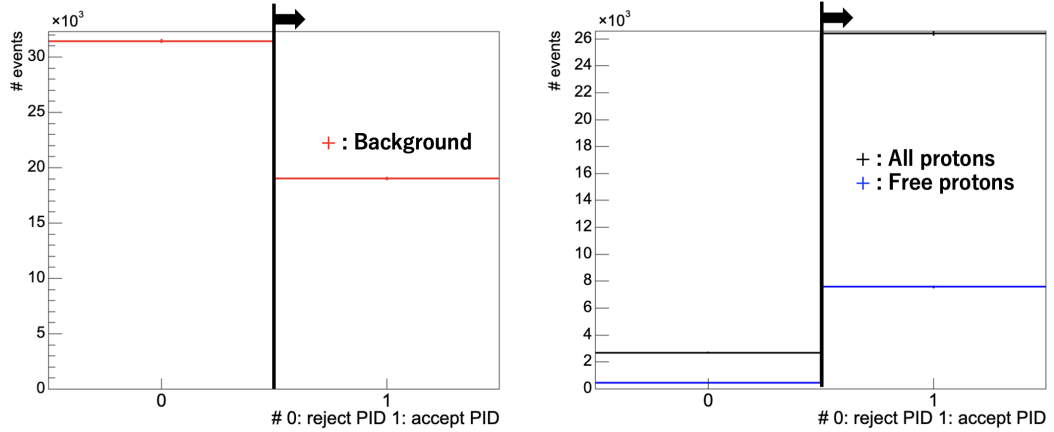


Figure 4.13. The distribution of all  $e$ -like or not in the signal (right) and atmospheric neutrino (left) MC after applying the criterion 1 and 2. In each histogram, 1 of the horizontal axis means all  $e$ -like (accepted) and 0 means the other (rejected). In the right plot, the black is for all protons and the blue is for free protons. The black vertical lines and arrow symbols show the selected region for the criterion 3.

For the criterion 4, in  $p \rightarrow e^+\pi^0$ , no muons appear except when a charged pion is produced by charge exchange in the nucleus. Therefore, the criterion 4 requires that the number of Michel electrons is zero. Though the criterion 3 also removes events containing  $\mu$ -like particles, this selection can reject atmospheric neutrino events where muons which have lower momentum than the Cherenkov threshold or long life mesons are generated. Figure 4.14 shows the distribution of the number of Michel electrons in the signal and atmospheric neutrino MC after applying the criterion 1-3.

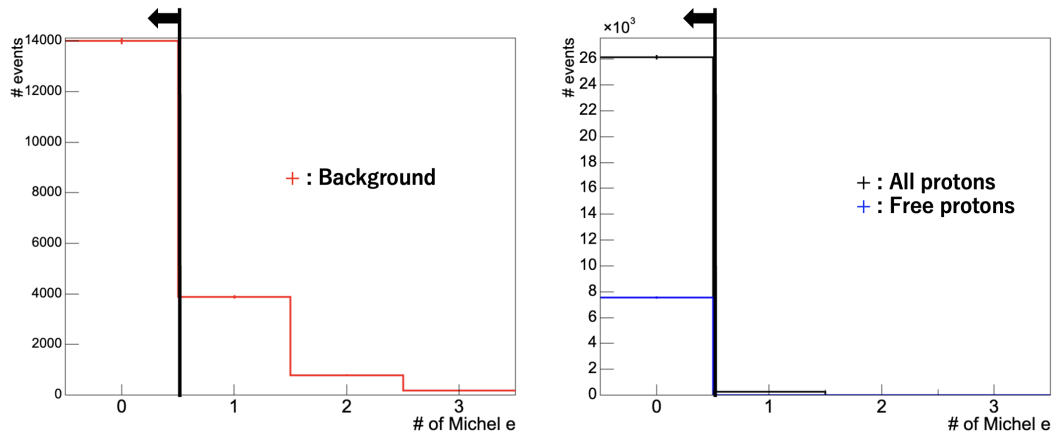


Figure 4.14. The distribution of the number of Michel electrons in the signal (right) and atmospheric neutrino (left) MC after applying the criterion 1-3. In the right plot, the black histogram is for all protons and the blue one is for free protons. The black vertical lines and arrow symbols show the selected region for the criterion 4.

For the criterion 5, when the number of rings is determined to be three in the criterion 2, the invariant mass of  $\pi^0$  ( $M_{\pi_0}$ ) can be reconstructed because both of the two gamma rays from  $\pi^0$  are reconstructed. In this analysis, two of the three rings are chosen and the invariant mass is calculated in each combination. The one closest to  $135 \text{ MeV}/c^2$  is chosen as  $M_{\pi_0}$ . Figure 4.15 shows the distribution of the reconstructed  $\pi^0$  mass in the signal and atmospheric neutrino MC after applying the criterion 1-4.

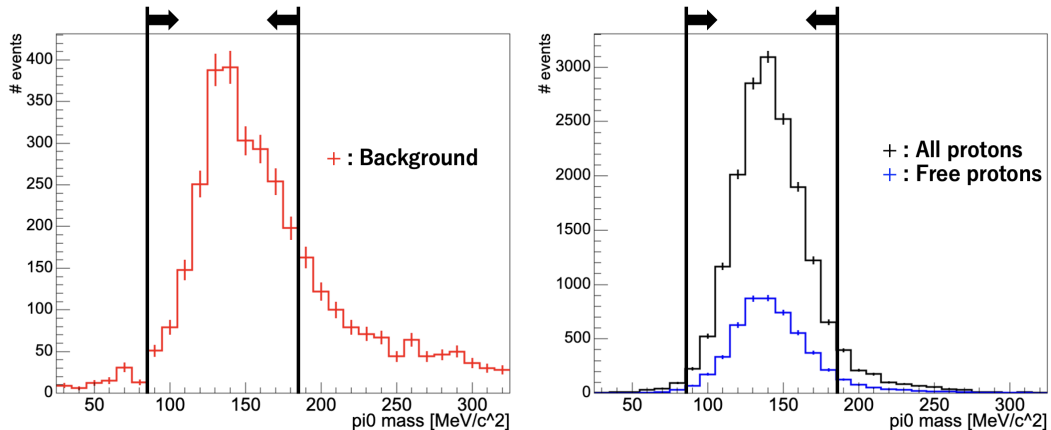


Figure 4.15. The distribution of  $M_{\pi_0}$  in the signal (right) and atmospheric neutrino (left) MC after applying the criterion 1-4. In the right plot, the black histogram shows the all protons and the blue one shows the free protons. The black vertical lines and arrow symbols show the selected region for the criterion 5.

In the distribution for signal events, there is a clear peak around  $135 \text{ MeV}/c^2$ . Thus, events satisfying  $85 \text{ MeV}/c^2 < M_{\pi_0} < 185 \text{ MeV}/c^2$  are selected. In the distribution for the atmospheric neutrino events, there is also a peak around  $135 \text{ MeV}/c^2$  because many events with three  $e$ -like rings include a  $\pi^0$  such as  $\text{CC}1\pi^0$  events. However, some other mesons such as  $\eta$  also have a decay mode with two  $\gamma$ s and those events are removed.

For the criterion 6, the invariant proton mass  $M_{tot}$  can be calculated from the observed momentum and energy of all of the two or three rings. Figure 4.16 shows the distribution of  $M_{tot}$  in the signal and background events after applying the criterion 1-5. In the distribution of signal events, especially for free protons, there is a clear peak of the distribution in signal events is around true proton mass ( $938 \text{ MeV}/c^2$ ). Thus, events satisfying  $800 \text{ MeV}/c^2 < M_{\pi_0} < 1050 \text{ MeV}/c^2$  are selected. On the other hand, the number of background events is small in the region of  $800 \text{ MeV}/c^2 < M_{tot} < 1050 \text{ MeV}/c^2$ .

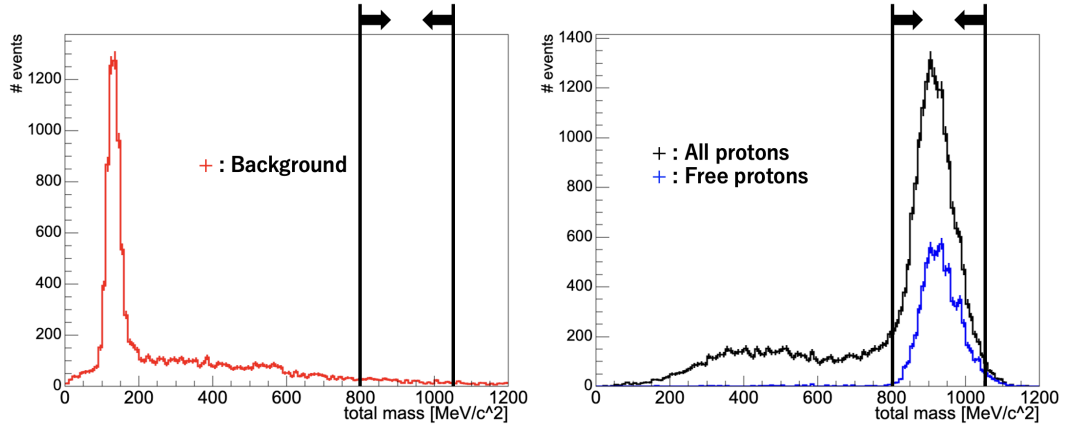


Figure 4.16. The distribution of reconstructed proton mass in the signal (right) and atmospheric neutrino MC (left) events after applying the criterion 1-5. In the right plot, the black histogram shows the all protons and the blue one shows the free protons. The black vertical lines and arrow symbols show the selected region for the criterion 6.

For the criterion 7, the total momentum  $P_{tot}$  is the sum of the observed momentum of all of the 2 or 3 rings. Figure 4.17 shows the distribution of  $P_{tot}$  in the signal and atmospheric MC after applying the criterion 1-6. From Fig. 4.17, it can be seen that many signal events exist in the region of  $P_{tot} < 250$  MeV/c, especially for free protons. Thus, events satisfied  $P_{tot} < 250$  MeV/c are selected. This selection is very effective to reject backgrounds because most particles generated by atmospheric neutrinos are emitted to the forward region.

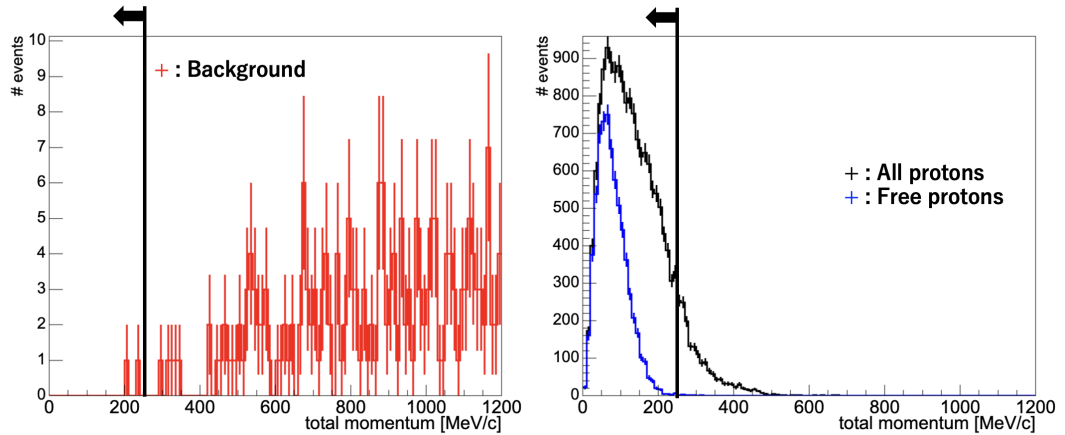


Figure 4.17. The distribution of total momentum in the signal (right) and atmospheric neutrino(left) MC after applying the criterion 1-5. In the right plot, the black histogram shows the all protons and the blue one shows the free protons. The black vertical lines and arrow symbols show the selected region for the criterion 7.

The breakdown of the signal efficiency and the number of the remaining atmospheric neutrino MC after applying each selection criterion are shown in Fig. 4.18 and Table 4.2.

The signal efficiency is defined as the ratio of remaining signal events after applying each criterion to the total number of signal events true vertices of which are inside the fiducial volume ( $d_{\text{wall}} > 200$  cm). The atmospheric MC is 0.917 Mt·year worth (corresponding to 5 years operation in HK). The breakdown in the latest analysis in SK is also shown in Figure 4.19 [12].

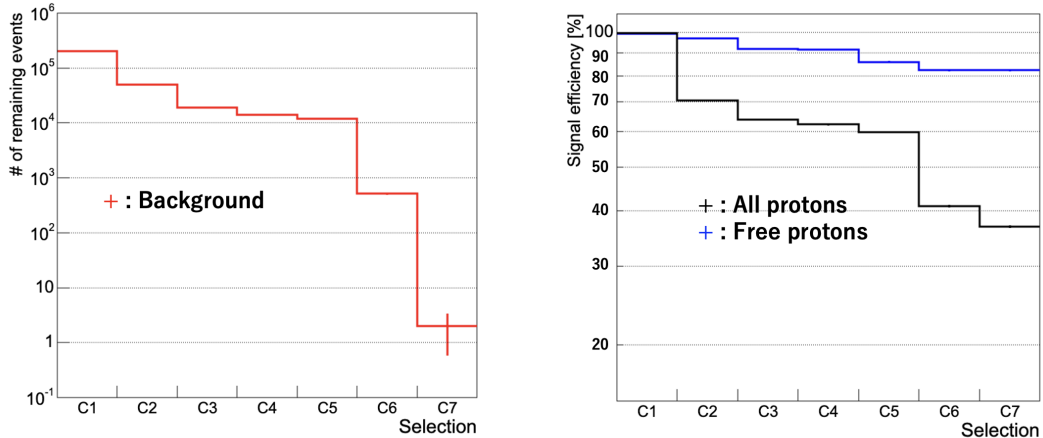


Figure 4.18. Signal efficiency (right) and remaining 5 years atmospheric neutrino MC (left) after applying each criterion. C1 to C7 in the horizontal axis correspond to the criterion 1 to 7, respectively.

Table 4.2. Signal efficiency and remaining 5 years atmospheric neutrino MC after applying each criterion.

Selection	Signal efficiency [%] (all protons)	Signal efficiency [%] (free protons)	Remaining backgrounds [events]
FV	$99.73 \pm 0.03$	$99.26 \pm 0.09$	$203968 \pm 452$
2- or 3-ring	$70.41 \pm 0.22$	$97.06 \pm 0.19$	$50465 \pm 225$
$e$ -like	$63.87 \pm 0.23$	$91.71 \pm 0.30$	$19020 \pm 138$
No Michel $e$	$63.26 \pm 0.24$	$91.50 \pm 0.31$	$13998 \pm 118$
$\pi^0$ mass	$59.84 \pm 0.24$	$85.96 \pm 0.38$	$12014 \pm 110$
Total mass	$40.91 \pm 0.24$	$82.37 \pm 0.42$	$514 \pm 23$
Total momentum	$36.76 \pm 0.24$	$82.26 \pm 0.42$	$2 \pm 1.4$

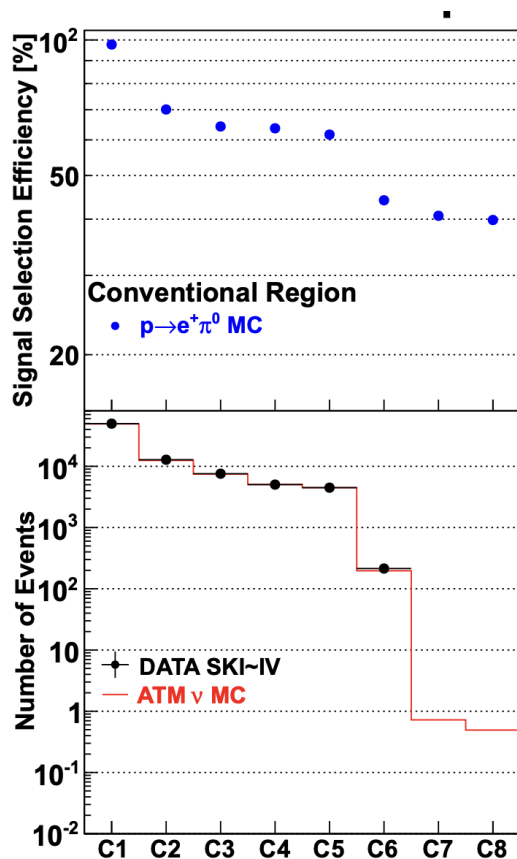


Figure 4.19. The breakdown of the signal efficiency and remaining backgrounds in the latest analysis in SK. C1-7 correspond to the criterion 1 to 7. C8 is ignored because it is the criterion for number of tagged neutrons and not applied in this analysis. Taken from [12].

Table 4.3 is the summary of the signal efficiency after applying all criteria and the background rate. The background rate is calculated as the number of remaining atmospheric neutrino events per Mt·year after applying all criteria, assuming that the fiducial volume is 183.31 kt.

Table 4.3. Signal efficiency after applying all criteria and background rate

Signal efficiency (all protons)	$36.76 \pm 0.24 \%$
Signal efficiency (free protons)	$82.26 \pm 0.42 \%$
Background rate	$2.2 \pm 1.5 \text{ events}/(\text{Mt}\cdot\text{year})$

In the latest analysis of  $p \rightarrow e^+\pi^0$  in SK, the signal efficiency with the same criteria as this analysis is approximately 42 % for all protons. Therefore, the signal efficiency obtained in this analysis is about 5 % worse than in SK. Comparing Table 4.2 and Fig. 4.19, while the efficiencies at the criterion 1-4 (until the criterion for the Michel electrons) are similar between this analysis and the SK one, the efficiencies at the criterion 5-7 (the criterion for masses and momenta) in this analysis are lower than in SK. This is

due to worse resolution of fiTQun used in this analysis. For example, in this analysis, the Gaussian fitted  $\pi^0$  mass peak and sigma are  $141.0 \pm 0.2$  MeV/ $c^2$  and  $23.5 \pm 0.2$  MeV/ $c^2$  respectively for all protons (the distribution of reconstructed  $\pi^0$  mass is shown in Fig. 4.15). On the other hand, the  $\pi^0$  mass peak and sigma are  $135.0$  MeV/ $c^2$  and  $17.4$  MeV/ $c^2$  respectively in SK [12]. Therefore, the sigma of reconstructed  $\pi^0$  mass in this analysis is about 30 % larger than that in SK analysis. It is speculated that this worse resolution is due to the fact that the tuning of fiTQun is incomplete at this time. For example, fiTQun used in this analysis does not take into account scattering of Cherenkov light in water as mentioned in Sec.4.2.2. Therefore, the signal efficiency can be improved if fiTQun is sufficiently tuned in the future.

In the 11.25 Mt-year worth atmospheric neutrino MC study in the latest SK analysis, the background rate is 1.83 events/(Mt-year) [12] and it is consistent with the value in this analysis,  $2.2 \pm 1.5$  events/(Mt-year). However, the MC used in this analysis is only 0.917 Mt-year worth (corresponding to 5 years operation in HK) and it is not a sufficient statistic. To increase statistics of backgrounds, additional atmospheric MC was generated. The energies of primary neutrinos of the 0.917 Mt-year worth background MC remaining after applying the criterion 6 (total mass cut) are distributed within 1 GeV to 100 GeV (see Fig. 4.20). Also, most backgrounds for the  $p \rightarrow e^+\pi^0$  analysis have a parent neutrino energy from 1 GeV to 10 GeV in the previous analysis in SK (see Fig. 4.21). In fiTQun, the time required for event reconstruction increases as the number of rings increases (sometimes taking more than 10 minutes per event). Therefore, high-energy events with a large number of generated particles take longer to reconstruct. On the other hand, low-energy events below 1 GeV take less time to reconstruct, but the number of events is large in such a low energy region. From these reasons, to save time, the energy of a primary neutrinos of the additional atmospheric MC is restricted from 0.8 GeV to 100 GeV. As a result of this restriction, the time required to generate and reconstruct the atmospheric neutrino MC for the same number of years has been reduced to less than half.

The additional atmospheric MC is 9.51 Mt-years worth (51.9 years operation in HK) and the number of remaining events after applying all the selection criteria is 15. Therefore, the background rate becomes  $1.62 \pm 0.40$  events/(Mt-year) by merging the 5 years MC with the full energy region and the 51.9 years MC with the energy region from 0.8 GeV to 100 GeV. This value is also consistent with that in the previous analysis in SK.

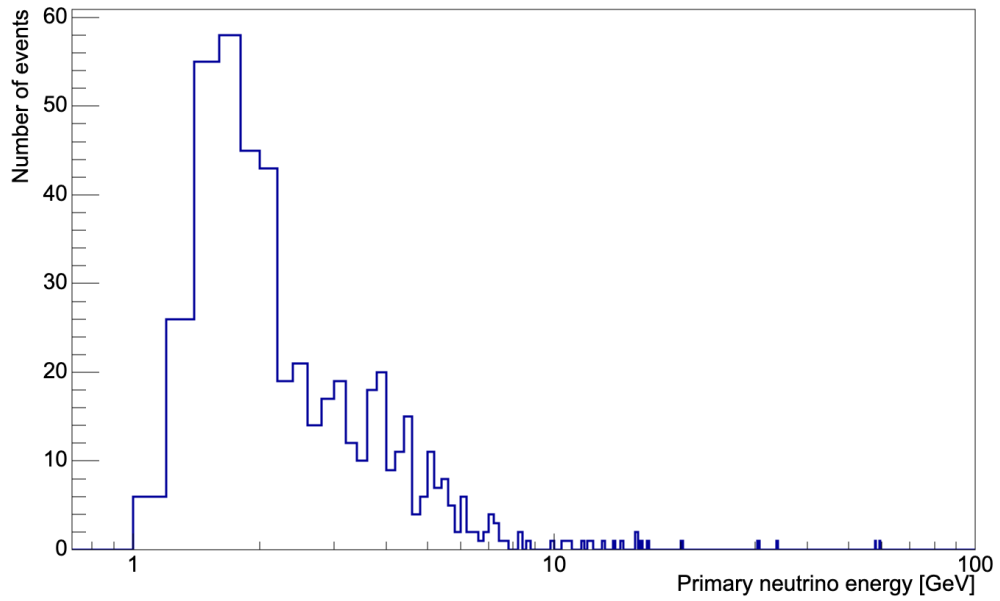


Figure 4.20. Primary neutrino energy distributions of the remaining 5 years atmospheric neutrino MC after applying the criterion 6 (total mass cut).

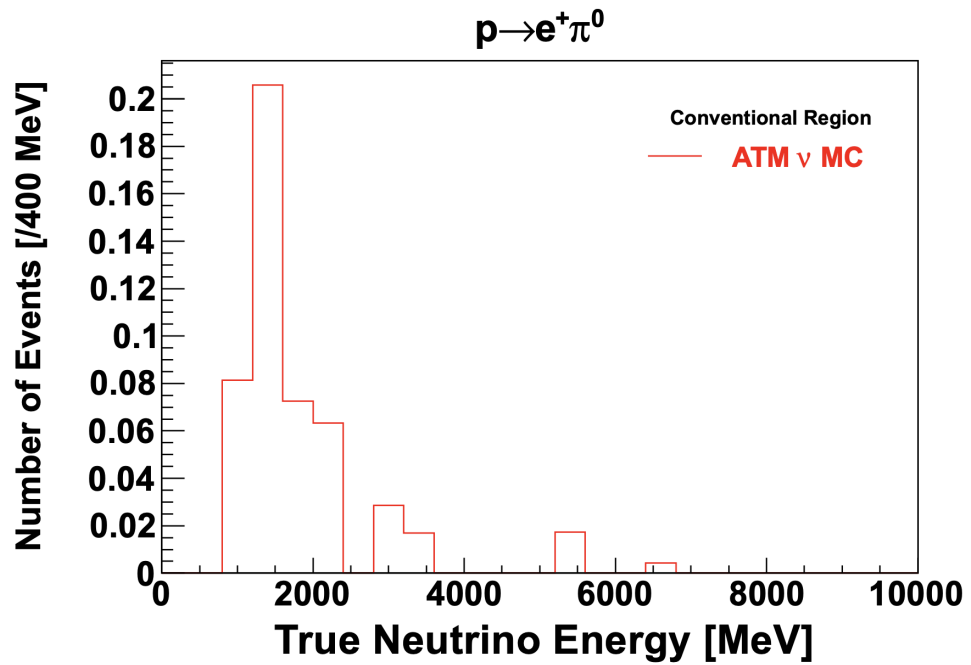


Figure 4.21. Primary neutrino energy distributions of the remaining atmospheric neutrino MC after applying all the criteria in SK. Taken from [12].

## Two box analysis

To improve the sensitivity by taking advantage of the characteristic of water having free protons, the remaining events in the region of the total momentum  $< 250 \text{ MeV}/c$  is further divided into two regions; a lower momentum region ( $P_{tot} < 100 \text{ MeV}/c$ ) and a higher momentum region ( $100 \text{ MeV}/c < P_{tot} < 250 \text{ MeV}/c$ ). In the lower momentum region, free proton decay events is concentrated while almost no atmospheric neutrino background events exist. On the other hand, in the higher momentum region, bound proton decay events are dominant while larger contamination from neutrino events can be seen. In the lower momentum region, a nearly background-free search can be performed. Therefore, we can achieve higher sensitivity by analyzing these two signal boxes separately. This method was used in the latest search for  $p \rightarrow e^+\pi^0$  in SK [12]. Table 4.4 is the summary of the signal efficiencies and background rates in the lower and higher momentum regions. Figure 4.22 shows the total mass ( $M_{tot}$ ) and momentum ( $P_{tot}$ ) scatter plots for the 5+51.9 year atmospheric neutrino MC and for the signal MC after applying the criteria 1 to 5. From Fig. 4.22, it can be seen that in the lower momentum region, many free proton events remain, whereas atmospheric neutrino events are extremely rare.

Table 4.4. Signal efficiencies and background rates in the lower and higher momentum regions

	Signal efficiency [%]	Background rate [/(Mt·yr)]
Lower momentum	$15.48 \pm 0.18$	$0.38 \pm 0.19$
Higher momentum	$21.28 \pm 0.20$	$1.25 \pm 0.35$

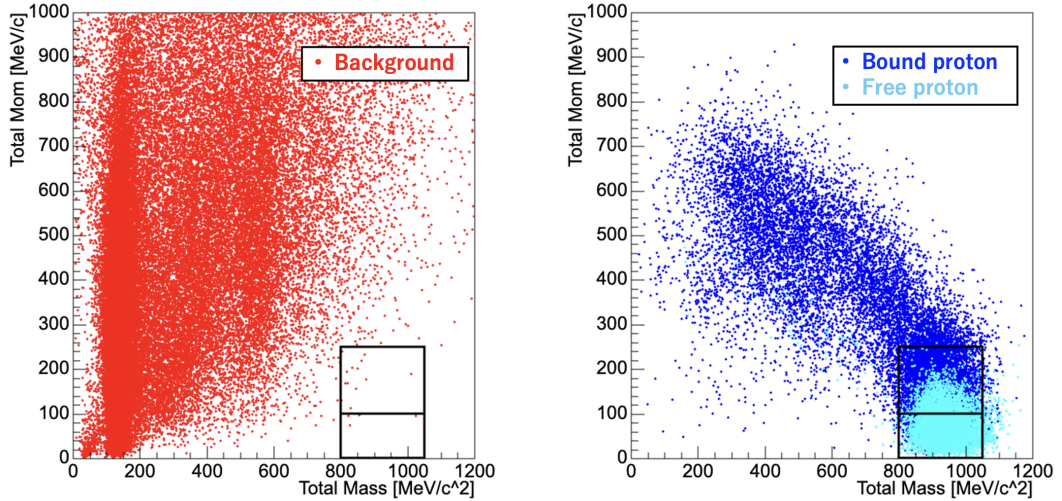


Figure 4.22. Total mass ( $M_{tot}$ ) and momentum ( $P_{tot}$ ) scatter plots for the 5+51.9 years atmospheric neutrino MC (left) and for the signal MC (right) after applying the criteria 1 to 5. For the right figure, the light (dark) blue shows free (bound) proton decay events. The two boxes in both figures correspond to the  $P_{tot} < 100 \text{ MeV}/c$  (lower momentum) region and the  $100 < P_{tot} < 250 \text{ MeV}/c$  (higher momentum) region.

### 4.3.2 Sensitivity

Here, the search sensitivity (expected lifetime limit at 90 % confidence level (CL)) to the mode of  $p \rightarrow e^+\pi^0$  in HK is discussed. The search sensitivity is calculated as follows;

$$\Gamma_{\text{exp}} = \sum_{n_0=0}^{\infty} \sum_{n_1=0}^{\infty} \frac{e^{-b_0} b_0^{n_0}}{n_0!} \frac{e^{-b_1} b_1^{n_1}}{n_1!} \Gamma_{90\%CL}(n_0, n_1, b_0, b_1), \quad (4.13)$$

$$\tau_{\text{exp}}/B = \frac{1}{\Gamma_{\text{exp}}} \quad (4.14)$$

where  $\Gamma_{\text{exp}}$  is the expected decay rate, the subscripts 0 and 1 represent the lower-momentum and higher-momentum regions respectively,  $b_i$  is the expected number of background events in each momentum region,  $n_i$  is the number of candidate events in each momentum region, and  $B$  is the branching ratio of a particular decay mode.  $\Gamma_{90\%CL}(n_0, n_1, b_0, b_1)$  is an upper limit of the decay rate with a candidate of  $(n_0, n_1)$  and a background of  $(b_0, b_1)$  at 90 % CL.  $\Gamma_{90\%CL}$  is derived by the following procedure.

The probability of detecting  $n_i$  events is given by a Poisson statistics as below if the decay rate  $\Gamma$ , the exposure  $\lambda_i$ , the signal efficiency  $\epsilon_i$ , and the number of background  $b_i$  are known ( $i = 0$  and  $i = 1$  correspond to the lower and higher momentum region, respectively);

$$P(n_i|\Gamma\lambda_i\epsilon_i b_i) = \frac{e^{-(\Gamma\lambda_i\epsilon_i+b_i)}(\Gamma\lambda_i\epsilon_i + b_i)^{n_i}}{n_i!}. \quad (4.15)$$

Applying Bayes' theorem to this probability, the following formulas are obtained;

$$P(\Gamma\lambda_i\epsilon_i b_i|n_i)P(n_i) = P(n_i|\Gamma\lambda_i\epsilon_i b_i)P(\Gamma\lambda_i\epsilon_i b_i). \quad (4.16)$$

Here, the decay rate, the exposure, the signal efficiency, and the number of background are assumed to be independent. With this assumption, Eq.4.16 is transformed as below;

$$P(\Gamma\lambda_i\epsilon_i b_i|n_i)P(n_i) = P(n_i|\Gamma\lambda_i\epsilon_i b_i)P(\Gamma)P(\lambda_i)P(\epsilon_i)P(b_i). \quad (4.17)$$

Then, the probability density function of the decay rate is given as follows;

$$P(\Gamma|n_i) = \frac{1}{A} \iiint \frac{e^{-(\Gamma\lambda_i\epsilon_i+b_i)}(\Gamma\lambda_i\epsilon_i + b_i)^{n_i}}{n_i!} P(\Gamma)P(\lambda_i)P(\epsilon_i)P(b_i) d\epsilon_i db_i d\lambda_i, \quad (4.18)$$

where  $A$  is defined as;

$$A = \int P(\Gamma|n_i) d\Gamma \quad (4.19)$$

The probability of the decay rate is assumed to be uniform;

$$P(\Gamma) = \text{const.} \quad (4.20)$$

The probabilities  $P(\lambda_i)$  and  $P(\epsilon_i)$  are defined as a Gaussian;

$$P(\lambda_i) \propto e^{-(\lambda_i - \lambda_{i0})^2 / 2\sigma_{\lambda_i}^2}, \quad (4.21)$$

$$P(\epsilon_i) \propto e^{-(\epsilon_i - \epsilon_{i0})^2 / 2\sigma_{\epsilon_i}^2}. \quad (4.22)$$

where  $\lambda_{i0}$  ( $\sigma_{\lambda_i}$ ) and  $\epsilon_{i0}$  ( $\sigma_{\epsilon_i}$ ) are the estimations (systematic errors) of the signal efficiency and the exposure, respectively. The statistical uncertainty of the estimation of the background events cannot be considered as the sigma of a Gaussian because the number of the remaining atmospheric neutrino MC after all the selection criteria is small (below 20 events). Therefore, to take into account the statistical uncertainty of the number of background, the probability  $P(b)$  is expressed as the convolution of a Poisson and a Gaussian distribution as below;

$$P(b_i) \propto \int_0^\infty \frac{e^{-B} B^{n_{b_i}}}{n_{b_i}!} e^{-(Cb_i - B)^2 / 2\sigma_{b_i}^2} dB, \quad (4.23)$$

where  $n_{b_i}$  is the number of background events in the atmospheric neutrino MC in each momentum region,  $C$  is a constant to normalize the MC live time to the observation time, and the  $\sigma_{b_i}$  is the systematic error of the number of background. In this thesis, only the statistical uncertainties of the signal efficiency and the number of background events are considered. Therefore, Eq.4.18 is expressed as below;

$$P(\Gamma | n_i) = \int_0^\infty \int_0^\infty \frac{e^{-(\Gamma \lambda_i \epsilon_i + b_i)} (\Gamma \lambda_i \epsilon_i + b_i)^{n_i}}{n_i!} e^{-(\epsilon_i - \epsilon_{i0})^2 / 2\sigma_{\epsilon_i}^2} \frac{e^{-Cb_i} (Cb_i)^{n_{b_i}}}{n_{b_i}!} d\epsilon_i db_i \quad (4.24)$$

Then,  $\Gamma_{90\%CL}$  is given by

$$0.9 = \int_{\Gamma=0}^{\Gamma_{90\%CL}} \prod_{i=0,1} P(\Gamma | n_i) d\Gamma. \quad (4.25)$$

Figure 4.23 shows the sensitivity as a function of the operation time of HK. The sensitivity for each operation time is calculated using the values of the signal efficiency and its statistical uncertainty, the background rate by merging the 5 years MC with the full energy region and the 51.9 years MC with the energy region from 0.8 GeV to 100 GeV, and the fiducial volume of HK discussed in Sec.4.3.1.

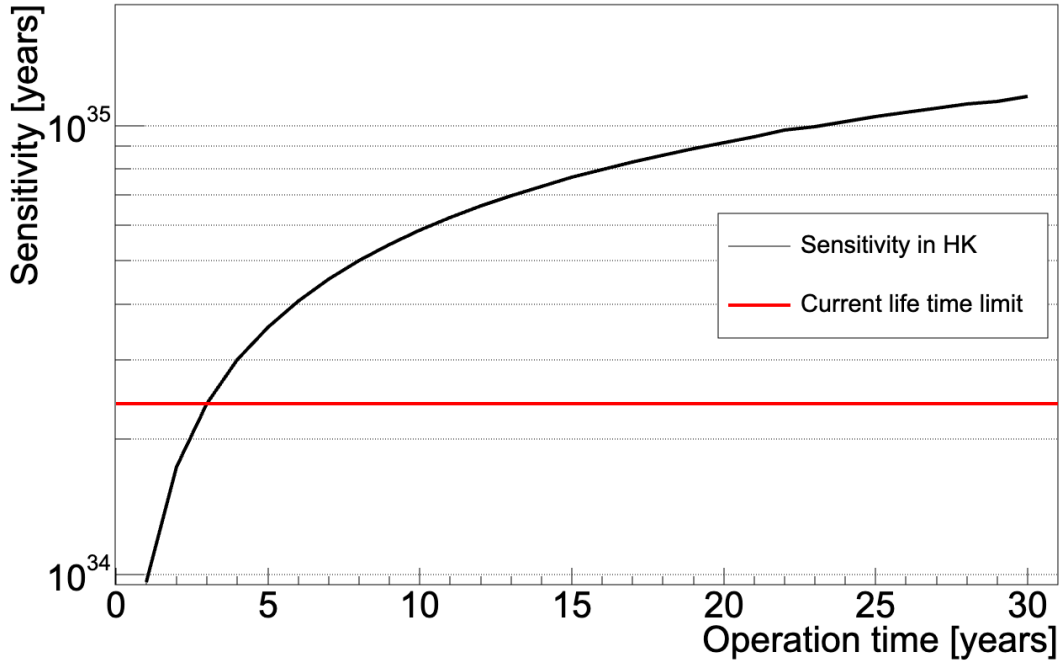


Figure 4.23. Sensitivity in HK as a function of the operation time. Black curve shows the sensitivity in HK and red horizontal line shows the Current life time limit [12].

From this figure, the sensitivity in HK exceeds the current limit after about 3 years operation and reaches  $10^{35}$  years after about 25 years operation without systematic errors. If we consider systematic errors, the sensitivity becomes worse.

The official sensitivity of HK [14] was estimated based on signal efficiency of 38 %, a background rate of 0.68 events/(Mt·year) (using neutron tagging), an fiducial volume of 186 kt, and systematic errors on the same level as SK. Under these conditions, it was estimated that the sensitivity would reach the current lower limit after about 3 years operation and would reach  $10^{35}$  years after about 14 years operation. Therefore, the sensitivity estimated in this study is worse than the official value. However, the sensitivity in this study can be improved as the tuning and development of software for HK is completed, leading to a better signal efficiency, a larger fiducial volume, and a lower background rate with neutron tagging.

## 4.4 Summary

The search sensitivity to the mode of  $p \rightarrow e^+ \pi^0$  is evaluated. This study represents the first attempt using software developed for HK. From the signal and background (atmospheric neutrino) MC study, the signal efficiency and the background rate in HK are estimated to be  $36.76 \pm 0.24$  % and  $1.62 \pm 0.40$  events/(Mt·year) respectively, while the signal efficiency and the background rate were about 42 % and 1.83 events/(Mt·year) respectively in the previous analysis in SK. The search sensitivity in HK with only statistic errors exceeds

the current life time limit after 3 years operation and reaches  $10^{35}$  years after about 25 years operation. These results are worse than the official sensitivity of HK with software for SK, but they can be improved if tuning of software for HK is completed and additional analysis techniques such as neutron tagging are applied.

# Chapter 5

## Summary

HK is a gigantic water Cherenkov detector that is the successor to SK. HK is under construction and the operation will be started in 2027. Proton decay, which is an effective phenomenon to test the theory beyond SM, is one of the main physics target of HK.

In preparation for the search for proton decay in HK, this thesis first evaluates the stability of HKPMT, which are key to the performance of HK, through two types of measurements; “mass-measurement” and “long-term measurement”. In mass-measurement, dark rate and its stability for 1 to 6 months are evaluated and the quality stability throughout the mass production are also monitored. In long-term measurement, dark rate and gain of 16 PMTs have been monitored over a year. For the dark rate, while the results of both measurements basically satisfies the HK’s requirement, further investigation is needed to understand the intrinsic characteristics of PMTs especially for mass-measurement. In addition, more consideration is required when considering a 10- or 20-year operation of HK. For gain, increasing tendency of  $1.3 \pm 0.4$  %/year has been observed. This is a similar trend with SKPMT.

The sensitivity of HK to proton decay ( $p \rightarrow e^+\pi^0$ ) is also evaluated. This thesis represents the first attempt using software developed for HK. Compared to the analysis in SK, the signal efficiency is reduced by a few percent. However, this is thought to be due to the fact that the event reconstruction tool does not account for Cherenkov light scattering in water, and there is room for improvement through future tuning. The amount of background is similar to that of SK without neutron tagging. Assuming the performances estimated in this study, the search sensitivity in HK with only the statistical uncertainty exceeds the current life time limit after 3 years operation and reaches  $10^{35}$  years after about 25 years operation. These results are worse than the official sensitivity of HK with software for SK, but they can be improved if tuning of software for HK is completed and additional analysis techniques such as neutron tagging are applied.

## Acknowledgment

I would like to express my sincere gratitude to my supervisor, Prof. Masashi Yokoyama for providing me with the opportunity to conduct my research. I would also like to express my deep gratitude to Associate Prof. Yasuhiro Nakajima and Prof. Kota Nakagiri for their tremendous support throughout my master course. I want to express my appreciation to the members of the Yokoyama-Nakajima group: Daniel, Xiaodong, Yoshimi, Kodama-san, Okinaga-san, Kobayashi-san, Arai-kun, Mizuno-kun, Muro-kun, Hayasaki-kun, Masaki-kun, and Yufei.

I am grateful to the members of the Hyper-Kamiokande photodetector group for their valuable advice and assistance with the PMT measurements, especially to the following people: Yasuhiro Nishimura, Takuya Tashiro, Akimichi Taketa, and Christophe Bronner. I am also thankful to the members of the Hyper-Kamiokande software group for their patient and detailed explanation of the tools used for proton decay simulations and analysis, especially to the following people: Makoto Miura, Benjamin Quilain, Ryo Matsumoto, and Roger Wendell.

Finally, I would like to express my greatest appreciation to my family for their consideration and support.

# List of Figures

1.1	Elementary particles in the SM. Taken from [3]	5
1.2	Feynman diagrams for $p \rightarrow e^+\pi^0$ via $X$ and $Y$ bosons	6
1.3	A comparison of historical experimental limits on the nucleon lifetime for several key modes and ranges of theoretical prediction as of 2018. Expected limits by some future measurements are also included. Taken from [14].	8
2.1	A schematic view of Cherenkov radiation. Taken from [15].	10
2.2	Cherenkov radiation and PMTs which detect those light. Taken from [16].	11
2.3	A schematic view of HK [17]	12
2.4	The arrangement of PMTs on the ID wall. The circle (left) represents the top (bottom) of a cylindrical tank. The rectangle (right) represents the side of the cylindrical tank. Pink dots in the figure represent PMTs. PMTs are placed in a checkerboard pattern. Taken from [16].	13
2.5	HKPMT	14
2.6	Venetian blind type dynode in SKPMT (left) and Box & Line type dynode in HKPMT (Right) [19]	14
2.7	Transit time distribution at single photoelectron [14]. Blue solid line is HKPMT and black dotted line is SKPMT.	15
2.8	Single photoelectron distribution with pedestal [14]. Blue solid line is HKPMT and black dotted line is SKPMT.	15
2.9	Relative single photon detection efficiency as a function of the position in the photocathode, where a position angle is zero at the PMT center and $\pm 90^\circ$ at the edges [14]. The dashed line is the result of a scan along the line of symmetry of the Box&Line dynode structure, and the solid line is the result of a scan along the direction orthogonal to the line of symmetry.	16
2.10	Side view of HKPMT [14]	17
3.1	Time variation of the averaged PMT gain measured by using the PMTs in the bottom of the SK tank [15]. The colors show the detector periods; black, red, green and blue are for SK-I, -II, -III and -IV, respectively.	20
3.2	A view of the darkroom where PMTs are installed (left) and PMTs arrangement (right). There is another darkroom next to this room.	21
3.3	Time variation of temperature inside the dark room. The points where temperature changes like a spike correspond to when the darkroom was opened for PMT replacement. There are no data between November 2023 and March 2024 due to the problem of the thermometer.	21

3.4	Map indicating which PMTs in each room are connected to which QBEE and HV modules. Top (Bottom) left is for QBEEs in room A (B) and top (bottom) right is for HV modules in room A (B). . . . .	22
3.5	Trends of temperatures of 10 QBEEs between February 2024 and October 2024. . . . .	23
3.6	Examples of time variation of dark rate. The left is stable PMT. The right is unstable PMT and fails the criterion 2 and 3. . . . .	24
3.7	The position where problematic PMTs were detected in room B between July 2023 and July 2024. . . . .	26
3.8	The distribution of QBEE and HV modules where problematic PMTs connected in room B between July 2023 and July 2024. Left is for QBEE and right is for HV module. . . . .	27
3.9	The position where problematic PMTs were detected in room B after replacement of module 5 and 7 of HV in August 2024. . . . .	28
3.10	The distribution of QBEE and HV modules where problematic PMTs connected in room B after replacement of module 5 and 7 of HV on August 2024. Left is for QBEE and right is for HV module. . . . .	28
3.11	The overview of the setup of long-term measurement. The left is the PMTs and darkroom layout. The middle top is the larger dark room where 10 PMTs are set and the middle bottom is the smaller dark room where 6 PMTs are set. The right is one of the optical fibers fixed on each PMT for photon injection. . . . .	30
3.12	Time variation of temperature in the dark room. The points where temperature changes like a spike correspond to when the darkroom was opened for minor setup changes. . . . .	30
3.13	DAQ system. The left is the flowchart of how signals are processed. The right is the electric rack. . . . .	32
3.14	Time variation of dark rate. The top is dark rates of 10 PMTs in the larger dark room and the bottom is that of 6 PMTs in the smaller dark room. . .	33
3.15	Time variation of radon concentration at the entrance of the laboratory. . .	34
3.16	Scatter plot of the average dark rate of 16 PMTs against the radon concentration. . . . .	35
3.17	The baseline of the ADCs (left) and the signal (right) as a function of time. Periodic structures emerge due to noise. . . . .	36
3.18	An example of a charge distribution distorted by noise. The pink, green, and light blue dotted lines show the first, second, and third term of Eq. (3.1), respectively. The red dotted curve shows the summation of the second and third term of Eq. (3.1). . . . .	36
3.19	Smearing of charge distribution by Gaussian convolution. $\sigma$ of the Gaussian is 0.25 pC. It can be seen that before smearing, the fitting described below failed due to distortion of the charge distribution caused by noise, and that smearing enables proper fitting. The pink, green, and light blue dotted lines in both distributions show the first, second, and third term of Eq. (3.1), respectively. The red dotted curve shows the summation of the second and third term of Eq. (3.1). . . . .	37

3.20	How to obtain gain from charge distribution. The pink, green, and light blue dotted lines show the first, second, and third term of Eq. (3.1), respectively. The red dotted curve shows the summation of the second and third term of Eq. (3.1). . . . .	38
3.21	How to obtain correction factors between new ADC and previous ADC. . .	39
3.22	Time variation of gain. The left top shows the gain of 8 PMTs in the larger dark room and the left bottom shows the gain of 6 PMTs in the smaller dark room. The right is the distribution of change rate of gain per year when the gain of each PMT at the beginning of the measurement is set to 1. In CH6, data from November 11 <sup>th</sup> to November 28 <sup>th</sup> (red circle) were rejected when calculating the variation of the gain due to a clear abnormal gain caused by a cable connection problem. . . . .	40
4.1	Distributions of simulated initial momentum (left) and effective invariant mass (right) of protons. The cyan, black, green, red and purple histograms correspond to free, bound, $s$ -state, $p$ -state and correlated decay protons, respectively. Taken from [15]. . . . .	43
4.2	Direction-averaged atmospheric neutrino flux at SK by the Honda flux (red) and other models (blue, black, and green). The absolute flux is on the left and the the flux ratio is on the right. Taken from [30]. . . . .	44
4.3	Distributions of CC $\nu_\mu$ (left) and $\bar{\nu}_\mu$ (right) cross sections per nucleon as a function of neutrino energy simulated in NEUT (solid lines) and the experimental data (dots). Taken from [34], . . . . .	45
4.4	Event display of a $p \rightarrow e^+\pi^0$ event. . . . .	47
4.5	Schematic diagram illustrating the relationship between the variables for the predicted charge, with the particle's vertex position marked as a white dot. Taken from [41]. . . . .	49
4.6	Distribution of goodness as a function of $t$ for an event with a parent muon and a Michel electron. The vertical dashed lines indicate true particle time. The black dots are the scanned goodness points. The blue and green lines indicate the threshold which are used to search peaks. The red vertical lines indicate the time of the subevents found by the algorithm. Taken from [41]. . . . .	50
4.7	Tree diagram illustrating the ring counting algorithm. In this figure, the process starts from single electron ring hypothesis. Taken from [41]. . . . .	51
4.8	Definition of the momentum resolution. The blue histograms shows a distribution of reconstructed momentum. The red line shows a Gaussian fitted to the histogram. The momentum resolution is defined as the ratio of the sigma of the Gaussian to the true momentum. . . . .	53
4.9	Momentum resolution plotted as a function of the distance from the true vertex points to the nearest wall for electrons (left) and muons (right). . .	53
4.10	The distributions of $\ln(L_e/L_{\pi^+})$ for electrons and muons in the region where the distance from the nearest wall is greater than 200 cm. . . . .	54
4.11	PID accuracy plotted as a function of the distance from the true vertex position to the nearest wall for electrons (left) and muons (right). . . . .	54

4.12	The distribution of the number of rings in the signal (right) and atmospheric neutrino (left) MC after applying the criterion 1. In the right plot, the black histogram is for all protons and the blue one is for free protons. The black vertical lines and arrow symbols show the selected region for the criterion 2. . . . .	56
4.13	The distribution of all $e$ -like or not in the signal (right) and atmospheric neutrino (left) MC after applying the criterion 1 and 2. In each histogram, 1 of the horizontal axis means all $e$ -like (accepted) and 0 means the other (rejected). In the right plot, the black is for all protons and the blue is for free protons. The black vertical lines and arrow symbols show the selected region for the criterion 3. . . . .	57
4.14	The distribution of the number of Michel electrons in the signal (right) and atmospheric neutrino (left) MC after applying the criterion 1-3. In the right plot, the black histogram is for all protons and the blue one is for free protons. The black vertical lines and arrow symbols show the selected region for the criterion 4. . . . .	57
4.15	The distribution of $M_{\pi_0}$ in the signal (right) and atmospheric neutrino (left) MC after applying the criterion 1-4. In the right plot, the black histogram shows the all protons and the blue one shows the free protons. The black vertical lines and arrow symbols show the selected region for the criterion 5. . . . .	58
4.16	The distribution of reconstructed proton mass in the signal (right) and atmospheric neutrino MC (left) events after applying the criterion 1-5. In the right plot, the black histogram shows the all protons and the blue one shows the free protons. The black vertical lines and arrow symbols show the selected region for the criterion 6. . . . .	59
4.17	The distribution of total momentum in the signal (right) and atmospheric neutrino(left) MC after applying the criterion 1-5. In the right plot, the black histogram shows the all protons and the blue one shows the free protons. The black vertical lines and arrow symbols show the selected region for the criterion 7. . . . .	59
4.18	Signal efficiency (right) and remaining 5 years atmospheric neutrino MC (left) after applying each criterion. C1 to C7 in the horizontal axis correspond to the criterion 1 to 7, respectively. . . . .	60
4.19	The breakdown of the signal efficiency and remaining backgrounds in the latest analysis in SK. C1-7 correspond to the criterion 1 to 7. C8 is ignored because it is the criterion for number of tagged neutrons and not applied in this analysis. Taken from [12]. . . . .	61
4.20	Primary neutrino energy distributions of the remaining 5 years atmospheric neutrino MC after applying the criterion 6 (total mass cut). . . . .	63
4.21	Primary neutrino energy distributions of the remaining atmospheric neutrino MC after applying all the criteria in SK. Taken from [12]. . . . .	63

4.22	Total mass ( $M_{tot}$ ) and momentum ( $P_{tot}$ ) scatter plots for the 5+51.9 years atmospheric neutrino MC (left) and for the signal MC (right) after applying the criteria 1 to 5. For the right figure, the light (dark) blue shows free (bound) proton decay events. The two boxes in both figures correspond to the $P_{tot} < 100\text{MeV}/c$ (lower momentum) region and the $100 < P_{tot} < 250\text{MeV}/c$ (higher momentum) region. . . . .	64
4.23	Sensitivity in HK as a function of the operation time. Black curve shows the sensitivity in HK and red horizontal line shows the Current life time limit [12]. . . . .	67

# List of Tables

2.1	Momentum thresholds of the Cherenkov radiation in water for various charged particles in water ( $n = 1.34$ ) . . . . .	9
2.2	Summary of the basic performances of HKPMT and SKPMT . . . . .	16
3.1	Breakdown of the summary of each measurement period of 1-month measurements . . . . .	25
3.2	Breakdown of the summary of each measurement period of 3- or 6-month measurements . . . . .	25
3.3	List of equipment used for measurements . . . . .	32
3.4	List of correction factors . . . . .	39
4.1	Breakdown of the fraction of the types of $\pi$ -FSI . . . . .	43
4.2	Signal efficiency and remaining 5 years atmospheric neutrino MC after applying each criterion. . . . .	60
4.3	Signal efficiency after applying all criteria and background rate . . . . .	61
4.4	Signal efficiencies and background rates in the lower and higher momentum regions . . . . .	64

# Bibliography

- [1] G. Aad et al. Observation of a new particle in the search for the standard model higgs boson with the atlas detector at the lhc. *Physics Letters B*, 716(1):1–29, 2012. URL: <https://www.sciencedirect.com/science/article/pii/S037026931200857X>, doi:10.1016/j.physletb.2012.08.020. (page 4).
- [2] S. Chatrchyan et al. Observation of a new boson at a mass of 125 gev with the cms experiment at the lhc. *Physics Letters B*, 716(1):30–61, 2012. URL: <https://www.sciencedirect.com/science/article/pii/S0370269312008581>, doi:10.1016/j.physletb.2012.08.021. (page 4).
- [3] Higgstan. Referenced on December 26, 2024. URL: <https://higgstan.com/standerd-model/>. (pages 5, 71).
- [4] H. Georgi and S.L. Glashow. Unity of all elementary-particle forces. *Phys. Rev. Lett.*, 32:438–441, Feb 1974. URL: <https://link.aps.org/doi/10.1103/PhysRevLett.32.438>, doi:10.1103/PhysRevLett.32.438. (page 5).
- [5] Paul Langacker. Grand unification and the standard model, 1994. URL: <https://arxiv.org/abs/hep-ph/9411247>, doi:10.48550/arXiv.hep-ph/9411247. (page 6).
- [6] H. Murayama and A. Pierce. Not even decoupling can save the minimal supersymmetric su(5) model. *Phys. Rev. D*, 65:055009, Feb 2002. URL: <https://link.aps.org/doi/10.1103/PhysRevD.65.055009>, doi:10.1103/PhysRevD.65.055009. (page 6).
- [7] H. Kolečová and M. Malinský. Proton lifetime in the minimal so(10) gut and its implications for the lhc. *Phys. Rev. D*, 90:115001, Dec 2014. URL: <https://link.aps.org/doi/10.1103/PhysRevD.90.115001>, doi:10.1103/PhysRevD.90.115001. (page 7).
- [8] H. Kolečová and M. Malinský. Flavor structure of guts and uncertainties in proton lifetime estimates. *Phys. Rev. D*, 99:035005, Feb 2019. URL: <https://link.aps.org/doi/10.1103/PhysRevD.99.035005>, doi:10.1103/PhysRevD.99.035005. (page 7).
- [9] C. McGrew et al. Search for nucleon decay using the imb-3 detector. *Phys. Rev. D*, 59:052004, Feb 1999. URL: <https://link.aps.org/doi/10.1103/PhysRevD.59.052004>, doi:10.1103/PhysRevD.59.052004. (page 7).

- [10] K.S. Hirata et al. Experimental limits on nucleon lifetime for lepton+meson decay modes. *Physics Letters B*, 220(1):308–316, 1989. URL: <https://www.sciencedirect.com/science/article/pii/0370269389900580>, doi:10.1016/0370-2693(89)90058-0. (page 7).
- [11] M. Miura. Search for nucleon decay in super-kamiokande. *Nuclear and Particle Physics Proceedings*, 273-275:516–521, 2016. 37th International Conference on High Energy Physics (ICHEP). URL: <https://www.sciencedirect.com/science/article/pii/S2405601415005659>, doi:10.1016/j.nuclphysbps.2015.09.076. (page 7).
- [12] A. Takenaka et al. Search for proton decay via  $p \rightarrow e^+\pi^0$  and  $p \rightarrow \mu^+\pi^0$  with an enlarged fiducial volume in super-kamiokande i-iv. *Phys. Rev. D*, 102:112011, Dec 2020. URL: <https://link.aps.org/doi/10.1103/PhysRevD.102.112011>, doi:10.1103/PhysRevD.102.112011. (pages 7, 46, 55, 60, 61, 62, 63, 64, 67, 74, 75).
- [13] K. Abe et al. Search for proton decay via  $p \rightarrow \nu K^+$  using 260 kiloton · year data of super-kamiokande. *Phys. Rev. D*, 90:072005, Oct 2014. URL: <https://link.aps.org/doi/10.1103/PhysRevD.90.072005>, doi:10.1103/PhysRevD.90.072005. (page 7).
- [14] K. Abe et al. Hyper-kamiokande design report, 2018. URL: <https://arxiv.org/abs/1805.04163>, doi:10.48550/arXiv.1805.04163. (pages 8, 15, 16, 17, 42, 67, 71).
- [15] Y. Suda. *Search for Proton Decay Using an Improved Event Reconstruction Algorithm in Super-Kamiokande*. PhD thesis, University of Tokyo, 2017. (pages 10, 19, 20, 43, 55, 71, 73).
- [16] S. Yoshida. Performance evaluation of initial mass produced 50 cm diameter photomultiplier tubes for hyper-kamiokande. Master’s thesis, University of Tokyo, 2022. (pages 11, 13, 71).
- [17] Hyper kamiokande home page. Referenced on December 26, 2024. URL: <https://www-sk.icrr.u-tokyo.ac.jp/hk/about/outline/>. (pages 12, 71).
- [18] A. Suzuki et al. Improvement of 20 in. diameter photomultiplier tubes. *Nuclear Instruments and Methods in Physics Research Section A: Accelerators, Spectrometers, Detectors and Associated Equipment*, 329(1):299–313, 1993. URL: <https://www.sciencedirect.com/science/article/pii/016890029390949I>, doi:10.1016/0168-9002(93)90949-I. (page 13).
- [19] D. Fukuda et al. Properties of New 50 cm Photodetectors in an Environment for Hyper-Kamiokande. In *International Conference on New Photo-detectors PhotoDet2015*, 2016. (pages 14, 71).
- [20] J. Xia et al. The calibration and evaluation of 50 cm box and line photomultiplier tubes designed for hyper-kamiokande. In *Proceedings of the 5th International Workshop on New Photon-Detectors (PD18)*, 2019. URL: <https://journals.jps>.

- [jp/doi/abs/10.7566/JPSCP.27.012002](https://doi.org/10.7566/JPSCP.27.012002), [arXiv:https://journals.jps.jp/doi/pdf/10.7566/JPSCP.27.012002](https://arxiv.org/abs/https://journals.jps.jp/doi/pdf/10.7566/JPSCP.27.012002), [doi:10.7566/JPSCP.27.012002](https://doi.org/10.7566/JPSCP.27.012002). (page 16).
- [21] H. Nishino et al. High-speed charge-to-time converter ASIC for the super-kamiokande detector. *Nuclear Instruments and Methods in Physics Research Section A: Accelerators, Spectrometers, Detectors and Associated Equipment*, 610(3):710–717, 2009. URL: <https://www.sciencedirect.com/science/article/pii/S0168900209017495>, [doi:10.1016/j.nima.2009.09.026](https://doi.org/10.1016/j.nima.2009.09.026). (pages 22, 23).
- [22] H. Nishino. スーパーカミオカンデにおける新データ収集エレクトロニクスの研究と開発. Master's thesis, University of Tokyo, 2006. (page 23).
- [23] T. Tomiya. Investigation of the impact of magnetic field on 50 cm diameter photomultiplier tubes for hyper-kamiokande. Master's thesis, University of Tokyo, 2023. URL: [https://www-sk.icrr.u-tokyo.ac.jp/hk/doc/thesis/tomiya\\_mthesis.pdf](https://www-sk.icrr.u-tokyo.ac.jp/hk/doc/thesis/tomiya_mthesis.pdf). (page 23).
- [24] M.G. Mayer and J.H.D. Jensen. *Elementary Theory of Nuclear Shell Structure*. Wiley, New York, 1955. (page 43).
- [25] K. Nakamura et al. The reaction  $^{12}\text{C}(e, ep)$  at 700 MeV and DWIA analysis. *Nuclear Physics A*, 268(3):381–407, 1976. URL: <https://www.sciencedirect.com/science/article/pii/037594747690539X>, [doi:10.1016/0375-9474\(76\)90539-X](https://doi.org/10.1016/0375-9474(76)90539-X). (page 43).
- [26] T. Yamazaki and Y. Akaishi. Nuclear medium effects on invariant mass spectra of hadrons decaying in nuclei. *Physics Letters B*, 453(1):1–6, 1999. URL: <https://www.sciencedirect.com/science/article/pii/S037026939900163X>, [doi:10.1016/S0370-2693\(99\)00163-X](https://doi.org/10.1016/S0370-2693(99)00163-X). (page 43).
- [27] Y. Hayato and L. Pickering. The NEUT neutrino interaction simulation program library. *The European Physical Journal Special Topics*, 230(24):4469–4481, 2021. [doi:10.1140/epjs/s11734-021-00287-7](https://doi.org/10.1140/epjs/s11734-021-00287-7). (pages 43, 44).
- [28] L.L. Salcedo et al. Computer simulation of inclusive pion nuclear reactions. *Nuclear Physics A*, 484(3):557–592, 1988. URL: <https://www.sciencedirect.com/science/article/pii/0375947488903107>, [doi:10.1016/0375-9474\(88\)90310-7](https://doi.org/10.1016/0375-9474(88)90310-7). (page 43).
- [29] R.D. Woods and D.S. Saxon. Diffuse surface optical model for nucleon-nuclei scattering. *Phys. Rev.*, 95:577–578, Jul 1954. URL: <https://link.aps.org/doi/10.1103/PhysRev.95.577>, [doi:10.1103/PhysRev.95.577](https://doi.org/10.1103/PhysRev.95.577). (page 43).
- [30] M. Honda et al. Calculation of atmospheric neutrino flux using the interaction model calibrated with atmospheric muon data. *Phys. Rev. D*, 75:043006, Feb 2007. URL: <https://link.aps.org/doi/10.1103/PhysRevD.75.043006>, [doi:10.1103/PhysRevD.75.043006](https://doi.org/10.1103/PhysRevD.75.043006). (pages 44, 73).

- [31] M. Honda et al. Improvement of low energy atmospheric neutrino flux calculation using the jam nuclear interaction model. *Phys. Rev. D*, 83:123001, Jun 2011. URL: <https://link.aps.org/doi/10.1103/PhysRevD.83.123001>, doi:10.1103/PhysRevD.83.123001. (page 44).
- [32] G. Battistoni et al. The fluka atmospheric neutrino flux calculation. *Astroparticle Physics*, 19(2):269–290, 2003. URL: <https://www.sciencedirect.com/science/article/pii/S0927650502002463>, doi:10.1016/S0927-6505(02)00246-3. (page 44).
- [33] G. D. Bar et al. Three-dimensional calculation of atmospheric neutrinos. *Phys. Rev. D*, 70:023006, Jul 2004. URL: <https://link.aps.org/doi/10.1103/PhysRevD.70.023006>, doi:10.1103/PhysRevD.70.023006. (page 44).
- [34] T. J. Irvine. *Development of Neutron-Tagging Techniques and Application to Atmospheric Neutrino Oscillation Analysis in Super-Kamiokande*. PhD thesis, University of Tokyo, 2014. (pages 44, 45, 73).
- [35] Wcsim github. Referenced on January 4, 2025. URL: <https://github.com/WCSim>. (page 46).
- [36] J. Allison et al. Recent developments in geant4. *Nuclear Instruments and Methods in Physics Research Section A: Accelerators, Spectrometers, Detectors and Associated Equipment*, 835:186–225, 2016. URL: <https://www.sciencedirect.com/science/article/pii/S0168900216306957>, doi:10.1016/j.nima.2016.06.125. (page 46).
- [37] H. Ikeda et al. Front-end hybrid circuit for super-kamiokande. *Nuclear Instruments and Methods in Physics Research Section A: Accelerators, Spectrometers, Detectors and Associated Equipment*, 320(1):310–316, 1992. URL: <https://www.sciencedirect.com/science/article/pii/0168900292907912>, doi:10.1016/0168-9002(92)90791-2. (page 46).
- [38] R. B. Patterson et al. The extended-track event reconstruction for miniboone. *Nuclear Instruments and Methods in Physics Research Section A: Accelerators, Spectrometers, Detectors and Associated Equipment*, 608(1):206–224, 2009. URL: <https://www.sciencedirect.com/science/article/pii/S0168900209012480>, doi:10.1016/j.nima.2009.06.064. (page 47).
- [39] M. Shiozawa. Reconstruction algorithms in the super-kamiokande large water cherenkov detector. *Nuclear Instruments and Methods in Physics Research Section A: Accelerators, Spectrometers, Detectors and Associated Equipment*, 433(1):240–246, 1999. URL: <https://www.sciencedirect.com/science/article/pii/S0168900299003599>, doi:10.1016/S0168-9002(99)00359-9. (page 47).
- [40] R. Matsumoto et al. Search for proton decay via  $p \rightarrow \mu^+ K^0$  in 0.37 megaton-years exposure of super-kamiokande. *Phys. Rev. D*, 106:072003, Oct 2022. URL: <https://link.aps.org/doi/10.1103/PhysRevD.106.072003>, doi:10.1103/PhysRevD.106.072003. (page 47).

- [41] S. Tobayama. *An Analysis of the Oscillation of Atmospheric Neutrinos*. PhD thesis, University of British Columbia, 2016. (pages [47](#), [49](#), [50](#), [51](#), [73](#)).